Characterization of the Multipath Environment of Ionospheric Scintillation Receivers

Tsige Yared Atilaw

ATLTSI001

Dissertation presented in partial fulfillment of the requirements for the degree of Master of Philosophy Specialising in Space Studies

Supervisors: Prof. Pierre Cilliers and Prof. Peter Martinez

MPhil in Space Studies
Department of Electrical Engineering
University of Cape Town
Cape Town, South Africa, October 2015

SL15-01

Declaration

I hereby declare that this dissertation is my own work and it has not been submitted anywhere for any award. Where other sources of information have been used, they have been acknowledged.

Signed by candidate

Tsige Yared Atilaw
MPhil in Space Studies,
Department of Electrical Engineering,
University of Cape Town,
South Africa

Abstract

Global Navigation Satellite Systems (GNSS) are used to provide information on position, time and velocity all over the world at any time of the day. Currently there are four operational GNSS and one of them is GPS (Global Positioning System) that is developed and maintained by U.S Department of Defence (DoD), which is widely used and accessible all over the world. The accuracy of the output or even the availability of the navigation system depends on current space weather conditions, which can cause random fluctuations of the phase and amplitude of the received signal, called scintillation. Interference of GNSS signals that are reflected and refracted from stationary objects on the ground, with signals that travel along a direct path via the ionosphere to the antenna, cause errors in the measured amplitude and phase. These errors are known as multipath errors and can lead to cycle slip and loss of lock on the satellite or degradation in the accuracy of position determination. High elevation cutoff angles used for filtering GNSS signals, usually $15 - 30°$, can reduce non-ionospheric interference due to multipath signals coming from the horizon. Since a fixed-elevation threshold does not take into consideration the surrounding physical environment of each GPS station, it can result in a significant loss of valuable data. Alternatively, if the fixed-elevation threshold is not high enough we run the risk of including multipath data in the analysis.

In this project we characterized the multipath environment of the GPS Ionospheric Scintillation and TEC (Total Electron Content) Monitor (GISTM) receivers installed by SANSA (South African National Space Agency) at Gough Island (40.34^o S and 9.88^o W), Marion Island (46.87^o S and 37.86^o E), Hermanus (34.42^o S and 19.22^o E) and SANAE IV (71.73^o S and 2.2^o W) by plotting azimuth-elevation maps of scintillation indices averaged over one year. The azimuth-elevation maps were used to identify objects that regularly scatter signals and cause high scintillation resulting from multipath effects. After identifying the multipath area from the azimuth-

elevation map, an azimuth-dependent elevation threshold was developed using the MATLAB curve fitting tool. Using this method we are able to reduce the multi-path errors without losing important data. Using the azimuth-dependent elevation threshold typically gives 5 to 28% more useful data than using a 20° fixed-elevation threshold.

Acknowledgement

I would like to express my sincere appreciation and thanks to my supervisors, Professor Pierre Cilliers and Professor Peter Martinez, for their extraordinary and continuous support, mentorship and encouragement through my study.

I wish to express my sincere thanks to the South African National Space Agency (SANSA) Space Science Directorate for providing me with all the necessary facilities for the research printed in this thesis; for creating a positive environment during my study and for the financial support for attending international and national conferences during my studies. I am also grateful for all of the financial support provided by the National Astrophysics and Space Science Programme (NASSP). I take this opportunity to express my gratitude to all of my colleagues who supported me and were there to help me from the very first day at SANSA until I was writing my dissertation. I would like to thank Mr. Jacques du Plessis for proofreading my work and for giving me a lot of helpful feedback.

Special thanks to my lovely family who are always in my thoughts, Titiye, Abaye, Babaye, Enanye, Mesay, Ashenafi, Bigu, Alex, Amex and so on. Thank you for all of your support, encouragement and attention. It is your prayer for me that has given me strength throughout these years.

Above all I would like to thank the one and only almighty God for every single thing He has done for me.

Contents

Abbreviations and acronyms

ADET Azimuth Dependent Elevation Threshold
C/A Code/Acquisition
CCDIV Code-Carrier Divergence
CCSTDDEV Standard deviation of Code-Carrier Divergence
CNo Carrier-to-Noise density
DoD Department of Defence
EUV Extreme Ultraviolet
GBSC Ground Based Scintillation Climatology
GEO Geostationary
GISTM GPS Ionospheric Scintillation and Total Electron Content Monitoring
GIS Geographic Information System
GLONASS Global Orbiting Navigation Satellite System
GNSS Global Navigation Satellite Systems
GPS Global Positioning System
LEO Low Earth Orbit
PPS Precise Position Service
PRN Pseudo-Random Number
RTEC Rate of TEC
S/No Signal-to-noise density
SAMA South Atlantic Magnetic Anomaly
SANAE South African National Antarctic Expedition
SANSA South African National Space Agency
SAPS Subauroral Polarization Streams
SBAS Satellite Based Augmentation System
SCINDA Scintillation Network and Decision Aid
SED Storm Enhanced Density
SNR Signal-to-Noise Ratio

SPS Standard Position System
TEC Total Electron Content
TOW Time Of Week
UT Universal Time
UV Ultraviolet

Chapter 1

Introduction

Radio signals that are transmitted from satellites can be distorted by variations in the propagation medium through which they travel from the transmitting point to the receiving point. Global Navigation Satellite Systems (GNSS) signals travel from a satellite to a receiver over a distance in the range between 19,000 km and 23,000 km. Trans-ionospheric signals undergo refraction (change in speed and direction) because of the change in the refractive index of the propagation medium. The refractive index of the propagation medium determines the speed of the propagating signal. Since the composition of the ionosphere and troposphere is not uniform, the refractive index changes all along the path of the signal resulting in "bending" of the signal which makes the path longer compared to the geometrical straight line path (Misra and Enge, 2006). Bending of signals and consequent delay effects are more pronounced for signals received from satellites at lower elevation because these signals travel a longer path through the atmosphere compared to signals that are coming from satellites at higher elevation angles (El-Rabbany, 2002).

Random fluctuations in the amplitude and phase of the received GNSS signal are known as *scintillation* (Davies, 1990; Ondoh and Marubashi, 2001). Space weather conditions and solar irradiation determine the severity of ionospheric scintillation. Scintillation intensity is directly related to random electron density fluctuations, which are also known as ionospheric irregularities (Kintner *et al.*, 2007; Wernik *et al.*, 2003). Ionospheric irregularities act as wave scatterers for GNSS signals which pass through the ionosphere (see Figure 1.1). As Figure 1.1 illustrates, physical structures, both near and far, can act as signal reflectors that can produce multipath signals (Hofmann-Wellenhof *et al.*, 1992; Mohinder *et al.*, 2001). Multipath effects

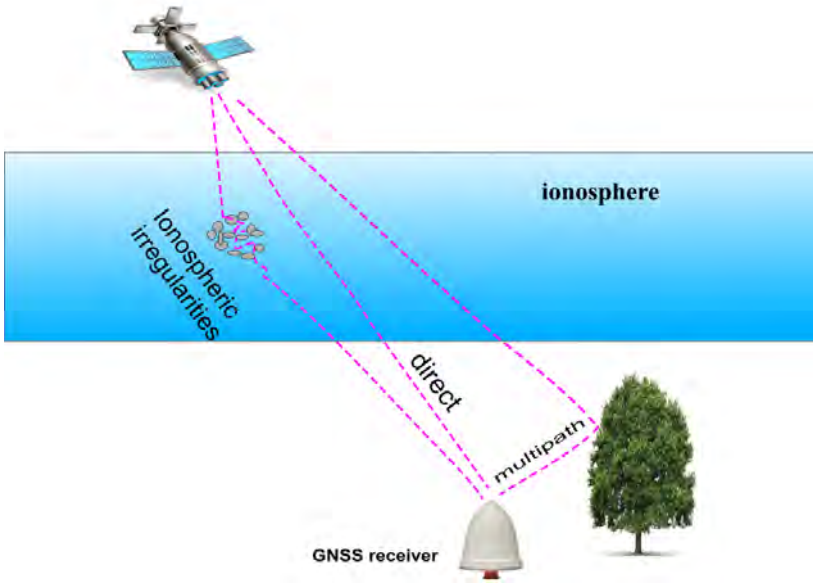

Figure 1.1: Pictorial illustration of the multipath effect of ionospheric irregularities and physical structures found in the vicinity of a GNSS receiver antenna.

of both ionospheric irregularities and reflecting physical structures that are found in the environment surrounding an antenna contribute to the degradation of GNSS performance. Deep and long scintillations or signal fading may extend the time for the GNSS receiver to recover from cycle slips or loss of lock (Kintner *et al.*, 2007). Sufficiently intense scintillation can result in the failure of GNSS receivers to track signals from some GNSS satellites. This will lead to increased navigation errors, which can cause navigation failure (Kaplan and Hegarty, 2006; Kintner *et al.*, 2007). So far, the most efficient way to compensate for the ionospheric delay is to characterize the delay by using dual-frequency measurements (Hofmann-Wellenhof *et al.*, 1992).

Although nothing can be done to control errors due ionospheric irregularities, it is possible to limit multipath errors due to reflecting physical structures in the vicinity of GNSS receiver antennas. It is therefore advisable to study the environment to identify any nearby stationary reflecting structures before the installation of a GNSS receiver antenna, and to then install the antenna at a sufficient height to minimize interference due to multipath signals from such structures. This project aims to characterize the multipath environment of ionospheric scintillation receivers in order to identify areas in azimuth-elevation space that might be linked to stationary physical structures, in the vicinity of the antenna, that give rise to multipath errors. An elevation mask that can be used to filter out these multipath errors will be developed, which will improve the quality of the scintillation data for ionospheric studies.

1.1 Motivation

Scintillation studies are useful in the study of the formation and evolution of ionospheric irregularities (Alfonsi *et al.*, 2011; Romano *et al.*, 2013). The surrounding environment of GNSS antennas has a great impact on the quality of the data that can be used for scintillation studies. Ionospheric scintillation studies and mitigation techniques need to be based on well-established data quality (Romano *et al.*, 2013). Therefore, characterizing the antenna environment should be the first step to improving the quality of GNSS data.

During the post-processing of GNSS data a fixed-elevation cutoff angle, in the range $15° - 30°$, is usually used to reduce multipath effects from stationary structures in the environment of the antenna. This simplistic approach does not take into consideration the surrounding environment of a specific receiver antenna. Applying a fixed elevation cutoff angle leads to the loss of valuable data associated with non-multipath signals and may not remove all of the multipath errors due to structures that have elevation angles above the fixed cut-off angle.

Multipath effects are location dependent, which means that each receiver environment has to be characterized individually in order to reduce errors that are caused by multipath effects without losing valuable data. Characterizing the multipath environment of a GNSS antenna can help to identify in azimuth-elevation space areas affected by stationary multipath sources. A location-specific elevation mask can be developed from the characteristics of the environment. Such a mask can filter out signals that are distorted by multipath effects and thus reduce the multipath errors.

1.2 Objectives and benefits of this project

The main objective of this project is to reduce the multipath errors that are due to the physical surrounding environment of GNSS antennas.

The objectives of the project include:

- identifying structures that are the cause of multipath errors by means of azimuth-elevation maps for each station;
- developing a station-specific azimuth-dependent elevation mask to filter out multipath errors;
- improving the quality and quantity of useful GNSS data in ionospheric studies and scintillation climatology studies.

In this project, we have analysed scintillation data from GPS Ionospheric Scintillation and TEC (Total Electron Content) Monitor (GISTM) receivers installed at Gough Island, Hermanus, Marion Island and SANAE IV to identify stationary multipath sources. In the analysis we used data series of up to 1 year in duration from each receiver. The analysis is used to associate the occurrence of persistent scintillations throughout the selected period with scintillations that are caused by the multipath effects of stationary physical structures found in the vicinity of the receiver antenna. We have adapted the Ground Based Scintillation Climatology (GBSC) method (Alfonsi *et al.*, 2011; Romano *et al.*, 2013; Spogli *et al.*, 2009, 2010, 2014), which uses azimuth-elevation maps for scintillation climatology analysis and multipath characterization.

Azimuth-elevation maps of the percentage occurrence of scintillation indices above a given threshold, for all satellites in view of a given station at each epoch, were used to identify areas, in azimuth-elevation space, with high and regular scintillation due to multipath effects. The identification of stationary structures that are sources of multipath signals allowed us to develop an azimuth-dependent elevation threshold mask. This mask will improve the quality of the data by effectively filtering out non-ionospheric scintillation for the post-processing of scintillation data in climatology studies. The fact that this mask is specific to the surrounding environment of a particular antenna will reduce the data loss that is incurred by using an arbitrary fixed elevation threshold.

1.3 Thesis outline

This thesis contains 5 chapters: the introduction, theoretical background, methods, result, discussion and conclusion. This chapter is a brief introduction to the objective and motivation for this study. Chapter 2 covers the basic theoretical background on the ionosphere, scintillation and scintillation errors on GNSS. Chapter 3 covers the instrumentation and the main techniques used in the data analysis. In Chapter 4 the results are discussed. Chapter 5 contains conclusions and recommendations for future research.

Chapter 2

Theoretical Background

The objective of this project is to reduce the multipath effects that are due to the physical environment surrounding GNSS antennas. Multipath effects cause interference with direct signals, which can distort signals and introduce errors in GNSS applications, such as position estimation. Radio wave signals that are transmitted from GNSS navigation satellites are affected by the propagation medium they travel through, which, in this case, is the Earth's atmosphere. Earth's atmosphere is composed of different layers that have different compositions, ionization level, density and temperature. The upper atmosphere includes a conducting layer with high electron density called the ionosphere. Random changes in the electron density act as a signal scatterer and cause multipath effects which manifest as ionospheric scintillation. Ionospheric scintillation is measurable as random fluctuation of the amplitude and phase of the received signal. Scintillation can also be introduced by the multipath effect of the physical environment of the antenna. This chapter addresses the basic theoretical background for the main elements of this thesis. We begin with a brief description on the Earth's atmosphere and the ionosphere in sections 2.1 and 2.2. Sections 2.3 and 2.4 deal with terrestrial and trans-ionospheric radio wave propagation. Sections 2.5 to 2.7 deal with scintillation effects and parameters used to measure scintillation. Sections 2.8 and 2.9 describe GNSS and the sources of errors in GNSS applications, with a specific reference to GPS.

2.1 Earth's atmosphere

Earth's atmosphere is a gas composed mainly of molecular nitrogen, molecular oxygen and atomic argon that surrounds the Earth with a number density percentage of 78.08%, 20.95% and 0.93% at sea level, respectively (Davies, 1990). Earth's atmosphere has different layers with varying temperature, pressure and density. The density is high at low altitudes (about 1.2 kg/m^3 at sea level) and decreases with increasing altitude (about 5.6×10^{-7} kg/m^3 at an altitude of 100 km) (Jacobson, 2005). The atmosphere can be categorized into lower, middle and upper regions.

The lower part of the atmosphere, called the troposphere, starts from the ground and extends up to 10 km at high latitudes and up to 17 km near the equator. This is the meteorologically active layer where most of the water vapour and dust are found (Ondoh and Marubashi, 2001). The middle part of the atmosphere includes the stratosphere and the mesosphere, which are found between 10 and 85 km. This part of the atmosphere contains the ozone layer that blocks ultraviolet (UV) radiation from the Sun. The Earth's upper atmosphere starts from an altitude of 85 km, including the thermosphere and the exosphere (Moldwin, 2008). The Earth's lower atmosphere is neutral while the upper part is ionized and known for its conductive behaviour. The transition from neutral to ionized atmosphere is determined by how far energetic particles and high-energy photons such as UV light and X-rays that are coming from the sun and outer space penetrate Earth's atmosphere.

The ionosphere, extends from an altitude of approximately 50 km to about 1,000 km, has a significant effect on trans-ionospheric signals used for radio communication and navigation (El-Rabbany, 2002; Moldwin, 2008). In the following sections, we will briefly discuss the formation and composition of the ionosphere, its importance for radio communication and the errors that can be introduced in trans-ionospheric signals.

2.2 Ionosphere

The ionosphere contains free electrons formed primarily due to the ionization of the atmospheric molecules and atoms by extreme ultraviolet (EUV) radiation from the sun. The process of photons ejecting electrons from a neutral atom to create free electrons and positively charged ions is called photo-ionization (McNamara, 1991). The photo-ionization process can be expressed as

$$X + h\nu \rightleftharpoons X^+ + e, \tag{2.1}$$

where X represents an atom or a molecule and $h\nu$ is a photon, which will produce free ions (X^+) and electrons (e).

The ionosphere is a naturally dynamic medium with an electron density that varies with time of day, season, geographical location and solar activity (Georges, 1969). The ionosphere was discovered in 1901 by Marconi when he was sending radio signals across the Atlantic. In 1902, Kennelly, and Heaviside and Lodge, separately, suggested that the ionosphere reflects electromagnetic waves because of the free electrons that are produced by solar radiation (Kohl *et al.*, 1996). Before 1926, the ionosphere used to be known as the Heaviside layer or the Appleton layer (Kohl *et al.*, 1996).

The formation of an ionised layer in the atmosphere depends on the intensity of the EUV light and the density of neutral atoms. As the altitude increases the concentration of neutral atoms decreases due to the decreasing gravitational force. The intensity of the EUV light from the sun decreases at lower altitudes because of absorption. Due to the balance, between increasing density and decreasing EUV intensity, as one gets closer to the surface of the Earth, there is a particular altitude where there is a maximum rate of production of free electrons (McNamara, 1991). The penetration depth of the EUV radiation through the atmosphere and the electron density of the ionospheric regions is shown in Figure 2.1.

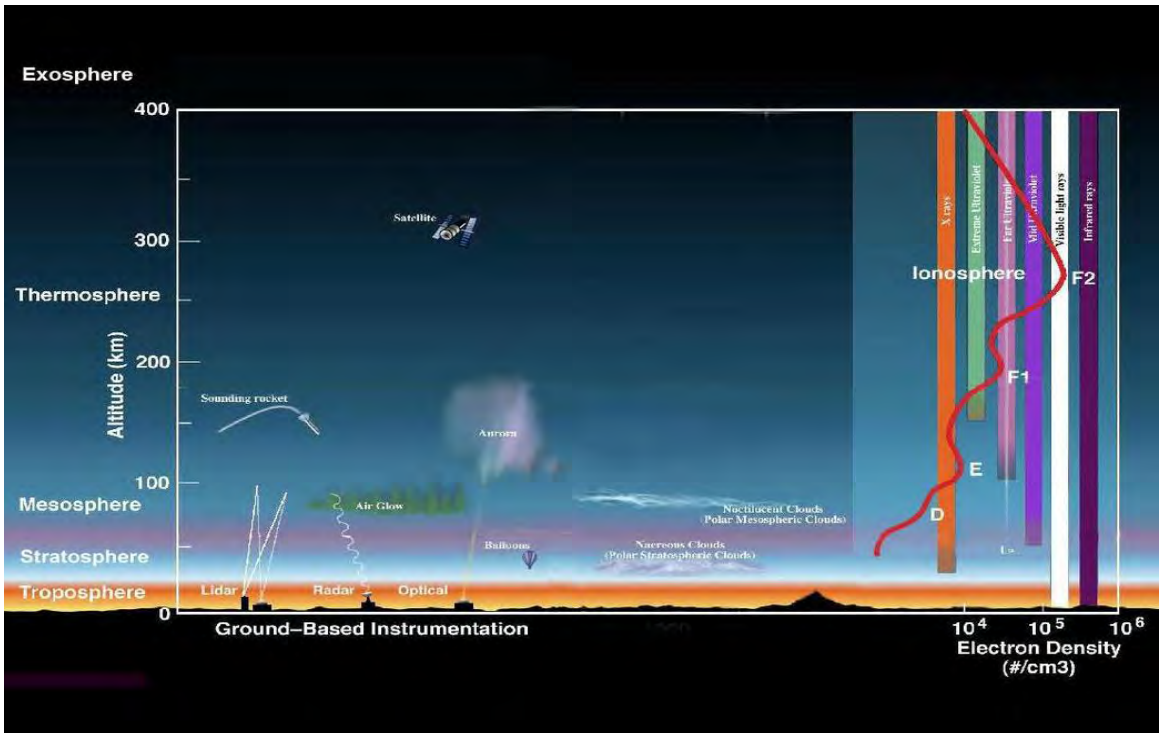

Figure 2.1: Layers of Earth's atmosphere, including the ionosphere and showing the electron density of each region and the penetration depth of the different types of solar radiation (Credit: NASA/Goddard (Zell, 2013)).

The Chapman function in equation Equation 2.2 (in simplified form) describes the production rate of free electrons in a simple ionospheric layer:

$$q = q_o exp[1 - Z - sec\chi exp(-Z)], \tag{2.2}$$

where Z is the reduced height for the neutral gas given as $Z = (h - h_o)/H$, H being the scale height, h_o is the height of the maximum rate of production when the Sun is overhead, and χ represents the solar zenith angle (when $\chi = 0$ it means the sun is overhead) and q_o is the production rate at h_o, also when the Sun is overhead.

The production rate of ions depends strongly on the intensity, which gives rise to its diurnal variation. The maximum production rate occurs at height (Z_m) (Davies, 1990)

$$Z_m = ln(sec(\chi)), \tag{2.3}$$

where χ is the solar zenith angle. Therefore, by substituting equation Equation 2.3 into equation Equation 2.2, we get the peak production rate for ions as:

$$q_m = q_o cos(\chi). \tag{2.4}$$

The electron density in the ionosphere shows variations with time of day, season, altitude, latitude, and solar activity because the production rate of free electrons depends on the intensity of the photons and on the number of neutral atoms (McNamara, 1991). At high latitudes precipitation of energetic particles through the magnetosphere contributes to the production of free electrons in the ionosphere through a process called collision ionization (Hunsucker and Hargreaves, 2003; McNamara, 1991). Most of the ionospheric variation has to do with the intensity of the UV radiation, especially for diurnal and seasonal variation, which is also directly related to the position of the sun in the sky. Variation of the ionosphere with respect to altitude is the result of both the variation of the photon intensity and density of neutral atoms at different altitudes. The latitudinal and solar activity dependence corresponds to the precipitation of energetic particles into the atmosphere, which dominates during high solar activity and mostly at high latitudes.

Electron density in the ionosphere depends on the relative speed of the production and loss processes from the recombination and attachment processes. In the upper part of the ionosphere, free electrons get lost by combining with positively charged ions to produce neutral atoms, this process is called recombination (McNamara, 1991). In the lower ionosphere electron loss is caused by the attachment process in which electrons are attached to neutral atoms and produce negatively charged ions (McNamara, 1991).

The continuity equation (Equation 2.5) expresses the rate of change in electron density of terms of the production and loss rates in the ionosphere (Hunsucker and Hargreaves, 2003).

$$\frac{\partial N}{\partial t} = q - L - div(N\mathbf{v}), \tag{2.5}$$

where q is the production rate (per unit volume), L is the rate of loss by recombination,

$div(N\mathbf{v})$ is the loss of electrons by movement and $\mathbf{v}$ is the mean drift velocity.

Based on the ionization level, the ionosphere is divided into 4 layers called the D, E, F1 and F2 layers (see Figure 2.1). During night time the D, E, and F1 layers tend to completely disappear (see Figure 2.2) due to the increase in the loss rate of free electrons and the decrease in the production rate of ions since there is no photo-ionization at night. The F2 layer persists through the night-time because the ionosphere drifts to higher altitudes after sunset (see Figure 2.2). At higher altitudes, the recombination is less effective and there will still be an ionised layer which can be used for HF radio communication during night time (McNamara, 1991).

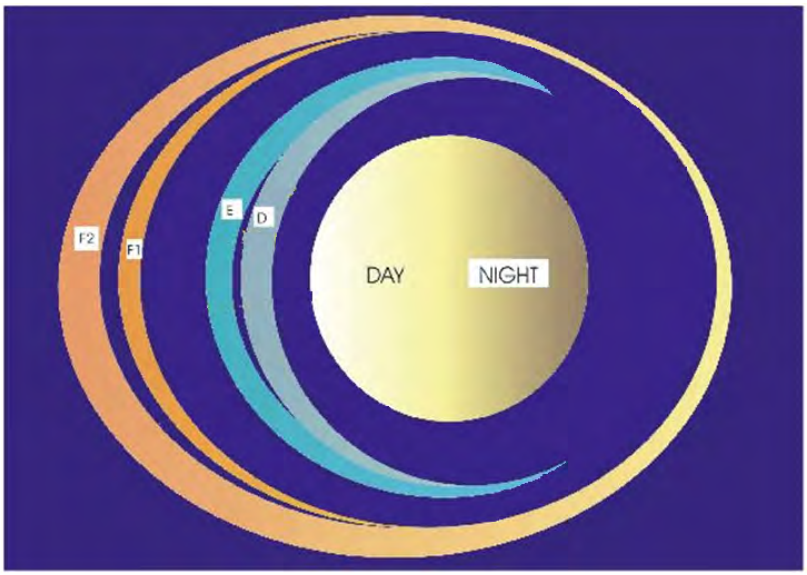

Figure 2.2: Layers of the ionosphere during the day and night time (Not drawn to scale).

The D layer is the lower part of the ionosphere, ranging approximately from 50 km to 90 km altitude. The D region has the property of absorbing lower frequency radio signals which degrade long-distance HF radio communication. The main sources of ionization in the D layer are ionization of nitric oxide by EUV photons, ionization of molecular nitrogen and oxygen by solar hard X-rays and cosmic rays (Moldwin, 2008). Because of the relatively high concentrations of neutral atoms at D-layer altitudes the rate of recombination is higher than in the F-layer. This is the cause of the disappearance of the D layer at night (Moldwin, 2008).

The E layer of the lower ionosphere is located between 90 km and 140 km in altitude (Ondoh and Marubashi, 2001). In this region, the production of free electrons is mainly due to ionization of molecular oxygen by low energy or soft X-ray and solar UV radiation. Precipitation of energetic particles also contributes to the ionization of the E layer. Precipitation is usually more significant at high latitudes. Since the E region is found at higher altitudes than the D region, the peak electron density in this region is 100 times greater than in the D region. The E region also disappears at night-

time because of the loss of electrons by dissociative recombination and attachment (McNamara, 1991; Moeketsi, 2007).

The F layer extends from 120 km to 1000 km and has a peak density at approximately 300 km (Moldwin, 2008). The F layer is mainly produced by solar UV ionization of atomic oxygen and is therefore dominated by oxygen ions (O^+). The F layer contains atomic ions while the D and E layers are dominated by molecular ions which have a higher recombination rate than atomic ions (Hunsucker and Hargreaves, 2003; Moldwin, 2008). Molecular ions have a much higher recombination rate because molecular ions can combine with electrons and give two neutral atoms through a process called dissociative recombination (McNamara, 1991). Therefore, in order to have a dissociative recombination in the F layer, the atomic ions first have to be converted to molecular ions (Hunsucker and Hargreaves, 2003). During the daytime, especially in the summer and when there are a low number of sunspots, the F layer splits into two layers, the F1 and F2 layers (Davies, 1990; Hunsucker and Hargreaves, 2003). The peak electron density is higher in the F2 layer than the F1 layer (Moldwin, 2008).

2.3 Terrestrial radio propagation

The free electrons in the ionosphere refract radio waves. The use of the ionosphere for terrestrial HF radio communication depends on the electron density of the ionosphere, which determines the critical frequency where the signal gets reflected back to Earth by the ionosphere (McNamara, 1991). This critical frequency is calculated from the plasma frequency and depends on the electron density.

The plasma frequency $f_N = \omega/2\pi$ is related to the electron density by

$$f_N = \frac{e}{2\pi(\epsilon_o m)^{1/2}} N^{1/2}, \tag{2.6}$$

where $\omega = Ne^2/\epsilon_o m$ is the angular frequency, N is the electron density per m^3, e is charge on an electron, m is the mass of the electron and ϵ_o is the permittivity of free space.

The critical frequency of each layer can be related to the maximum electron density in that layer by the following equation (after substituting for $m_e = 9.11 \times 10^{-31}$ kg, $\epsilon = 8.854 \times 10^{-12}$ Fm^{-1} and $e = 1.602 \times 10^{-19}$ Coulombs)

$$f_c \approx 9 \times 10^{-6} N_m^{1/2}, \tag{2.7}$$

where f_c is in MHz and N_m is in electrons per m^3. This means that if the F2 layer has a maximum electron density value of $10^{12}/\mathrm{m}^3$ the critical frequency of the F2 layer is 9 MHz, which is the maximum frequency of signals that can be reflected from the

F2 layer at vertical incidence (McNamara, 1991).

2.4 Trans-ionospheric radio wave propagation

Radio signals can propagate through the ionosphere as long as the frequency of the transmitted signal is greater than the critical frequency of the F2 layer. There are different phenomena that can be observed during the interaction of radio waves with matter, including reflection, refraction, diffraction, dispersion, scattering, change of polarization and attenuation (Hunsucker and Hargreaves, 2003). For trans-ionospheric signals the phase, the intensity and polarization can be significantly affected by the ionosphere. The effects are more pronounced for signals at low frequency (Hunsucker and Hargreaves, 2003). The ionosphere causes radio wave propagation delay and phase advance and fluctuation in signal strength, all of which are contributing factors to scintillation (Ondoh and Marubashi, 2001).

During the propagation of a radio wave in the ionosphere, electrons absorb energy from the wave and oscillate with the same frequency as the radio wave. If an oscillating electron collides with a heavy neutral atom it will give up its energy to the atom. In this case the radio wave energy is absorbed or attenuated (McNamara, 1991). Most of the radio signal absorption occurs in the lower part of the ionosphere because the collision frequency increases with decreasing altitude where the density of neutral atoms is higher (McNamara, 1991).

Refractive index of the ionosphere

The ionosphere is a dispersive propagation medium in which the refractive index varies with the frequency of the propagating wave. The Appleton-Lassen equation is used to define the refractive index n of an ionised propagation medium as (Hunsucker and Hargreaves, 2003):

$$n^2 = 1 - \frac{X}{1 - jZ - \frac{Y_T^2}{2(1-X-jZ)}} \pm \left(\frac{Y_T^4}{4(1-X-jZ)^2} + Y_L^2\right)^{1/2}, \tag{2.8}$$

where j is $\sqrt{-1}$, and $+$ denotes the ordinary and $-$ the extraordinary wave. Ordinary waves are independent of the direction of the magnetic field, while extraordinary wave motion gets modified because of the force exerted by the magnetic field normal to the direction of propagation (Francis and Karplus, 1960). In equation Equation 2.8 X, Y and Z are the dimensionless quantities,

$$X = \omega_N^2/\omega^2, \tag{2.9}$$

$$Y = \omega_B/\omega, \tag{2.10}$$

$$Z = \nu/\omega, \tag{2.11}$$

where ω is the radial frequency, ω_N is the plasma frequency in radians, ν is the collision frequency (in s^{-1}), $\omega_B = \mathbf{B}e/m_e$ is the gyration frequency of an electron in a magnetic field with flux density $\mathbf{B}$ (W m^{-1}).

For the special case, where collisions and magnetic field effects are negligible, the Appleton-Lassen equation (Equation 2.8) can be written as,

$$n^2 \cong 1 - X, \tag{2.12}$$

where the Y and Z components are zero since they depend on the magnetic field and collisions, respectively. For radio frequencies higher than the plasma frequency, $X << 1$, therefore Equation 2.12 can be approximated by the first term in the Taylor series expansion and written as,

$$n \cong (1 - X)^2 = 1 - \frac{\omega_N^2}{2\omega^2}. \tag{2.13}$$

Substituting the plasma frequency $\omega_N^2 = Ne^2/(\epsilon_o m)$ in equation Equation 2.13 gives the refractive index of the ionosphere as follows:

$$\begin{aligned} n &= (1 - X)^2 \\ &= 1 - \frac{Ne^2}{2\epsilon_o m_e \omega^2} \\ &= 1 - 40.30\frac{N(m^{-3})}{[f(Hz)]^2}. \end{aligned} \tag{2.14}$$

Phase and group velocity

Signals that propagate through a non-dispersive medium will have phase and group velocity equal to the speed of light. For GNSS signals, the phase and group velocities are not equal because of the dispersive behaviour of the ionosphere at L-band frequencies. The phase velocity ν_{ph} and the group velocity ν_{gr} depend on the frequency and wavelength of the signal (Opperman, 2007).

$$\nu_{ph} = \lambda f, \tag{2.15}$$

$$\nu_{gr} = -\frac{df}{d\lambda}\lambda^2. \tag{2.16}$$

There will be a group delay relative to a wave travelling at the speed of light due

to the group velocity being less than the speed of light ($\nu_{gr} < c$). There is likewise a phase advance because the refractive index is less than unity and the phase velocity is greater than the speed of light. The phase advance is proportional to the number of electrons in a column of unit cross section along the propagation path, which is known as the Total Electron Content (TEC). For an electron density N along a path l, the TEC can be expressed as $I = \int N dl$. In numerical form the phase advance is

$$\phi = (8.45 \times 10^{-7}) I/f, \tag{2.17}$$

where f is in Hz and I is the TEC in electron/m^{-2}. Normally the TEC is expressed in TEC units (TECu) where 1 TECu= 10^{16} electrons/m^2.

Taking the full derivative of the phase velocity given in Equation 2.15 results in an equation that relates the phase and group velocity as follows

$$d\nu_{ph} = f d\lambda + \lambda df, \tag{2.18}$$

which after dividing by $\lambda d\lambda$ can be written as

$$\frac{df}{d\lambda} = \frac{1}{\lambda}\frac{d\nu_{ph}}{d\lambda} - \frac{f}{\lambda}. \tag{2.19}$$

Substitution of equation Equation 2.19 into Equation 2.16 gives

$$\nu_{gr} = -\lambda \frac{d\nu_{ph}}{d\lambda} + \nu_{ph}, \tag{2.20}$$

which shows that the group velocity is less than the phase velocity by an amount which depends on the wavelength.

Polarization

The polarization angle rotates as the wave travels through the ionosphere (Erickson *et al.*, 2001; Hunsucker and Hargreaves, 2003). Rotation in the plane of polarization, due to the electron density in the ionosphere, is called Faraday rotation (Ondoh and Marubashi, 2001). For a linearly polarized wave travelling a distance l the change in the polarization angle (Ω) of the wave is given by (Hunsucker and Hargreaves, 2003)

$$\Omega = \frac{2.365 \times 10^4}{f^2} \int \mathbf{B}_L N dl, \tag{2.21}$$

where l is the distance, N is the electron density in electrons/m^3 and $\mathbf{B}$ is the magnetic field in Webers/m^2.

2.5 Scintillation

Scintillation is the rapid fluctuation in amplitude, phase, polarization and angle of arrival of a trans-ionospheric radio signal (Davies, 1990; McNamara, 1991). Scintillations are caused by a relative phase shift in the propagation wavefront and by diffraction, as the result of irregularities of the electron density in the ionosphere (Hunsucker and Hargreaves, 2003). Signals that pass through the ionosphere can get both diffracted and refracted because of irregularities with scale lengths from a few metres to a few kilometres (Wanninger, 1993). Strong scintillation is mainly caused by large horizontal gradients in the electron density.

Scintillation can lead to cycle slips of GNSS signals and in severe cases it can prevent the tracking of GNSS satellite signals (Davies, 1990; Wanninger, 1993). Scintillation can cause a reduction in the number of tracked GNSS satellites, which will degrade the accuracy of the computed position. Under severe scintillation conditions, when fewer than four satellites are tracked, there may be temporary loss of navigation service (Carrano *et al.*, 2005).

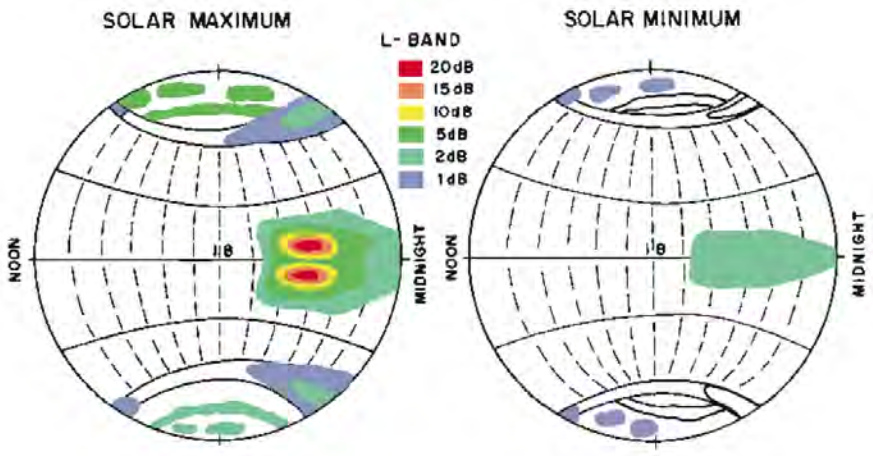

Figure 2.3: Variation of L-band scintillation with geomagnetic latitude, time of day and solar cycle (Basu *et al.*, 2002).

Figure 2.3 depict the scintillation intensity based on the fading depth of L-band radio signals at high, mid- and low latitudes during day and night time for both solar maximum and minimum. Equatorial scintillation is more intense during night time between 20:00 and 02:00 local time than during any other time of the day (see Figure 2.3). Scintillation as observed at the GPS frequencies (L-band) is also related to the breaking up of the F region ionization into small bunches of electrons (or irregularities), which can be seen as the spread F phenomena on ionosonde observations, (McNamara, 1991).

2.5.1 Low-latitude scintillation

Scintillations at low latitudes are generally stronger than at mid- and high latitudes. At the Earth's equatorial region both the electric field and the geomagnetic field are nearly horizontal (McNamara, 1991). The eastward electric field combining with the northward directed magnetic field results in an upward $\mathbf{E} \times \mathbf{B}$ drift of electrons ($\nu_{\mathbf{e}\perp} = \frac{\mathbf{E}\times\mathbf{B}}{B^2}$) during day time (Kelley and Heelis, 1989; Ondoh and Marubashi, 2001). As the electrons move upward because of the $\mathbf{E}\times\mathbf{B}$ drift, they encounter the horizontal lines of Earth's magnetic field, which cause poleward diffusion of electrons along the direction of the magnetic lines, as illustrated in Figure2.4 (McNamara, 1991; Ondoh and Marubashi, 2001).

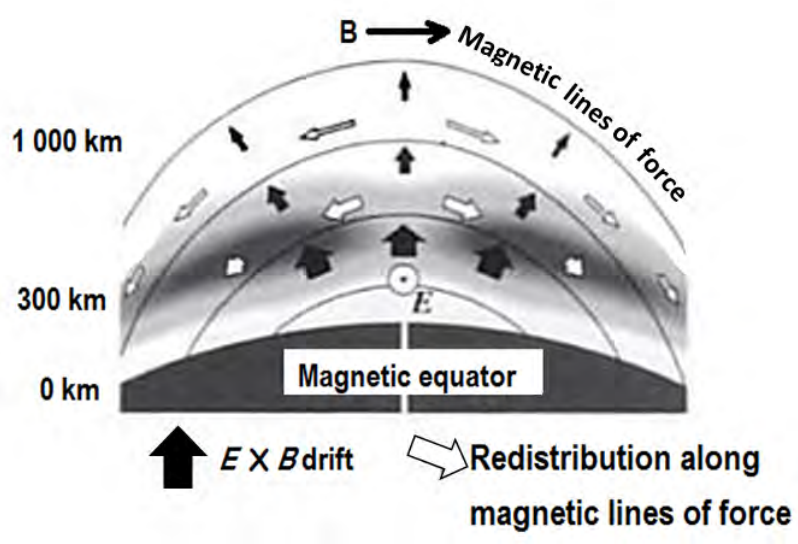

Figure 2.4: Pictorial depiction of the formation of the equatorial anomaly (Ondoh and Marubashi, 2001).

This process of redistributing electrons in the ionosphere, known as the *fountain effect*, is the main reason for the F2 layer critical frequency at the geomagnetic equator to be low and for latitudes between 10° and 20° to have higher critical frequency values than at the geomagnetic equator (Ondoh and Marubashi, 2001). These regions are often termed as the ionospheric equatorial anomaly. The equatorial anomaly starts at sunrise as ionization increases with the rising intensity of the solar radiation and reaches its maximum in the late afternoon and early evening, during the equinoxes and at solar maximum (McNamara, 1991; Ondoh and Marubashi, 2001). During the night-time there will also be an equatorial anomaly even if the direction of the electric field is reversed to westward because the process of redistributing electrons is not reversible (Ondoh and Marubashi, 2001).

The ionospheric variation at low latitudes is highly influenced by the Earth's magnetic field (McNamara, 1991). The ionosphere at low latitude has large horizontal

gradients of electron density and exhibits a rapid increase in density during sunrise (McNamara, 1991). The production of irregularities in the F region during night-time is the cause for high signal scintillation at low latitudes after sunset (McNamara, 1991; Ondoh and Marubashi, 2001).

2.5.2 Mid-latitude scintillation

The least variable and least disturbed ionospheric region is the mid-latitude region. At the mid-latitudes, the region between 20° and 50° geomagnetic latitudes in both hemispheres (Fremouw *et al.*, 1991), scintillation is much less pronounced. Scintillations at mid-latitudes usually occur during magnetic storms and are associated with two phenomena (Kintner *et al.*, 2007). One is the equator-ward movement of the Northern lights over the mid-latitudes during night-time due to precipitation of energetic particles into the neutral atmosphere. The other phenomenon is associated with storm-time ionospheric behaviour and doesn't involve precipitation of charged particles. The second phenomenon involves ionospheric density gradients that are associated with high velocity ionospheric flows sometimes called storm enhanced density (SED) and subauroral polarization streams (SAPS), which mainly occur during daytime (Kintner *et al.*, 2007).

2.5.3 High-latitude scintillation

Besides photo-ionization, the precipitation of energetic particles from interplanetary space into the atmosphere is the main source of ionization in high-latitude regions (Fremouw *et al.*, 1991). Since the magnetic field lines converge at high latitudes, charged particles that spin around the field lines will be introduced to Earth's atmosphere (Moldwin, 2008). Due to precipitation at high latitudes, ionospheric scintillation is more likely to occur here than at the mid- and low-latitude regions.

At high latitudes, strong scintillation effects are observed due to ionospheric irregularities caused by geomagnetic storms (Aquino *et al.*, 2005). The region between 64° and 70° geomagnetic latitude, known as the auroral zone, is also a region of enhanced scintillation due to the prevalence of irregularities associated with precipitation (Davies, 1990; Wanninger, 1993). The auroral zone moves closer to the mid-latitudes during intense geomagnetic disturbances (or geomagnetic storms) (McNamara, 1991; Wanninger, 1993). More intense scintillations are observed near midnight during the equinox season spanning March, April and May in the Northern hemisphere, both during quiet and disturbed magnetic conditions (Davies, 1990). Scintillation in this region, primarily affects the carrier phase resulting in an increase in the number of cycle slips (Wanninger, 1993).

2.6 Fresnel zones

The scattering effect of the irregularities in the density of free electrons in the ionosphere modifies the phase and amplitude of trans-ionospheric radio waves (Beach, 1998). Scattered radio waves spread out in every direction as they propagate. According to Huygens′ principle, each part of a wavefront can be a source of new wavelets whose superposition builds up a wavefront at further points (Hunsucker and Hargreaves, 2003), as depicted schematically in Figure 2.5.

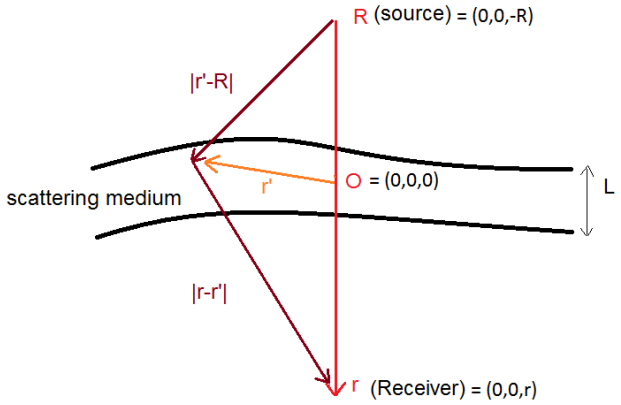

Figure 2.5: The single scattering effect from a thin layer of irregularities with thickness L which is located perpendicular to the line between the source and the receiver, where $|\mathbf{r}-\mathbf{r}'|+|\mathbf{r}'-\mathbf{R}|$ is the length of the piecewise straight line path from $\mathbf{R}$ to $\mathbf{r}'$ and then to $\mathbf{r}$ (figure adapted from Beach (1998)).

Waves propagating into the scattering medium can interact with fluctuations in permittivity ϵ_1. The integral in Equation 2.22 represents the scattering effect on a propagating wave through an irregular medium summed over all possible interaction points.

$$I = \int d\mathbf{r} G_o(\mathbf{r}-\mathbf{r}')\epsilon_1(\mathbf{r}')G_o(\mathbf{r}'-\mathbf{R}), \tag{2.22}$$

where the inhomogeneous Green's function $G_o(\mathbf{r}'-\mathbf{R})$ is given as

$$G_o(\mathbf{r}'-\mathbf{R}) = \frac{exp(ik|\mathbf{r}'-\mathbf{R}|)}{4\pi|\mathbf{r}'-\mathbf{R}|}, \tag{2.23}$$

where k is wave number. Substitution of equation Equation 2.23 into Equa-

tion 2.22 gives

$$I = \frac{1}{16\pi^2} \int d\mathbf{r}' \frac{exp[ik(|\mathbf{r} - \mathbf{r}'| + |\mathbf{r}' - \mathbf{R}|)]}{|\mathbf{r} - \mathbf{r}'||\mathbf{r}' - \mathbf{R}|} \epsilon_1(\mathbf{r}'). \tag{2.24}$$

The main contribution to the integral comes from the paths which are closer to the direct line between the source and the receiver as shown in Figure 2.5. The larger the $\mathbf{r}'$ the more rapid the variation of the phase along the path. Since the exponential over a cycle is zero, the contribution to the integral from larger $\mathbf{r}'$ becomes negligible (Beach, 1998).

The scale of irregularities that are more prone to cause interference corresponds to the Fresnel zone radius, r, which depends on the wavelength, λ and the distance h from the plane of the irregularities to the receiving point $r = \sqrt{h\lambda}$ (Hunsucker and Hargreaves, 2003; Ondoh and Marubashi, 2001; Rawer, 1993). Here the plane of the irregularities represent the ionosphere. Therefore, ionospheric irregularities with a particular size of 250 m can cause fluctuations of trans-ionospheric signals with a 1.57 GHz carrier frequency (Ledvina *et al.*, 2002). The Fresnel zones are concentric circular rings, where the outer edge of one ring has a distance to the receiver which is half a wavelength greater than the inner ring, as illustrated in Figure 2.6, where $\lambda/2$ is the distance in which the phase difference of the wave becomes 180° (Hunsucker and Hargreaves, 2003).

The square of the radius of the k^{th} Fresnel zone $r_f(k)$ is given by Equation 2.25 (Rawer, 1993).

$$\begin{aligned} r_f(k)^2 &= (h + \frac{1}{2}\lambda k)^2 - h^2 \\ &= kh\lambda + \frac{1}{4}(k\lambda)^2 \\ &\approx kh\lambda. \end{aligned} \tag{2.25}$$

Since the L-band wavelength is small compared to the height of the ionosphere (h), the second term ($\frac{1}{4}(k\lambda)^2$) can be ignored to get to $r_f(k)^2 \approx kh\lambda$.

Immediately after the radio waves pass through the plane of irregularities only the phase of the signal changes, but as it propagates further away from the plane of irregularities adjacent signals with different phase will start to interfere constructively and destructively. By the time the signal reaches the ground, a spatial variation in the electric field strength of the signal can be observed (Ondoh and Marubashi, 2001). If the observer is far enough from the plane where the irregularities lie, perturbation of both phase and amplitude will be observed on the received signal on the ground (Hunsucker and Hargreaves, 2003). Irregularities with scale length less than the

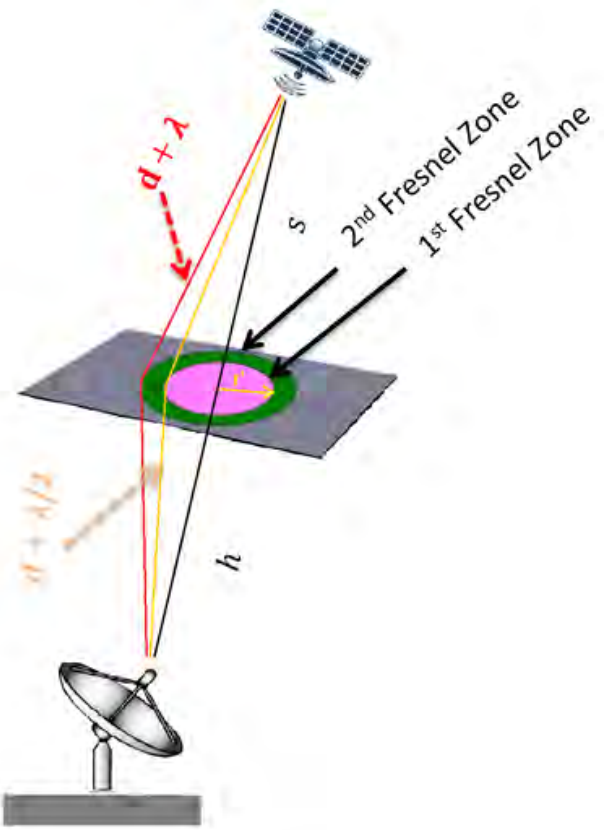

Figure 2.6: Pictorial representation of the Fresnel zones for a plane of irregularities found between the transmitter and the receiver separated by a distance $d = h + s$, the interference of the irregularities from the first and second Fresnel zones, and the line of sight of the wave propagation.

first Fresnel zone produce both amplitude and phase scintillation, while irregularities larger than the first Fresnel zone produce phase scintillation only (Hunsucker and Hargreaves, 2003).

In the next section we will briefly discuss the phase and amplitude scintillation indices that are used to measure the intensity of the scintillation effect on a received signal.

2.7 Scintillation parameters

- **Amplitude Scintillation (S_4 index)**
  The amplitude of radio signals depends mainly on ionospheric absorption, distance attenuation, focusing/defocusing and the coupling between the wave and

the antenna (Davies, 1990). Amplitude scintillations are observed as fading and enhancement of signal intensity. Such scintillation can cause errors in decoding the GPS data message and also in estimating the range (Carrano *et al.*, 2005; Wanninger, 1993). When signals fade below the receiver's lock threshold, which depends on the bandwidth of the GNSS receiver system and on the type of the tracking channel (Wanninger, 1993), it will cause loss of lock on signals coming from the satellite. In the worst case of amplitude scintillation, for deep and long-duration signal fading, it will be difficult to acquire the satellite in the first place (Beach, 1998; Shanmugam *et al.*, 2012). The amplitude of the received signal shows short-term fluctuations caused by the interference effects coupled with ionospheric motion and also long-term variation because of the change in the absorption level in the D region (Davies, 1990). Amplitude scintillation can be derived from the signal-to-noise ratio (S/N) data (Wanninger, 1993).

The S_4 index is a measure of the signal amplitude root-mean-square fluctuations or the deviation of its intensity compared to the mean value of the intensity (Beach, 1998; Kintner *et al.*, 2004). As shown in Briggs and Parkin (1963) there are different measurements of amplitude scintillation. The mathematical expressions used to calculate the amplitude scintillation using both mean deviation and root mean square deviation are given as follows (Briggs and Parkin, 1963),

$$S_1 = \frac{\overline{|A - \overline{A}|}}{\overline{A}}, \tag{2.26}$$

$$S_2 = \frac{\left(\overline{(A - \overline{A})^2}\right)^{1/2}}{\overline{A}}, \tag{2.27}$$

$$S_3 = \frac{\overline{|I - \overline{I}|}}{\overline{I}}, \tag{2.28}$$

$$S_4 = \frac{\left(\overline{(I - \overline{I})^2}\right)^{1/2}}{\overline{I}}. \tag{2.29}$$

Equations Equation 2.26 and Equation 2.28 give the mean deviation formulas. Equations Equation 2.27 and Equation 2.29 give the root mean square deviation formulas. Here A represents the signal amplitude while I is power or intensity, which is the square of the amplitude (A^2). After some mathematical manipulation the S_4 index given in Equation 2.29 can be written as

$$S_4 = \sqrt{\frac{(\overline{I^2} - \overline{I}^2)}{\overline{I}^2}}, \tag{2.30}$$

which is the standard deviation of the received power (or intensity) normalized by the mean value of the signal power. For a strong fluctuation in phase the

deviation of intensity is equal to the mean value of the intensity, therefore S_4 approaches unity (Beach, 1998; Datta-Barua *et al.*, 2003).

- **Phase Scintillation (σ_ϕ index)**

  Sudden changes in refraction or diffraction by the ionosphere can cause phase scintillation for signals that pass through the ionosphere (Wanninger, 1993), which are observed as rapid fluctuations on the phase of the received signal. Phase scintillation stresses the ability of the phase-lock loops of the receiver to maintain lock, which might lead to a loss of phase lock and frequent cycle slips (Carrano *et al.*, 2005; Groves *et al.*, 1997; Shanmugam *et al.*, 2012; Wanninger, 1993). The phase scintillation index is calculated by taking the standard deviation of linearly de-trended phase data, quantified by the phase scintillation index σ_ϕ. The mathematical expression of the σ_ϕ index is given as follows (Beach, 2006):

$$\sigma_\phi = \sqrt{< \phi^2 > - < \phi >^2}, \tag{2.31}$$

  where ϕ is the signal phase and $<>$ represents the mean value, typically taken over a period of 1 minute.

2.8 Global Navigation Satellite Systems

Global Navigation Satellite Systems (GNSS) comprise constellations of satellites designed to provide global positioning and timing information for users on Earth or in space. There are currently four GNSS systems developed by different countries: GPS (USA), GLONASS (Russia), Galileo (EU) and COMPASS/Beidou (China).

The Global Positioning System (GPS) was started in the late 1970s using a few satellites for various test roles and the final constellation was declared operational on April 27, 1995 (Gleason and Gebre-Egziabher, 2009). GPS satellites orbit the Earth at an orbital radius (distance from the centre of mass of the Earth to the satellite) of approximately 26,600 km using a nearly circular orbit with inclination of 55° (Misra and Enge, 2006; Mohinder *et al.*, 2001). Currently, there are 24 operational GPS satellites occupying six evenly spaced orbital planes, four satellites per plane (Hofmann-Wellenhof *et al.*, 1992; Kaplan and Hegarty, 2006). GLONASS (Global Orbiting Navigation Satellite System) was developed by the Russian Federation (Mohinder *et al.*, 2001). Its first satellite was set in orbit in 1982 with an orbital altitude of 19,100 km. GLONASS has 24 operational satellites using three orbital planes, eight satellites per plane, with a 64.8° inclination angle (Mohinder *et al.*, 2001). Galileo is designed and controlled by the European Union and the European Space Agency. The first two Galileo satellites were launched in 2011 (Gleason and Gebre-Egziabher, 2009; Kaplan and Hegarty, 2006). Galileo will have three orbital planes spread evenly with an inclination angle of 56° at an altitude of 23,222 km. The COMPASS/Beidou system was designed and implemented by China. It is currently in its in-orbit vali-

dation phase (Gleason and Gebre-Egziabher, 2009). COMPASS/Beidou will provide global coverage using 5 geostationary and up to 30 medium Earth orbit satellites in its full operational constellation (Gleason and Gebre-Egziabher, 2009).

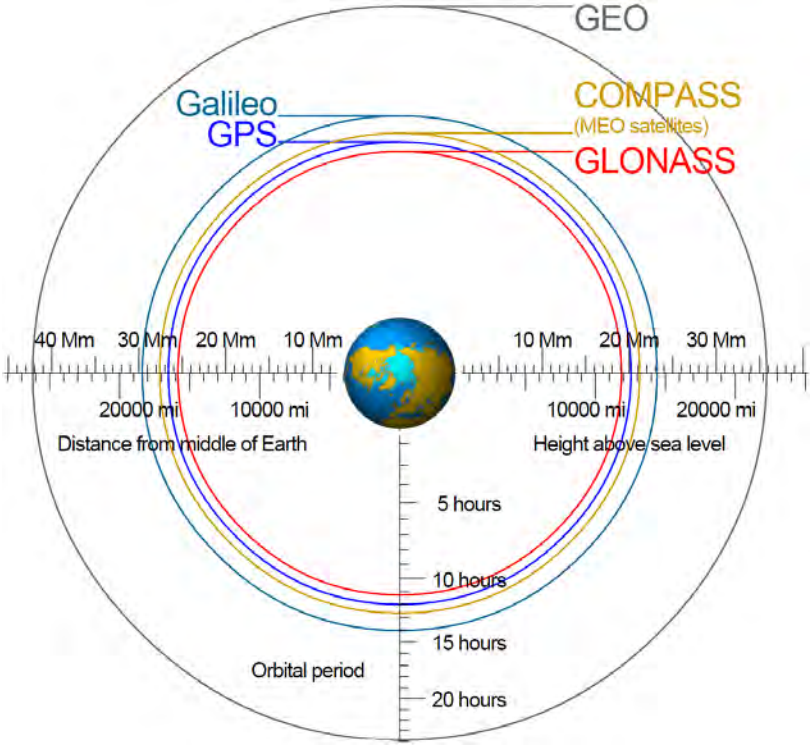

Figure 2.7: The orbital altitudes and orbital periods of GPS, Galileo, GLONASS, COMPASS/Beidou and GEO (Geostationary) satellites (Cmglee, 2011).

Since in this dissertation we will concentrate on using GPS signals, we describe this system in more detail below.

2.8.1 Global Positioning System (GPS)

The Global Positioning System (GPS) is a space-based satellite navigation system which quickly and accurately provides 24/7 information on position (in three dimensions), time and velocity anywhere on the globe (El-Rabbany, 2002; Farrell and Barth, 1999; Gleason and Gebre-Egziabher, 2009; Hofmann-Wellenhof *et al.*, 1992; Kaplan and Hegarty, 2006; Misra and Enge, 2006; Mohinder *et al.*, 2001). It is developed and maintained by the United States government's Department of Defence (DoD).

GPS satellites emit coherent radio signals, for broadcasting ranging codes and navigation data, on two L-band channels with carrier frequencies of L1=1.575 GHz and L2=1.227 GHz. Currently there is additional civilian GPS signal with carrier frequency of L5=1.176 GHz, that is part of the modernization of GPS in order to

support aviation safety applications and provide improved availability and accuracy. The modernization includes also the development of the next generation satellite system, known as GPS III, which will improve navigation and timing services and provide advanced anti-jam capabilities with a longer operational lifetime (GPS.GOV, 2015; McDonald, 2002). The GPS signals are right-hand circular polarized (Elósegui *et al.*, 1995; Kaplan and Hegarty, 2006; Mohinder *et al.*, 2001). Navigation data modulated onto the ranging signal is used by receivers to determine the location of the satellite at the time of signal transmission. The satellite-to-user range is determined from the transit time of the signal calculated from the ranging code (Kaplan and Hegarty, 2006). Cesium and/or rubidium atomic clocks are used by GPS satellites to give accurate timing information (Hofmann-Wellenhof *et al.*, 1992; Mohinder *et al.*, 2001).

Each GPS satellite generates a short and a long code referred to as coarse-acquisition (C/A) and precision (P(Y)) code, respectively (Kaplan and Hegarty, 2006). The L1 carrier signal is modulated by two pseudo-random noise (PRN) sequences: the P code with a chip frequency of 10.23 MHz and the C/A code with a chip frequency of 1.023 MHz. The L2 channel is modulated using the C/A code only (Elósegui *et al.*, 1995; Hofmann-Wellenhof *et al.*, 1992). The main advantage of using two carrier signals, L1 and L2 with different frequencies, is to measure the propagation delay of the signals relative to signals propagating at the speed of light in free space. Because the ionosphere is dispersive, the propagation delay is related to the inverse square of the signal frequency (Mohinder *et al.*, 2001). We can correct for the ionospheric delays using the information from both the L1 and L2 signals. For military receivers the ionospheric correction can be done by comparing the P-code pseudorange measurements obtained on the L1 and L2 frequencies, whereas civilian users can estimate the ionospheric delay by comparing the L1 and L2 phase measurements, since they don't have access to the P-code (Mohinder *et al.*, 2001).

GPS is a dual-use system which provides positioning and navigation services for both civilian and military use. The C/A-code, modulated on the L1 frequency only and designated as the Standard Positioning System (SPS), is available for civilian use (Hofmann-Wellenhof *et al.*, 1992). The P-code, which is modulated on both carriers L1 and L2, is designated as the Precise Positioning Service (PPS) and has been reserved for U.S military and other authorized users (Hofmann-Wellenhof *et al.*, 1992).

2.8.2 GPS measurements

GPS receivers log several observables, including the code information (C1, P1 and P2) and carrier phase information (L1 and L2) (Hofmann-Wellenhof *et al.*, 1992). GPS receivers track the signal code and carrier phase with a tracking loop and calculate the propagation time from the code and the time of arrival of the signal (Kintner

et al., 2004).

Pseudorange measurement

The pseudorandom noise sequence generated by a GPS satellite transmitter is embedded with the time information which provides the time of code transmission based on the onboard atomic clock of the satellite. Each GPS satellite is assigned a unique PRN code which is reset each week at midnight from Saturday to Sunday. Therefore, when a GPS receiver picks up the signal it will read the transmission time of the signal and use the receiver's clock to determine the arrival time of the signal. From the transmission and arrival times, the satellite-to-user propagation time of the signal can be calculated (El-Rabbany, 2002; Misra and Enge, 2006). Using the satellite-to-user propagation time and multiplying it by the speed of light, which is the speed of radio signals in free space, yields the satellite-to-user range called the pseudorange (El-Rabbany, 2002; Kaplan and Hegarty, 2006). The accuracy of the estimated satellite-to-user propagation time depends on the synchronism of the satellite and the receiver clocks (Misra and Enge, 2006).

Carrier phase measurements

Carrier phase tracking provides a measurement of the received carrier phase relative to the phase of a sinusoidal signal generated by the receiver clock (Misra and Enge, 2006). The carrier phase can be used to provide the satellite-to-user range by multiplying carrier wavelength (19 cm for L1 and 24.4 cm for the L2 carrier) with the total number of full carrier cycles, including fractional cycles at the receiver and the satellite (El-Rabbany, 2002). The carrier measurement allows for more accurate range determination than using only the code measurements (Mohinder *et al.*, 2001). The pseudorange measurements determined using the carrier phase are ambiguous, but the ambiguity can be resolved using the pseudorange measurements determined from the code observables, which gives an absolute distance. This is because the carrier phase measurements, being derived from a fractional phase counter, have a better resolution than the code measurements which are based on the receiver clock (El-Rabbany, 2002; Rife *et al.*, 2008). Carrier phase measurement can also be used to accurately determine user velocity from the phase rate (Mohinder *et al.*, 2001).

2.8.3 GPS system segments

GPS consists of three main segments: the space segment, the ground-control or monitoring segment and the user segment (see Figure 2.8).

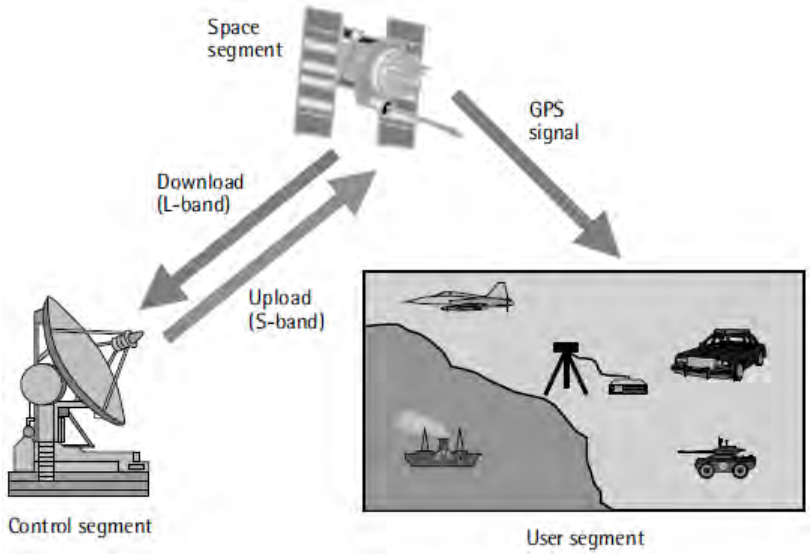

Figure 2.8: GPS main segments: ground-control segment, space segment and user segment (El-Rabbany, 2002).

User segment

The user segment comprises the GPS receivers, which use the L-band signals transmitted from the satellites to determine the user's position, velocity and time (Kaplan and Hegarty, 2006). A GPS receiver unit consists of an antenna, receiver, processor, control display unit, and a power supply (see Figure 2.9).

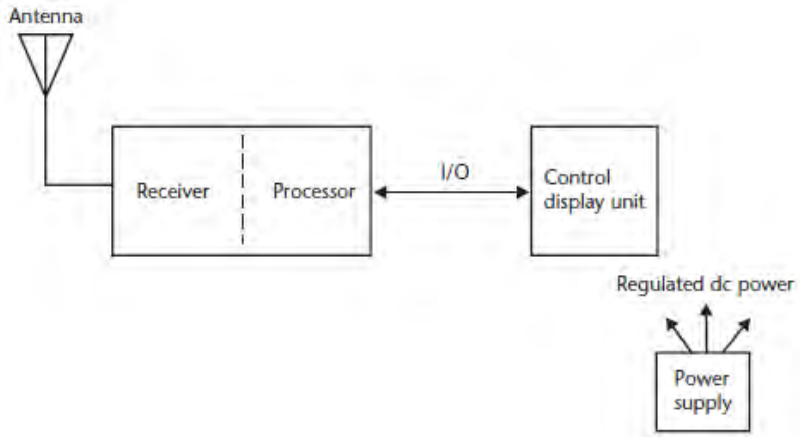

Figure 2.9: Basic components of the GPS user segment (Kaplan and Hegarty, 2006).

There are two basic types of receivers; dual-frequency receivers, that can track the L1 C/A codes and P(Y) code on L1 and L2 and single-frequency receivers, that can only track the C/A code (Kaplan and Hegarty, 2006). The antenna is used to receive signals that are coming from satellites, which are right-hand circular polarized. The receiver processor component of the user segment is used to control and command

the receiver through its operational sequence.

The main functions of the I/O interface are to permit operator data entry, and to display status and navigation solution parameters that are forwarded from the receiver processor (Kaplan and Hegarty, 2006). The other part of a GPS receiver system is a power supply, which can be either integral, external, or both.

2.8.4 GPS applications

GPS has many applications, both for military and civilian users. Some of the main GPS applications are location determination, navigation, mapping and tracking. Scientific uses include weather forecasting, earthquake monitoring, environmental protection and characterization of the ionosphere.

GPS is used in aviation for en route navigation and for landing applications. Both demand a very high level of performance in terms of accuracy and robustness (Gleason and Gebre-Egziabher, 2009). The space shuttle used GPS for guidance in all phases of its operation, starting from launch to on-orbit flight, re-entry and landing (Mohinder *et al.*, 2001). GPS is also used as an altitude determination sensor for Low Earth Orbit (LEO) satellites, a technique which is currently being extended to higher altitudes (Gleason and Gebre-Egziabher, 2009).

GPS can also be used to create a Geographic Information System (GIS) map by recording a series of locations (Kaplan and Hegarty, 2006; Mohinder *et al.*, 2001). Spacecraft are used to photograph large areas of the Earth's surface, and GPS can be used to accurately determine the position of the camera at the moment it took the picture (Kaplan and Hegarty, 2006). GIS tools combined with GPS measurements are used to produce accurate regional maps for resource monitoring and management, including forest management, mining and oil exploration.

In geodesy GPS is used for two main types of applications: firstly to observe the primary geodetic control networks that form the basis of all nations' map data and secondly to establish the global geodetic networks that define the international reference frame and monitor the motion of the crust or ice shelves with respect to that frame (Gleason and Gebre-Egziabher, 2009), which requires precision positioning information at the centimeter or millimeter level.

2.9 GPS error sources

The accuracy of GPS positioning, timing and navigation applications is affected by several source of error. In general, GPS error sources can be divided into satellite-related, propagation-related and receiver-related error sources. In addition to signals

that are sent from GPS satellites, which can be used to determine a certain position, there are different sources of radio signals that can be received by GPS receivers and interfere with the desired GPS signals. These interfering signals can result in degradation of the performance of GPS-based applications (Kaplan and Hegarty, 2006). Satellite-related errors include ephemeris (or orbital) errors and satellite clock errors. Ephemeris errors are errors on the estimated positions of satellites, which are introduced from the uncertainty on the model used to calculate forces acting on GPS satellites (El-Rabbany, 2002). Propagation-medium-related error sources include ionospheric irregularities, which are caused by the random change in the electron density of the ionosphere. Ionospheric irregularities cause scintillation on GPS signals which then introduce errors in position estimation. Tropospheric delay is also a source of error introduced by the medium through which GPS signals propagate. One of the receiver-related error sources is multipath signals. Structures that are in the vicinity of the GPS receiver antennas can reflect and refract signals and change the direction of the transmitted signal. Therefore, signals coming from satellites will not only be directly received, but also via different paths, which is called a multipath effect (Hofmann-Wellenhof *et al.*, 1992). In the following sections, errors caused by the multipath effects and ionospheric irregularities will be discussed briefly.

2.9.1 Errors caused by ionospheric irregularities

Small-scale irregularities in the ionosphere scatter radio energy because of the small changes in the index of refraction of the medium (Kintner *et al.*, 2004). Consequent interference effects, constructive and destructive, of signals cause rapid fluctuation in the phase and amplitude of radio signals as they propagate through the ionosphere as shown in Figure 2.10 (Davies, 1990; Mannucci *et al.*, 1999; McNamara, 1991). The severity level of ionospheric scintillation depends on space weather conditions, such as ionospheric storms that result in high gradients in the electron density of the ionosphere.

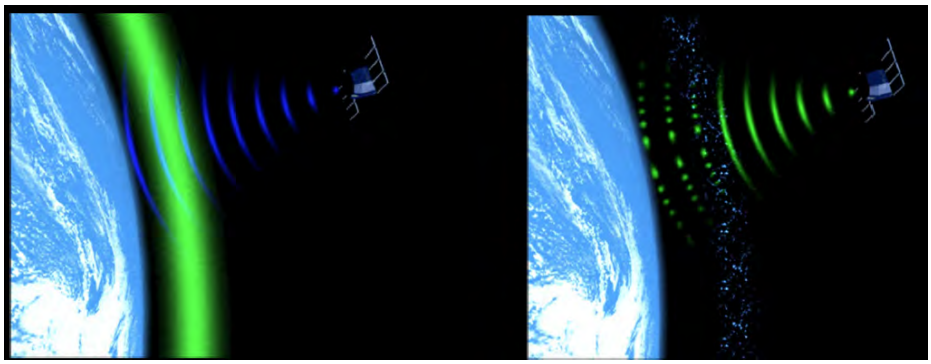

Figure 2.10: Two main effects of the ionosphere on GPS; signal delay (left) and scintillation (right) (credit: Bath university).

The ionosphere is a dispersive medium with respect to radio signals, which causes

the refraction index to be frequency dependent (El-Rabbany, 2002; Misra and Enge, 2006). The dispersive behaviour of the ionosphere causes signals to have different group and phase velocity. The ionosphere causes a decrease in the group velocity that results in a delay of the signal (see Figure 2.10). The delay depends on the particular satellite from which the signal is transmitted (Hofmann-Wellenhof *et al.*, 1992) and on the total electron content (TEC) of the ionosphere along the path of the signal (see Equation 2.32). The ionospheric group delay Δt_{ion} (in seconds), approximated to first order, is given as follows:

$$\Delta t_{ion}(f) = \frac{40.3}{f^2} TEC, \tag{2.32}$$

where f is the carrier frequency (in Hz) and TEC is the Total Electron Content (in TECu) in a 1 m^2 cross-sectional tube along the path of transmission through the ionosphere (Farrell and Barth, 1999).

The propagation delay effect of the ionosphere introduces a significant satellite-to-user range error. Relative to the actual satellite-to-user range, the satellite-to-user range measured using carrier phase becomes too short; at the same time the code measurement will be too long, which is due to the advance in the carrier phase and delay in the PRN code, respectively El-Rabbany (2002).

Ionospheric scintillations are more pronounced at the equatorial region ($\pm 15°$) and auroral zones than in the mid-latitude region (Romano *et al.*, 2013). Generally, the ionospheric delay causes GPS navigation errors on the order of 5 to 15 m, but can reach over 150 m in severe cases (El-Rabbany, 2002). Dual-frequency GPS receivers are used to estimate the ionospheric delay by combining the L1 and L2 carrier-phase measurements (El-Rabbany, 2002; Misra and Enge, 2006). It is difficult to remove errors due to ionospheric scintillation because of the random spatial distribution of the rapidly varying irregularities along the propagation path (Carrano *et al.*, 2005).

2.9.2 Multipath effects on GPS accuracy

Multipath errors arise when receiving reflected or diffracted duplicates of the desired signal, which arrive at the receiver along different paths(Kaplan and Hegarty, 2006). Multipath errors are primarily caused by reflecting surfaces near the antenna and situated on the horizon and secondly from reflections at the satellite during transmission (Hofmann-Wellenhof *et al.*, 1992). Signals that get reflected by stationary objects follow a different path to get to the antenna. The reflected path will have a path length with longer propagation time than signals that use a direct path to the antenna. Interference of these reflected signals with the direct signal will contribute to the fluctuation on the received signal phase and amplitude (Mohinder *et al.*, 2001). Errors in the measured phase that are introduced by multipath effects are directly proportional to the difference of path length travelled by the direct and indirect sig-

nals from their origin to the receiver (Elósegui *et al.*, 1995; Hofmann-Wellenhof *et al.*, 1992). When a reflected signal arrives at the receiver in phase with the direct signal it will cause constructive interference which will increase the strength of the signal, while destructive interference occurs when they are out of phase, which causes signal fading (Misra and Enge, 2006). In a severe multipath effect, loss of lock may occur (Hofmann-Wellenhof *et al.*, 1992).

Multipath errors affect both the pseudorange and carrier-phase measurements. However, the pseudorange measurement is more strongly affected by multipath errors than carrier phase measurement (El-Rabbany, 2002; Misra and Enge, 2006). Multipath signals cause distortion in the correlation peak between the code generated by the receiver and received code, which can lead to a pseudorange measurement error of up to 150 m. The maximum error caused by multipath effects on carrier-phase measurement occurs when the multipath carrier phase is 90° relative to the direct path, producing a carrier phase error of 45° or a quarter of a cycle (about 4.8 cm at the L1 frequency) (El-Rabbany, 2002; Kaplan and Hegarty, 2006).

Signals reflected from nearby objects (as seen in Figure 2.11), or even grazing multipaths reflected from distant objects, can arrive with short delays (e.g., tens or hundreds of nanoseconds). This can affect the correlation function between the received composite (direct path plus multipath) signal and the locally generated reference in the receiver. Multipath signals will also affect the composite phase of the received signal, which is directly related to the variation in path length (Kaplan and Hegarty, 2006).

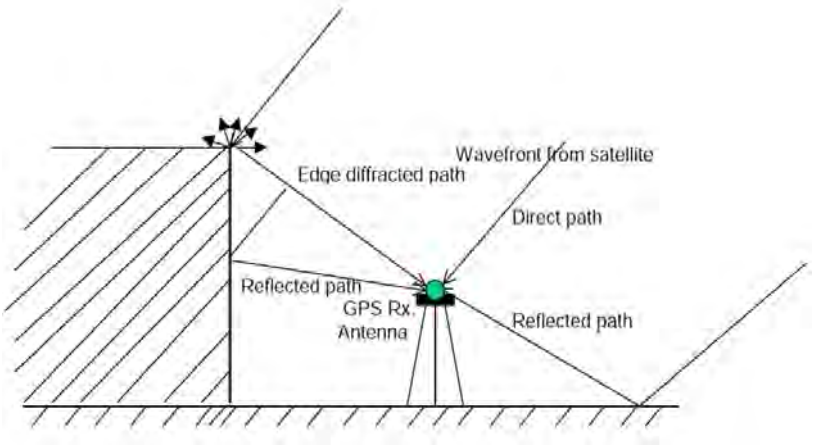

Figure 2.11: Multipath signals (credit: courtesy of Charles Carrano, Boston College).

The impact of multipath effects depends on the amplitude, phase and delay of the reflected signal relative to the direct signal and also on the rate of change of the phase (Misra and Enge, 2006). GPS receivers can distinguish between direct and indirect signals in the multipath environment if the relative delay of the reflected signal is longer than 1 microsecond for the C/A-code (where 1 microsecond is a typical width of a correlator used for differentiating direct and indirect signals). It is difficult to

differentiate multipath signals arriving within less than 1 microsecond after the direct signal is received (Kaplan and Hegarty, 2006; Misra and Enge, 2006).

Reducing multipath effects

Multipath effects can be reduced by choosing an antenna location where there are no stationary reflecting structures such as trees, mountains or buildings at an elevation above the internal elevation threshold of the antenna (Hofmann-Wellenhof *et al.*, 1992; Misra and Enge, 2006). Since the horizon is the main contributor to multipath effects, the reduction of multipath errors can be achieved by increasing the elevation cutoff angle for received signals, to typically 15° to 30° above the horizon. Another way to reduce multipath effects is by using antennas that can attenuate the reflected signals, such as choke ring antennas, wideband antennas and also by using antennas that take advantage of signal polarization. GPS signals are right-hand circularly polarized. Multipath signals which get reflected with an odd number of reflections are left-hand circularly polarized, but signals that reach the antenna after an even number of reflections become right-hand circularly polarized again (El-Rabbany, 2002; Hofmann-Wellenhof *et al.*, 1992; Misra and Enge, 2006). Using an antenna with a radio frequency absorbing ground plane can reduce multipath signals from low or even negative elevation angles.

Filtering out multipath errors using an outlier-analysis method that is based on the standard deviation of the Code-Carrier Divergence of scintillation data was done by Spogli *et al.* (2014), who showed that multipath errors can be reduced effectively using the new filtering method. Comparing it to using a fixed-elevation cutoff, their method limits the loss of non-multipath data.

Chapter 3

Instruments and data analysis

3.1 GPS Ionospheric Scintillation and TEC Monitoring

The device we used for GPS Ionospheric Scintillation and TEC Monitoring is a GPS Ionospheric Scintillation and TEC Monitor (GISTM) manufactured by Novatel (model GSV4004B). The GISTM is a dual-frequency receiver that can measure amplitude and phase scintillation at a 50-Hz rate at the GPS L1 frequency. GPS signals provide an excellent means to monitor ionospheric scintillation because they are continuously available and can be measured along many ray paths through the ionosphere simultaneously. The GISTM derives the amplitude scintillation index (S_4) from the 50-Hz amplitude measurements on L1 frequency, the phase scintillation index (σ_ϕ) from the 50-Hz carrier phase measurements, and the ionospheric TEC from a combination of pseudorange and carrier phase measurements at both the L1 and L2 frequencies. It also measures the code/carrier divergence at a rate of 1 Hz (Valley, 2005). The GISTM gives scintillation measurements with a better data rate than the International GPS Service (IGS) that has a sampling rate of 1-Hz (Prikryl *et al.*, 2013). The sampling rate of the GISTM (typical sampling rates of 10 - 50 Hz are used) is sufficient to resolve the temporal dynamics of ionospheric scintillation (Carrano and Groves, 2006).

Figure 3.1: Components of a GSV4004B GISTM receiver for the Hermanus station.

The Novatel GSV4004B GISTM receiver was developed by GPS Silicon Valley with support from NovAtel (Shanmugam *et al.*, 2012). It can track 10 to 11 GPS satellites and 1 to 3 SBAS (Satellite Base Augmentation System) Geo-stationary satellites. The GSV4004B consists of an L1/L2 GPS antenna, a GPS receiver and a power supply with various interconnecting cables. Picture of the Hermanus GISTM station is shown in Figure 3.1, including the GSV4004B GISTM receiver, the GPS antenna, a computer and several interconnecting cables.

The GISTM stations included in this project are located at Gough Island, Marion Island, Hermanus in South Africa, and the SANAE IV base in Antarctica (see Figure 3.3). Pictures of the antennas and the receiver are shown in Figure 3.2.

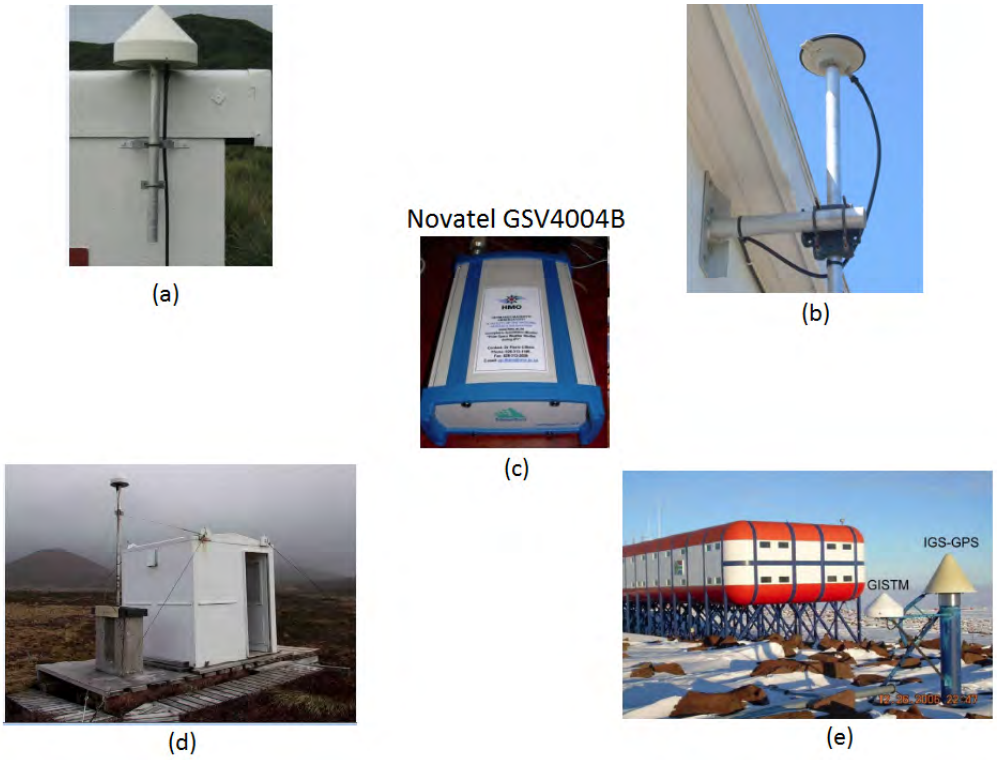

Figure 3.2: Pictures of GISTM antennas and the Novatel GSV4004B receiver. (a) Antenna on Gough Island (b) Antenna in Hermanus (c) Receiver (d) Antenna on Marion Island (e) Antenna at SANAE IV, Antarctica.

All GISTM stations require an internet connection to send the scintillation data once a day to the server at the SANSA Space Science centre in Hermanus. The data transmitted by each station to Hermanus daily has a total size of about 7.94 MB per-station. The scintillation data includes different files that contain the output data logged either in a binary or ASCII format. The data logging operation is controlled using software installed on a computer that is connected to each GISTM receiver. Two of the software programmes that can be used with GSV4004B receivers are SCINDA (Scintillation Network and Decision Aid) and SLOG. The SLOG software logs the output data in *.GPS and *.SLI files, and saves the daily scintillation data using a file name that is composed of the GPS week and GPS day of the week. In the GPS calendar, every week is identified with a specific number and each day of the week is represented using numbers from 0 (Sunday) to 6 (Saturday).

The SCINDA software provides measurements of S_4, σ_ϕ, TEC, and RTEC (Rate of TEC), as well as receiver position in real time. The real-time data processing reduces the man-hours and cost required to post-process large volumes of raw data. It is also possible to use stations with a low-bandwidth internet connection for ionospheric studies, since the processed data are smaller in size than the raw data (Carrano and Groves, 2006). The SCINDA software logs data in six different files: *.ism, *.psn, *.scn, *.msg, *.rng and *.nvd. The SCINDA software gives daily and/or hourly scin-

tillation data and saves the data using a file name derived from year, month and day. In the case of hourly data the file name includes hour, minute and second (e.g. daily file 150131.ism, hourly file 101201_010000.ism). The *.nvd file gives the raw data logged at the 50 Hz rate and the *.msg file contains diagnostic messages. The ionospheric statistics including S4, TEC_P, and TEC_ϕ data are logged in the *.scn file. The *.psn file gives the estimated position of the antenna in longitude, latitude and altitude every second (1 Hz) and the PRN number of the visible satellites.

3.2 Amplitude and phase scintillation measurements

The *.ism 1-minute parameter file, which we get from GISTM, contains a time stamp in GPS week and GPS time of the week, PRN number which is used as the identification of the satellite, Total Electron Content (TEC), RTEC and other signal parameters that can measure the quality of the signal. GPS week and time of week (in seconds) are used to record the time of measurement. Time of week (TOW) is reset to 0 every week at midnight on Saturday.

The output data provides TEC and ΔTEC (in TECu) computed over 15, 30, 45 and 60 seconds. The signal-to-noise ratio (SNR) is used to measure the quality of reception (Romano *et al.*, 2013). Lock time on L1 and L2 gives the record of how long the receiver has been locked to the carrier phase on the L1 and L2 frequencies. The difference between code and carrier pseudorange every second is averaged over 60 seconds and recorded as the average Code-Carrier Divergence (CCDIV). The CCDIV measures the difference between group delay and carrier phase advance. The CCSTDDEV is used to verify the existence of multipath effects, since the divergence due to ionospheric scintillation is not significant over a 60-second period (Datta-Barua *et al.*, 2003; Van Dierendonck *et al.*, 1993). A sample of the scintillation data contained in the *.ism files is shown in Table 3.1.

Table 3.1: An extract of data from an *.ism file that contains: GPS week, GPS Time of Week (TOW) in seconds, satellite PRN, Receiver status, azimuth angle and elevation angle (in degrees), Carrier-to-Noise density on L1, total S4 and correction to S4.

GPS week	TOW	PRN	RxStatus	Az	Elv	L1 CNo	S4	S4 Cor	...
1641	338460.00	22	00A00000	8.84	18.99	45.09	0.0919	0.0557	...
1641	338460.00	32	00A00000	240.59	40.37	49.69	0.0489	0.0327	...
.									
.									
.									

In order to remove the low-frequency background noise from the scintillation, both amplitude and phase scintillation measurements must be detrended (Shan-

mugam *et al.*, 2012). Raw phase measurements are detrended with a 6th-order Butterworth high-pass filter using a user-specified cutoff frequency. The detrending process removes all low-frequency effects below the cutoff frequency (Van Dierendonck *et al.*, 1993). The receiver logs five values of the phase scintillation index σ_ϕ every 60 seconds that are the residuals of the detrended phase measurements computed over periods of 1 second, 3 seconds, 10 seconds, 30 seconds and 60 seconds.

The raw S_4 amplitude scintillation index is detrended using a 6th-order low-pass filter with a user-specified cutoff frequency. There are two types of S_4 values that are logged in the *ism data: total S_4 and correction to the total S_4. The total S_4 includes the amplitude scintillation due to ambient noise. The amplitude scintillation that is due to ambient noise can be derived from the estimated average signal-to-noise density (S/No) over the entire evaluation interval (60 seconds) as follows (Van Dierendonck *et al.*, 1993):

$$S_{4_{No}} = \sqrt{\frac{100}{S/No}\left[1 + \frac{500}{19S/No}\right]}. \tag{3.1}$$

Scintillations that are due to ambient noise can be removed from the total S_4 by subtracting the square of S_4 due to the ambient noise in equation Equation 3.1 from the square of the total $S_{4_{tot}} = \sqrt{\frac{<SI^2>-<SI>^2}{<SI>^2}}$, where SI is the signal intensity and $<>$ represents the average value over an interval of 60 second (Datta-Barua *et al.*, 2003; Van Dierendonck *et al.*, 1993). This gives us an S_4 index that is free of ambient noise.

$$\begin{aligned} S_4 &= \sqrt{S_{4_{tot}}^2 - S_{4_{No}}^2}, \\ &= \sqrt{\frac{< SI^2 > - < SI >^2}{< SI >^2} - \frac{100}{S/No}\left[1 + \frac{500}{19S/No}\right]}. \end{aligned} \tag{3.2}$$

In cases where the $S_{4_{No}}$ is greater than the total S_4, which is the case where there is no scintillation, we have to set S_4 to zero in order to remove the ambient noise.

3.3 Methods used to analyse scintillation data

The multipath environment characterisation was done by taking daily data for one year from each station. The locations of the stations are shown in Figure 3.3. The GISTM stations were installed by SANSA during the international polar year, 2007-2009, to investigate the impact of particle precipitation on ionospheric scintillation in the vicinity of the South Atlantic Magnetic Anomaly (SAMA). For the Gough Island

and Marion Island stations, we used data for the period May 2009 to April 2010. Hermanus data was taken from July 2009 to June 2010 and SANAE IV data were taken for the calendar year 2010.

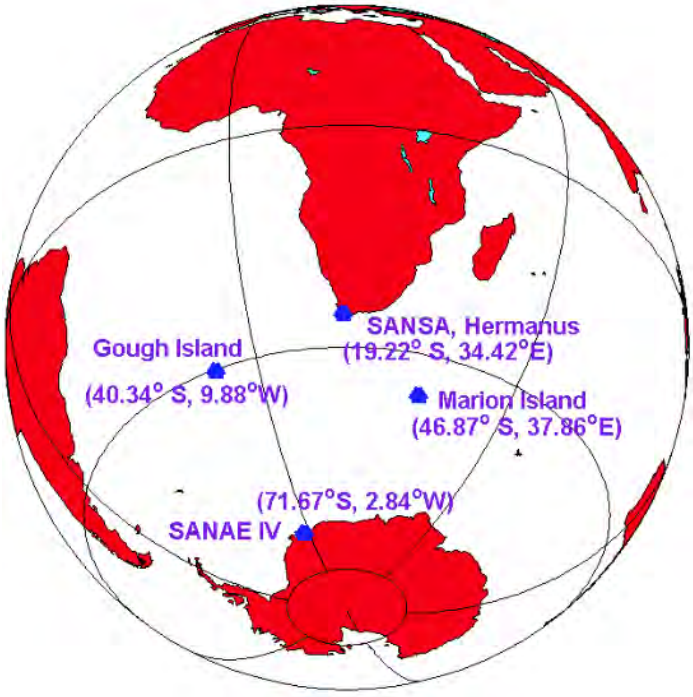

Figure 3.3: Geographic locations of Gough Island, Hermanus, Marion Island and SANAE IV.

Figure 3.4 shows the ray paths of GPS satellites plotted over one month on an elevation-azimuth map as observed from each of the GISTM stations. Because of the 55° inclination angle of GPS satellites, there are no visible satellites in the south direction (South corresponds to 180° azimuth angle) as indicated by the red hatched areas on the figures, for Gough Island, Hermanus and Marion Island. The minimum elevation angle of satellite visibility depends on the horizon of the station. The minimum elevation profile of each site is depicted by the blank areas below the visibility curves. The receiver at Hermanus had a built-in cutoff angle of 10°. Marion Island had a lower cutoff angle around 5° in all directions. In the case of Gough Island the elevation angle of the horizon reaches up to 20° at around 300° azimuth, which corresponds to the Northwest of the receiver, as shown in Figure 3.4(a). The receiver at SANAE IV had a built-in elevation cutoff angle of either 5° or 10° during the period selected for this study.

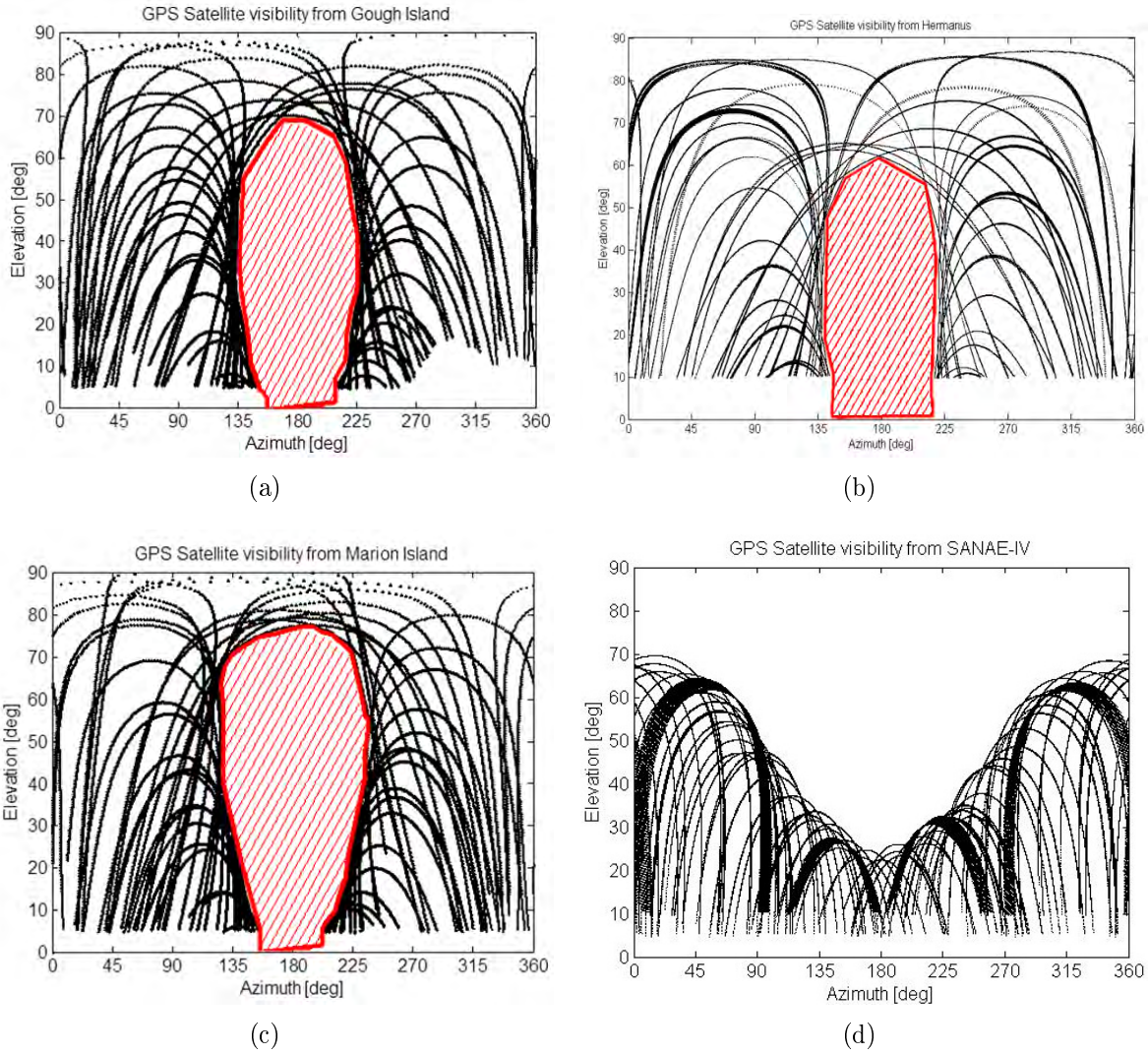

Figure 3.4: GPS satellite visibility over one month as seen from (a) Gough Island (b) Hermanus (c) Marion Island (d) SANAE IV GISTM receiver antennas.

A MATLAB script was used to read the ISM file, apply some thresholds and extract the necessary parameters and save them as a TXT file. The S_4 and σ_ϕ values less than 0.02 and greater than 1 were suppressed. Only signals from satellites with PRN numbers between 1 and 32 (GPS satellites) were included in this analysis, thus excluding the signals from geostationary satellites which are associated with PRN 128 to 132. The GSV4004B GISTM does not detect signals from other GNSS satellites, such as GLONASS and GALILEO. Since the purpose of this project was to study the multipath signals, including signals that are scattered from the horizon, we took the elevation angle threshold to be zero even if the minimum built-in elevation angle for GPS satellite visibility for the selected stations were usually set at 5° by the hardware.

The Ground-Based Scintillation Climatology (GBSC) method developed by Spogli *et al.* (2009) was used by Romano *et al.* (2013) to show that averaging the spatial

distribution of the scintillation over a period is a promising technique to characterize environmental effects on a station and to develop a mitigation method to correct for multipath effects (Spogli *et al.*, 2014). The method used to characterize the multipath environment is basically an azimuth-elevation map of scintillation indices and other signal quality parameters averaged over a long period. The method used in this research comprised plotting the occurrence percentage of amplitude and phase scintillation indices on an azimuth-elevation map and also plotting average scintillation indices and other signal quality parameters over a period of time on an azimuth-elevation map. Each bin on the map corresponds to 1° elevation by 1° azimuth. The amplitude scintillation index (S_4) was plotted on the azimuth-elevation map in two ways. The first method showed the percentage of occurrence of S_4 values greater than the threshold value taken to characterize the multipath effect. The second method showed the average value of S_4 values greater than the threshold value over one year calculated for each 1° by 1° bin. The same plots were also produced for the other indices σ_ϕ, L1 CNo and CCSTDDEV.

From these plots we were able to establish the areas of high scintillation, in azimuth-elevation space, related to multipath errors. The MATLAB spline curve fitting tool was used to fit a curve to the areas that have high scintillations. Typical examples of an azimuth-elevation map of S_4 occurrence percentage and S_4 mean and also the curve fitted to the areas that have high scintillations are shown in Figure 3.5. An azimuth-dependent elevation threshold, derived from the curve fitted to areas with high scintillation, can be used to filter out high scintillation occurrence that is related to multipath errors.

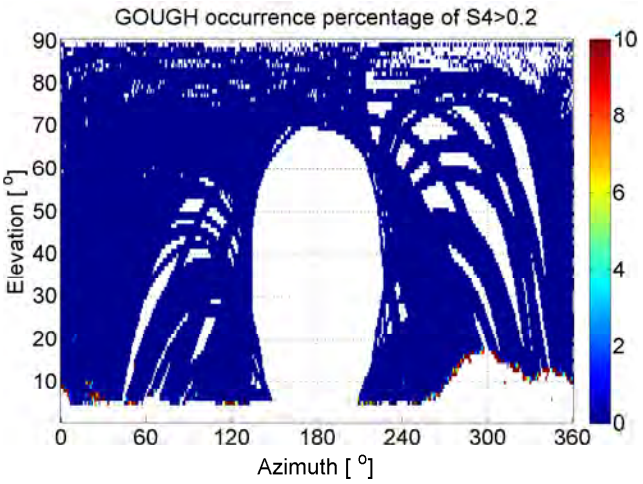

(a) Occurrence percentage of $S_4 > 0.2$ per each azimuth-elevation bin over one year.

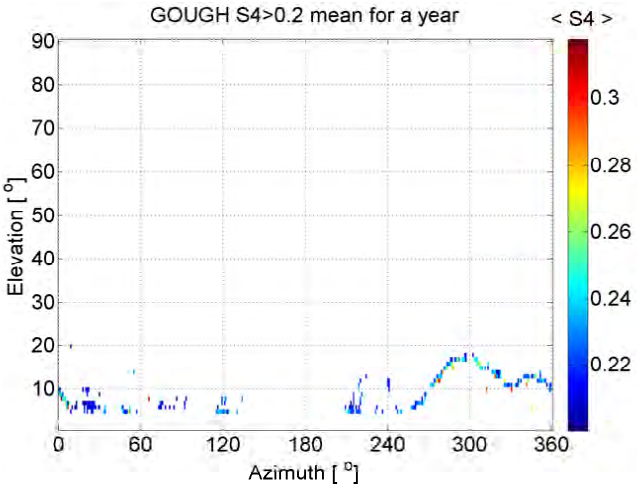

(b) Mean of $S_4 > 0.2$ per each azimuth-elevation bin for one year data.

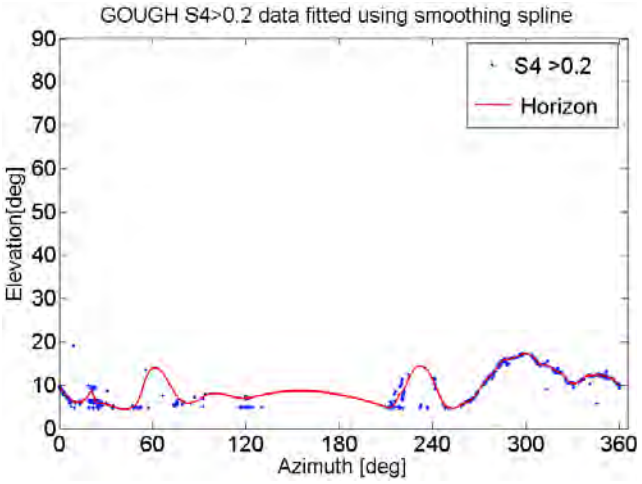

(c) Curve fitted to the areas with $S_4 > 0.2$ values.

Figure 3.5: Azimuth-elevation maps of (a) S_4 occurrence percentage (b) S_4 mean for one year data (from May 2009 to April 2010) and (c) a curve fitted to the areas with $S_4 > 0.2$ for the Gough Island GISTM.

Chapter 4

Results and discussion

This chapter presents some of the results found from the scintillation data analysis done for Gough Island, Hermanus, Marion Island and SANAE IV. Results shown in this chapter include the scintillation of GPS signals, during both quiet and geomagnetically disturbed days, for both high-latitude (SANAE IV) and mid-latitude (Hermanus). These results will show the effect of the ionospheric scintillation and multipath effects of the surrounding environment on: the S_4 index, the σ_ϕ index, the Standard deviation of the Code-Carrier divergence and the Carrier-to-noise ratio of L1. The results also show the GPS positioning errors that can be caused by scintillation effects. Then we will show the characterization of the spatial distribution of scintillation to identify areas in azimuth-elevation space that are affected by multipath errors. For each station, a station-specific azimuth dependent elevation threshold is derived to filter out multipath signals.

4.1 GPS signal scintillation during quiet and geomagneticaly disturbed days

Severe space weather conditions can lead to geomagnetic storms, which can cause scintillations that affect the quality of GPS signals. Geomagnetically disturbed days are characterized using the geomagnetic K-index and Dst index, and also from disturbance of the Earth's magnetic field components ΔX, ΔY and ΔZ measured using magnetometers. Week geomagnetic storm conditions are characterized with a min-

imum Dst values between -30 nT and -50 nT and Kp $\leq$ 4. Strong to great storm conditions are characterized with minimum Dst value of less than -100 nT and Kp $\geq$ 7 (Loewe and Prölss, 1997).

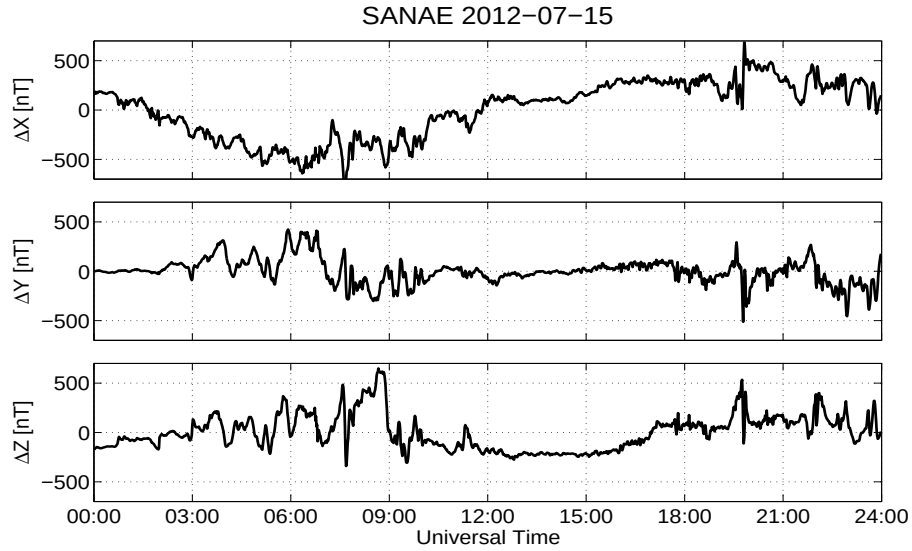

(a)

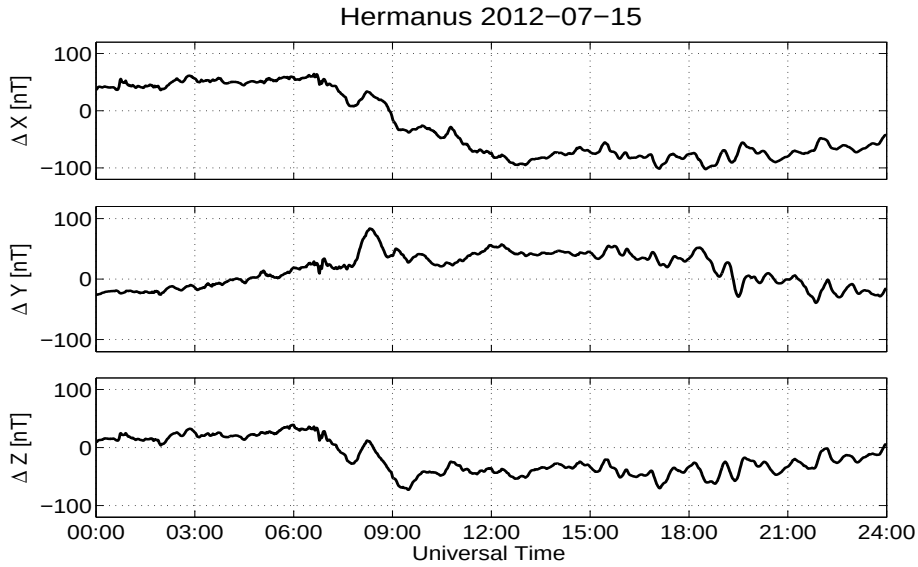

(b)

Figure 4.1: Magnetic field variations due to a geomagnetic storm observed at (a) SANAE IV and (b) Hermanus : ΔX (top panel), ΔY (middle panel) and ΔZ (bottom panel) observed on 2012-07-15.

Figure 4.1 shows the magnetic field variations derived from magnetometer measurements at SANAE IV and Hermanus. The geomagnetic storm on 2012-07-15

was characterized by a maximum interplanetary K-index value of 6 (SpaceWeatherlive.com, 2015) and minimum Dst value of -127 nT (KYOTO, 2015) (see Figure 4.2).

Based on the magnetic field fluctuations, the Kp-index and the Dst index values observed in Figures 4.1 and 4.2 show that it was a day with moderate storm activity (based on the NOAA space weather scale of geomagnetic storms http://www.swpc.noaa.gov/noaa-scales-explanation). Spaceweatherlive.com reported the storm condition for this day as "major to severe storms at high latitudes and minor to major storms at mid latitudes" (SpaceWeatherlive.com, 2015).

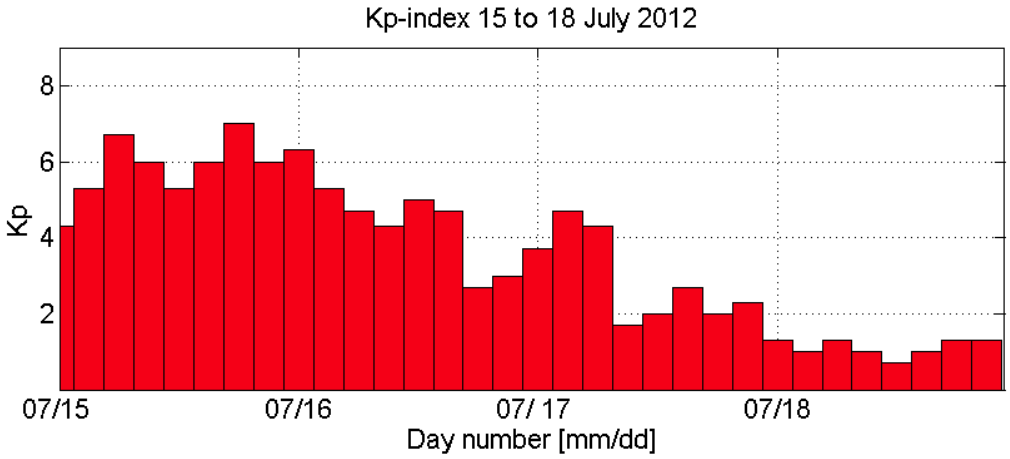

(a)

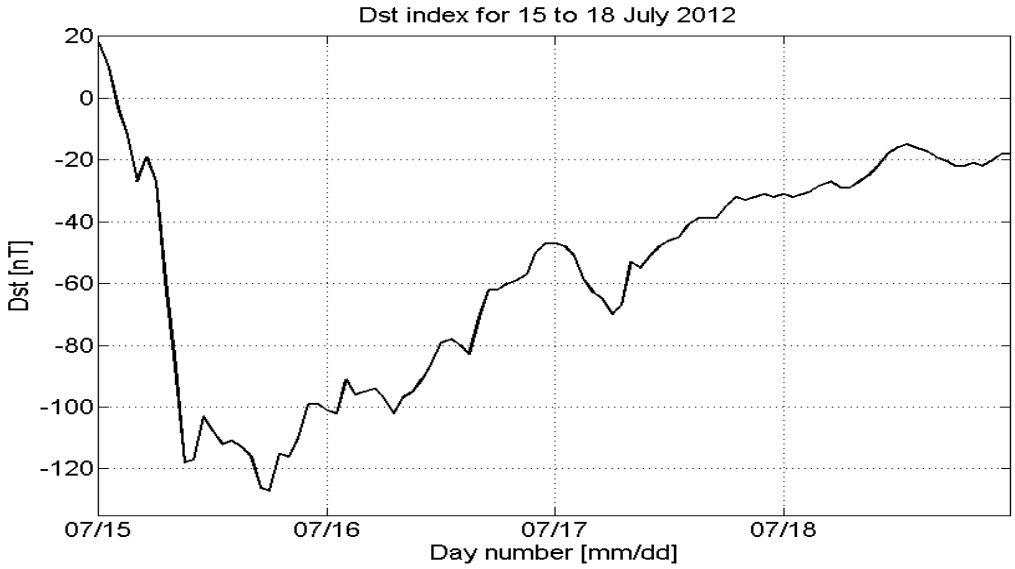

(b)

Figure 4.2: (a) Kp-index (b) Dst index for 15 to 18 July, 2012.

Figure 4.3 shows the amplitude and phase scintillations along the ray paths of all

satellites observed on 2012-07-15 from the SANAE IV GISTM station. The GISTM receiver located at SANAE IV measured high phase scintillation along the ray paths from most of the satellites observed above 20° elevation on 2012-07-15, as shown in Figure 4.3(b). A 20° elevation cutoff is used to remove scintillations that are due to the multipath effect of the horizon. Only a few of the ray paths experienced high amplitude scintillation (see Figure 4.3(a)). The scintillation effect caused by the storm was not strong on the signal amplitude while it severely affected the phase of the signals. Figures 4.4 and 4.5 show the amplitude and phase scintillation along the ray paths of each of the satellites observed from SANAE IV on 2012-07-15 together with the elevation of the satellites. We can see that the amplitude scintillation values increase as the satellite goes to lower elevation angles for all satellites in Figure 4.4(a) because of the multipath effect of the physical environment near the horizon. Since this particular day is a storm day, high phase scintillations were also observed at higher elevation angles (e.g. for PRN 22, 26 and 31 in Figure 4.4(b)) due to the ionospheric irregularities enhanced by the geomagnetic disturbance (see section 2.9.1).

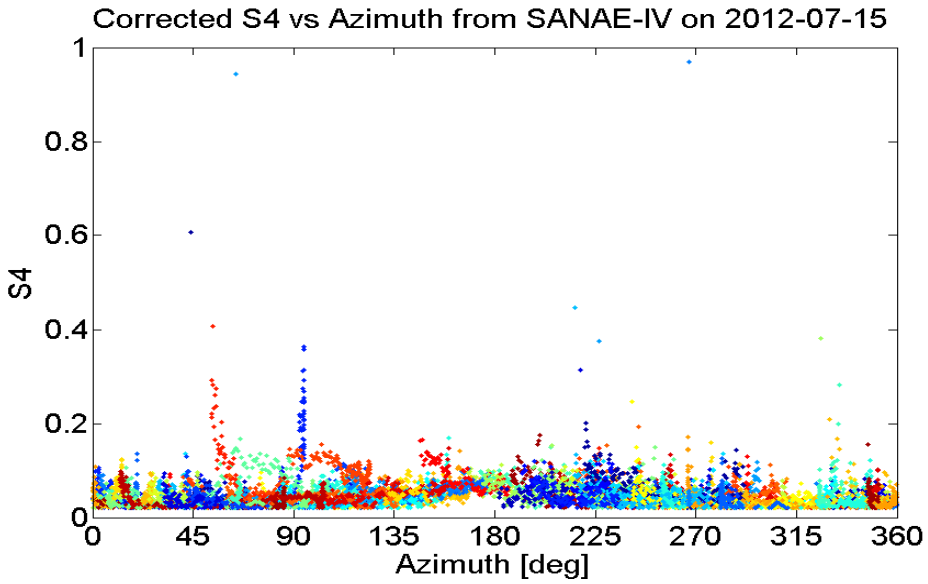

(a) Amplitude scintillation vs. azimuth angle for all satellites above 20° elevation angle which were tracked by the SANAE IV GISTM receiver on 2012-07-15.

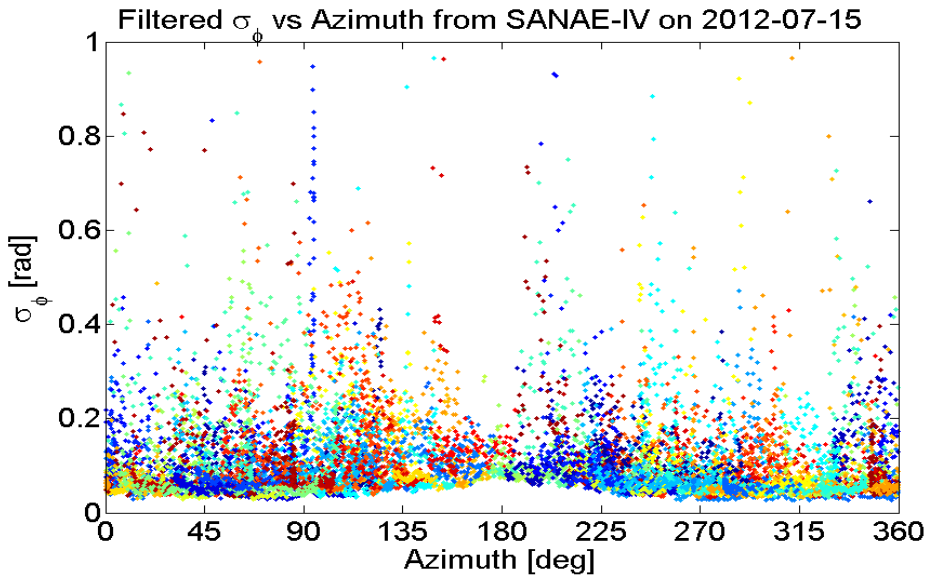

(b) Phase scintillation vs. azimuth angle for all satellites above 20° elevation angle which were tracked by the SANAE IV GISTM receiver on 2012-07-15.

Figure 4.3: Amplitude and phase scintillation for all satellites observed on 2012-07-15 from the SANAE IV GISTM antenna.

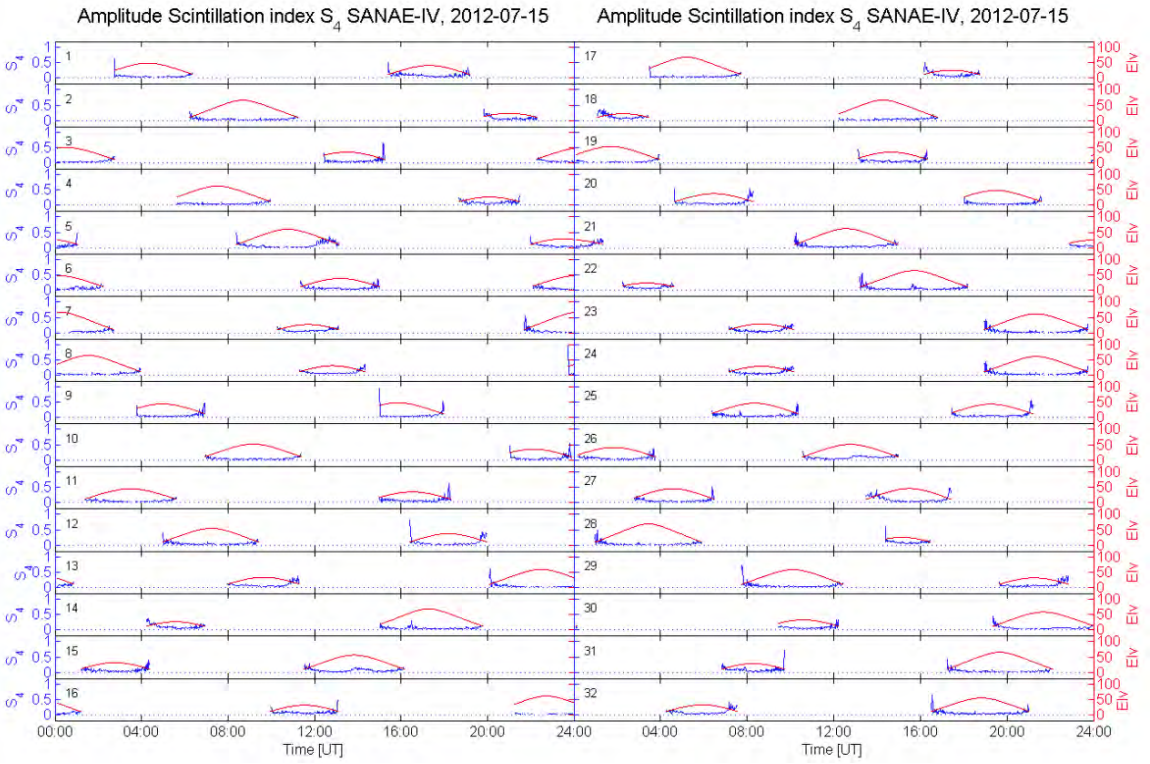

(a)

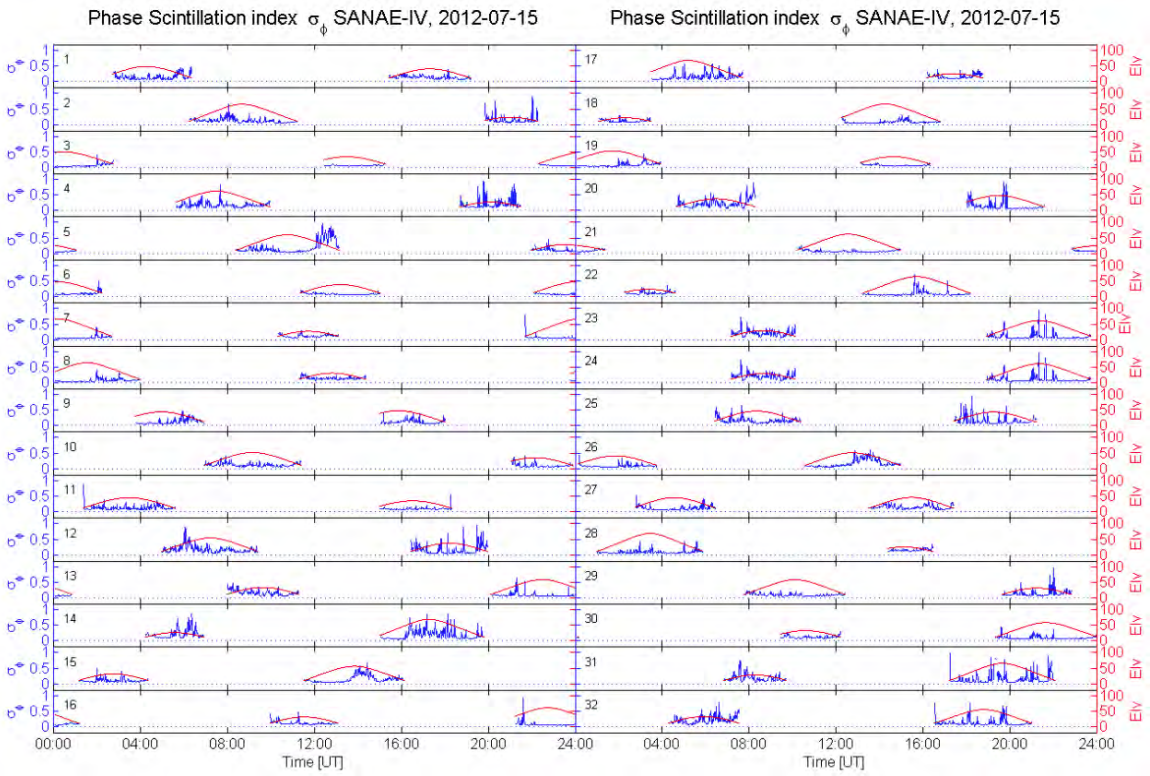

(b)

Figure 4.4: (a) Amplitude scintillation occurrence (in blue) and elevation angle (in red) (b) phase scintillation occurrence (in blue) and elevation angle (in red) for all satellites observed on 2012-07-15 from the SANAE IV GISTM station. The GPS satellite PRN numbers are indicated in the top left corner of each panel.

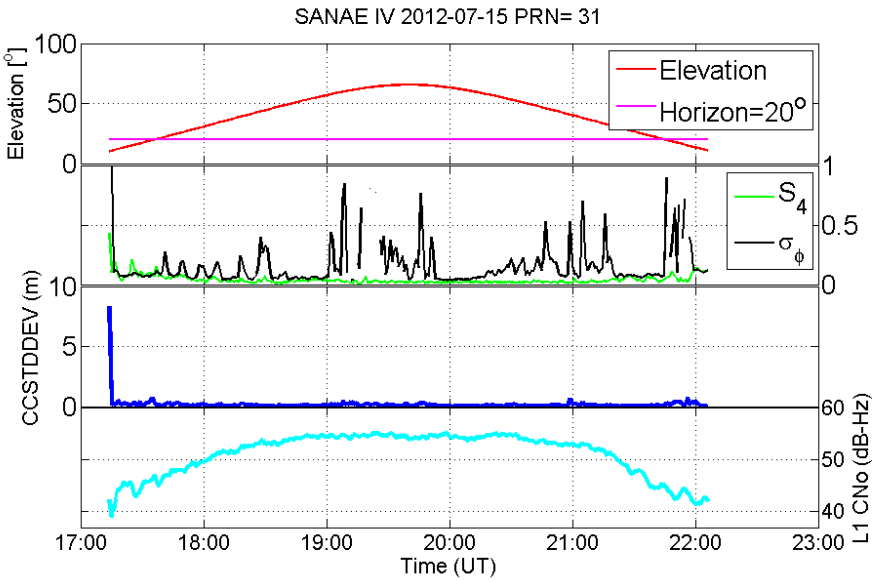

Figure 4.5: Various parameters related to scintillations observed on the ray path from PRN number 31 to the SANAE IV GISTM receiver: (1^{st} panel): elevation angle, (2^{nd} panel): amplitude scintillation index S_4 (green) and phase scintillation index σ_ϕ (black), (3^{rd} panel): standard deviation of the code-carrier divergence CCSTDDEV and (4^{th} panel): L1 carrier-to-noise ratio L1 CNo.

In order to study the scintillation effect on a particular satellite we choose PRN number 31, which exhibited scintillations both at high and low elevation angles. Figure 4.5 shows the path of the satellite as a function of elevation angle and time and also the S_4, σ_ϕ, CCSTDDEV and the carrier-to-noise ratio on L1 (L1 CNo) recorded for this particular satellite. High scintillations occur both at higher elevation and at lower elevation angles due to the ionospheric scintillation and the multipath scintillation, respectively. At low elevation angles, where the multipath effect is severe and the S_4 and σ_ϕ values are high, the CCSTDDEV is also high. The L1 CNo values in Figure 4.5 show that the signal quality fluctuates at low elevation angles because of the multipath effect of the horizon.

Figure 4.6 shows the scintillation indices S_4 and σ_ϕ as observed from the Hermanus GISTM station on 2012-07-15 for all the satellites above the 20° elevation cutoff. We used the 20° elevation cutoff angle to remove scintillations that are due to the multipath effect of the horizon, so that we can be able to see the scintillation effect that is caused mainly by the ionosphere. The S_4 values plotted in Figure 4.6(a) reach 0.2 and above while the σ_ϕ index values shown in Figure 4.6(b) are less than 0.1 radian. Comparing the scintillation observed at SANAE IV (see Figure 4.4) with the scintillation observed at Hermanus on the same day, the scintillation observed at Hermanus was not as severe as the scintillation observed at the SANAE IV station, which is expected since the storm was more intense at high latitudes.

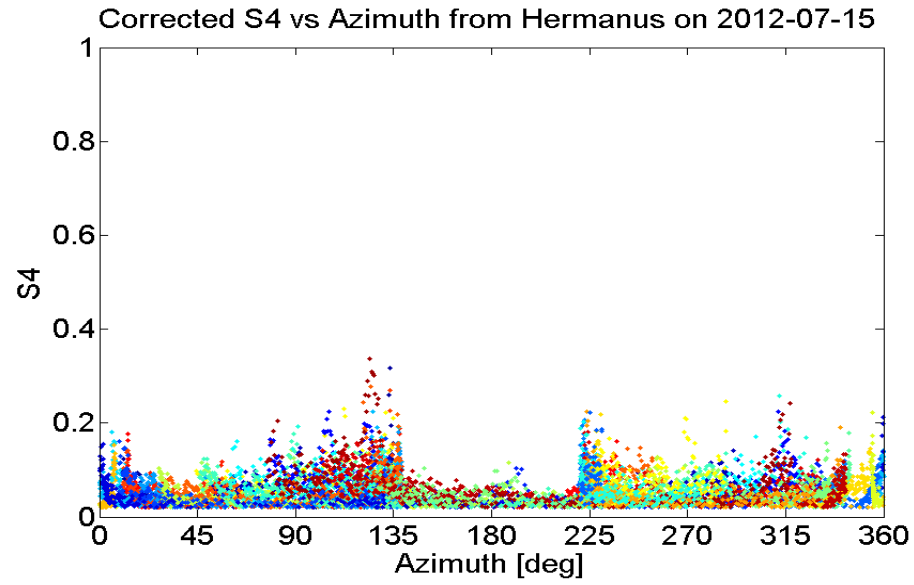

(a)

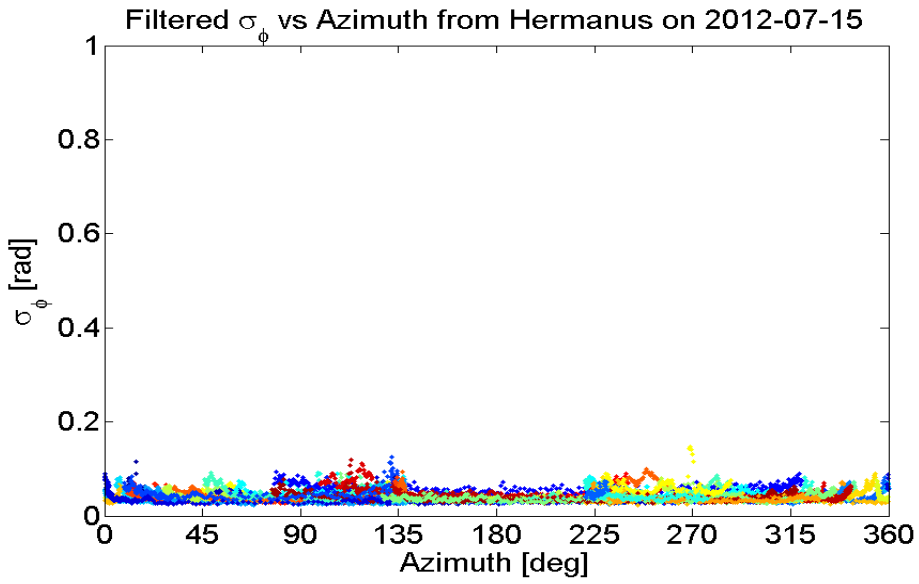

(b)

Figure 4.6: (a) Amplitude scintillation and (b) Phase scintillation (in radians) vs. azimuth angle (in degrees) for all satellites observed above a 20° elevation angle on 2012-07-15 from the Hermanus GISTM station.

Figure 4.7 shows the elevation, S_4 and σ_ϕ indices for all of the satellites observed from Hermanus on 2012-07-15. Except for the few high-amplitude scintillations observed at higher elevation angles (e.g. PRN 31 in Figure 4.7(a)) most of the scintillations are observed at lower elevation angles. The higher scintillations observed at low elevation angles are primarily due to the multipath effect of the horizon.

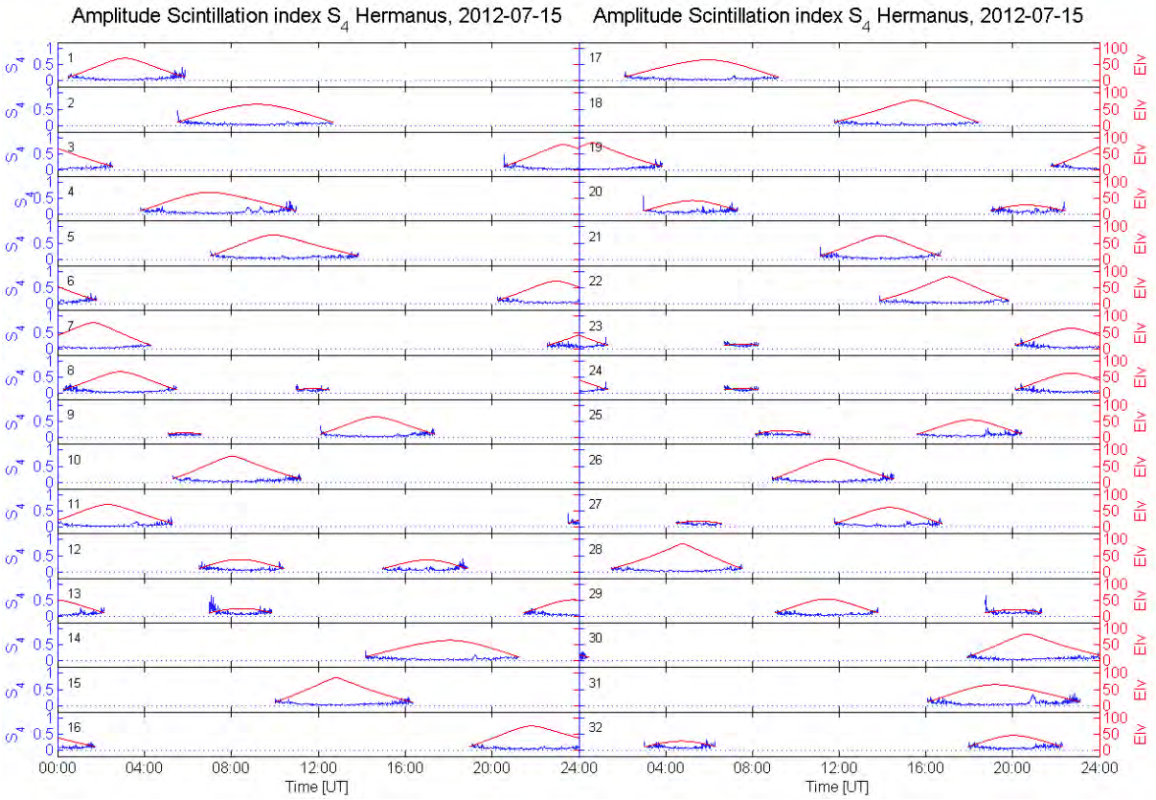

(a)

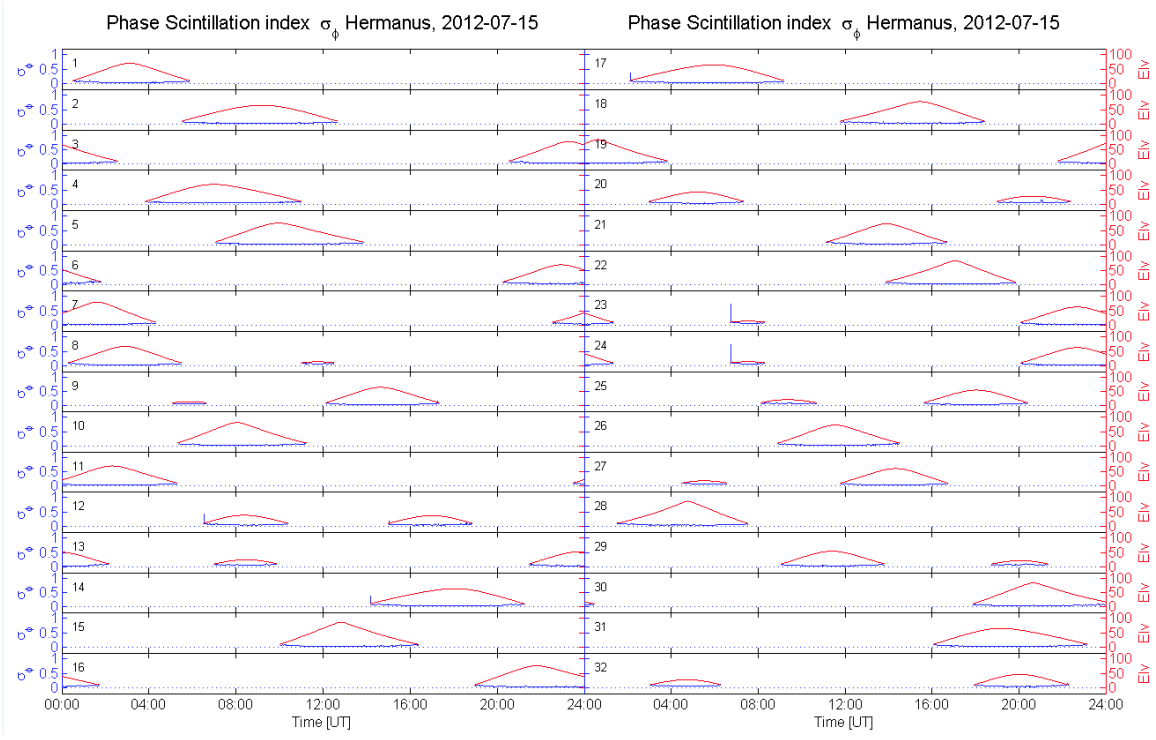

(b)

Figure 4.7: (a) Amplitude scintillation occurrence (in blue) and elevation angle (in red) (b) phase scintillation occurrence (in blue) and elevation angle (in red) for all satellites observed on 2012-07-15 from the Hermanus GISTM station.

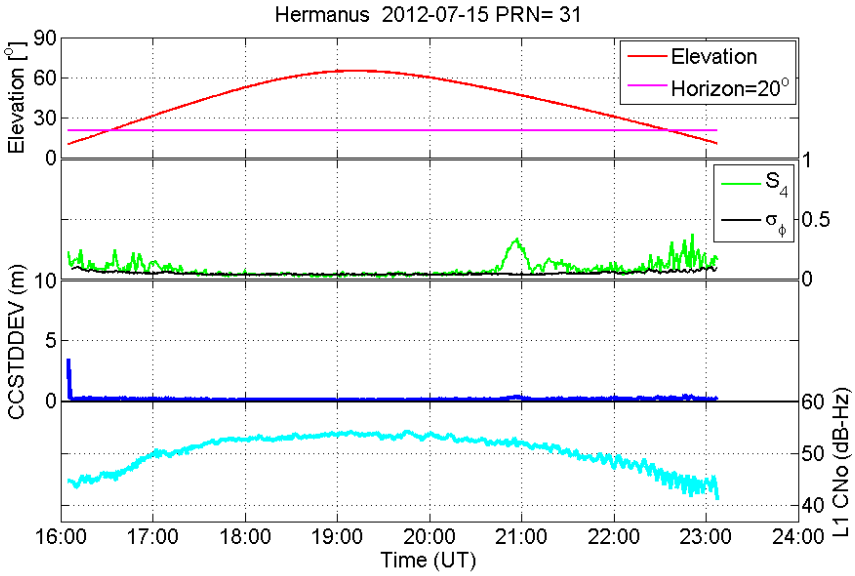

Figure 4.8: Various parameters related to scintillations observed on the ray path from PRN number 31 to the Hermanus GISTM receiver: (1^{st} panel): elevation angle, (2^{nd} panel): S_4 (green) and σ_ϕ (black) index, (3^{rd} panel): CCSTDDEV and (4^{th} panel): L1 CNo.

Figure 4.8 shows the elevation angle, S_4 index, σ_ϕ index, Standard Deviation of Code-Carrier Divergence (CCSTDDEV) and carrier-to-noise ratio on L1 (L1 CNo) for the satellite with PRN 31 on 2012-07-15. The amplitude scintillation and CCSTDDEV shows high values as the satellite goes to lower elevation angles and carrier-to-noise ratio starts to decrease at lower elevation (mostly below the 20° elevation angle), which is an indication of signal degradation due to the multipath effect. At around 50° elevation angle a higher value of S_4 is recorded which is due to the ionospheric scintillation effect, however the low σ_ϕ index shows neither ionospheric scintillation nor multipath effects.

4.2 GPS positioning errors

GPS position estimation accuracy is affected by different error sources; one of them is multipath effects. The multipath effect of stationary physical structures and ionospheric irregularities causes scintillation that can lead to cycle slip and loss of lock which can reduce the number of satellites available for position estimation. Figure 4.9 shows the horizontal position estimation errors for a storm day (2012-07-15) and a quiet day (2012-07-26) at the SANAE IV GISTM station. Each panel in Figure 4.9 illustrates the number of visible satellites available to compute the position, and also the amplitude and phase scintillations observed during these two days. For these plots no removal of multipath errors were done so that the effect of scintillations on position errors could be clearly demonstrated. The position and number of visible satellites are taken from the *.psn file, while the S_4 index and σ_ϕ index are taken from the *.ISM file. The horizontal position error is calculated from the longitudinal and latitudinal position estimation of the antenna measured at 1-second intervals. Since the *.ISM file measurements are taken every 60 s, we took the number of visible satellites and the position estimation error values at every 1 minute interval. The maximum values of S_4 and σ_ϕ are taken for each visible satellite at the 1 minute interval, (a GISTM receiver can track 10 to 11 satellites at any time).

Figure 4.9(a) shows that there are times when the number of visible satellites used for position estimation goes down to only four satellites, which leads to a high horizontal position error of up to 400 m. As this specific day is a storm day (maximum Kp-index of 7 (SpaceWeatherlive.com, 2015) and minimum Dst value of -127 nT (KYOTO, 2015), see Figure 4.2), significantly higher values of the σ_ϕ index were observed than for the quiet day depicted in Figure 4.9(b). At high latitudes during a storm day phase scintillations are manifested because of irregular patches of enhanced electron density. Higher values of the σ_ϕ index are observed for the storm day than on the quiet day. The S_4 patterns were similar on the two days, and most of the peaks in S_4 occurred at the same times on the two days, which confirms that the amplitude scintillation is mostly caused by the multipath effect of the physical structures in the vicinity of the antenna (see Figure 4.9(a)). It was also observed that some of the high position estimation errors that are due to the decrease in the number of visible satellites, correspond to high scintillation values, especially high S_4 values. It is known that strong and long duration scintillations can lead to loss of lock which results in a decrease in the number of satellites that will be available for the position estimation.

Figure 4.9(b) shows the horizontal position estimation error with a 1-minute interval and the number of visible satellites used to compute the position, and also the corresponding S_4 and σ_ϕ indices for a geomagnetically quiet day. For this day, 2012-07-26, a maximum Kp-index of 2 (SpaceWeatherlive.com, 2015) and a minimum Dst value of -1 nT (KYOTO, 2015) were recorded. As seen in Figure 4.9(b) there were a few times where the number of visible satellites decreased to four, leading

to high horizontal position errors. For the geomagnetically quiet day, there was an anomalous maximum horizontal position error of about 650 m observed at around 05:30 Universal Time (UT).

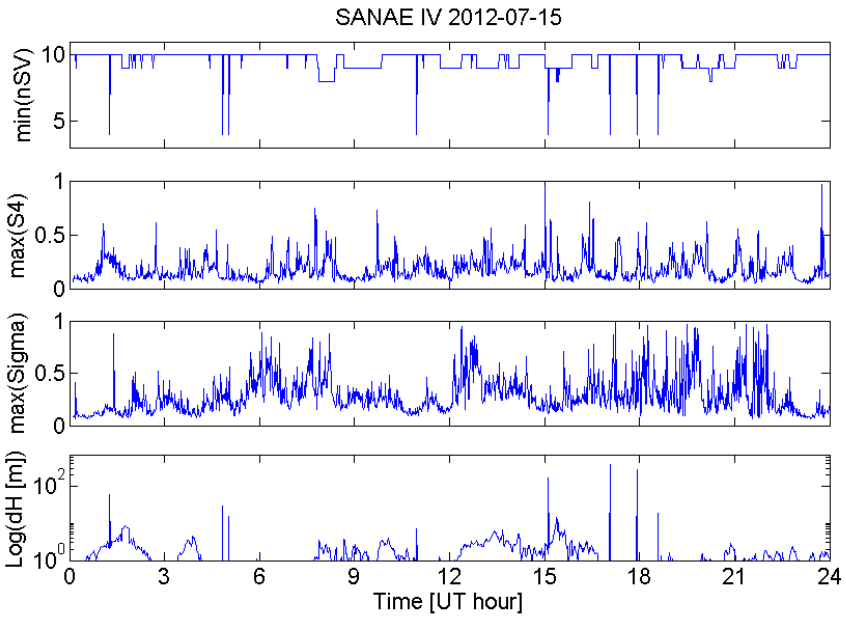

(a)

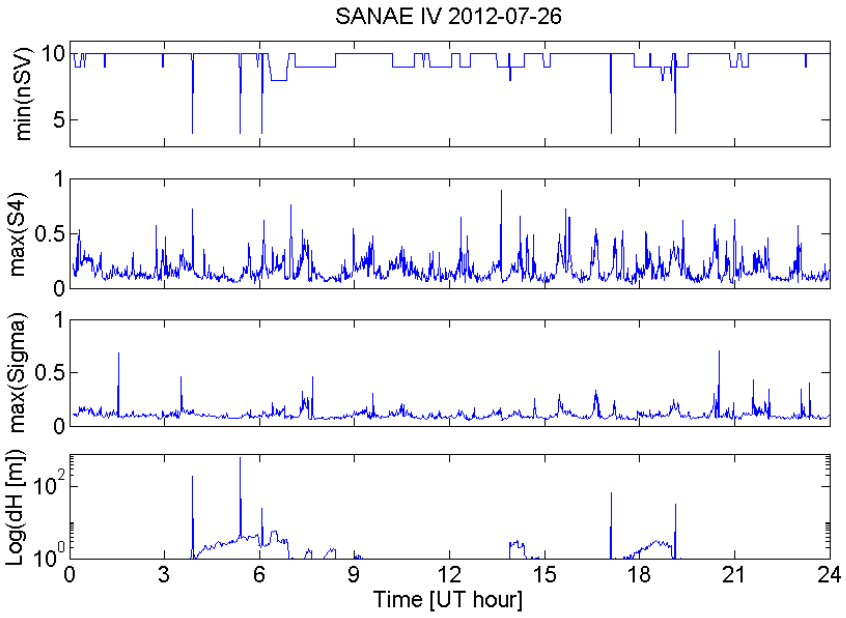

(b)

Figure 4.9: Number of visible satellites (1^{st} panel), S_4 (2^{nd} panel), σ_ϕ (3^{rd} panel), horizontal position estimation error (4^{th} panel) for (a) a geomagnetically disturbed day (2012-07-15) and (b) a geomagnetically quiet day (2012-07-26) at SANAE IV.

Figure 4.10 shows the distribution of the horizontal position estimation errors in the range between 0.5 m to 10.5 m for the 15^{th} and 26^{th} of July 2012. The position estimation error observed for both days shows a distribution with high error occurrence for small position errors around, 1 m, and a decrease in the occurrence of larger position errors (see Figures 4.10(a) and 4.10(b)). Figure 4.10(b) shows the distribution of the horizontal error for the geomagnetically quiet day (2012-07-26). We can see that the occurrence of large position errors is less frequent than on the storm day in Figure 4.10(a).

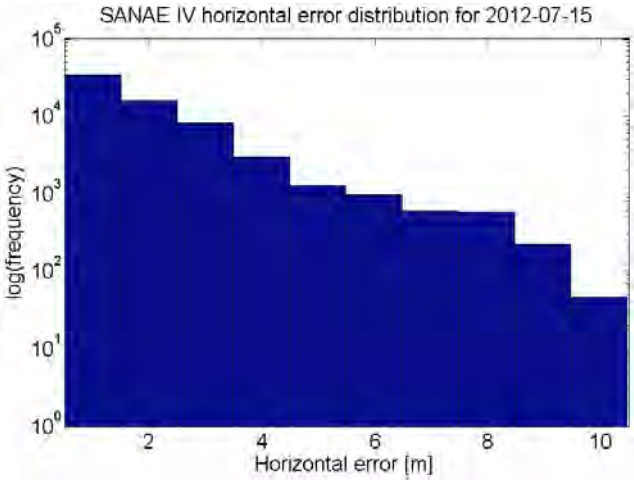

(a) Histogram of the horizontal position estimation error distribution in log scale during a high scintillation day because of the storm on 2012-07-15.

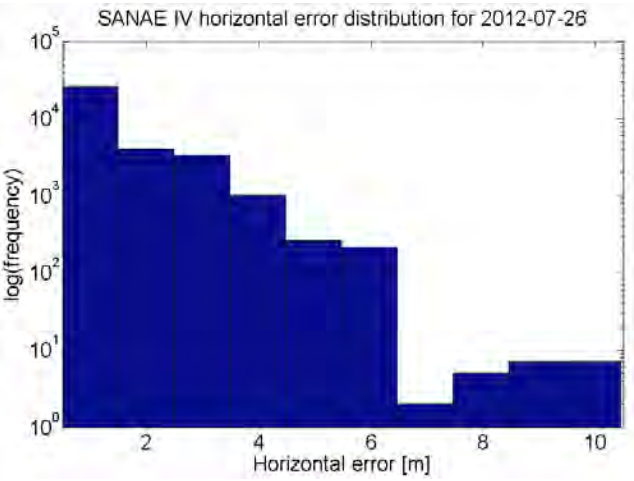

(b) Histogram of the horizontal position estimation error distribution in log scale showing a relatively lower scintillation occurrence for the geomagnetically quiet day (2012-07-26).

Figure 4.10: Comparing GPS position estimation errors for (a) geomagnetically disturbed and (b) quiet days at SANAE IV.

Figure 4.11 shows the correlation of the position estimation error with both the S_4 index and σ_ϕ index. It can be seen from the scatter plots shown in Figure 4.11, that there is a poor correlation between the scintillation indices (σ_ϕ and S_4) and the estimated position error.

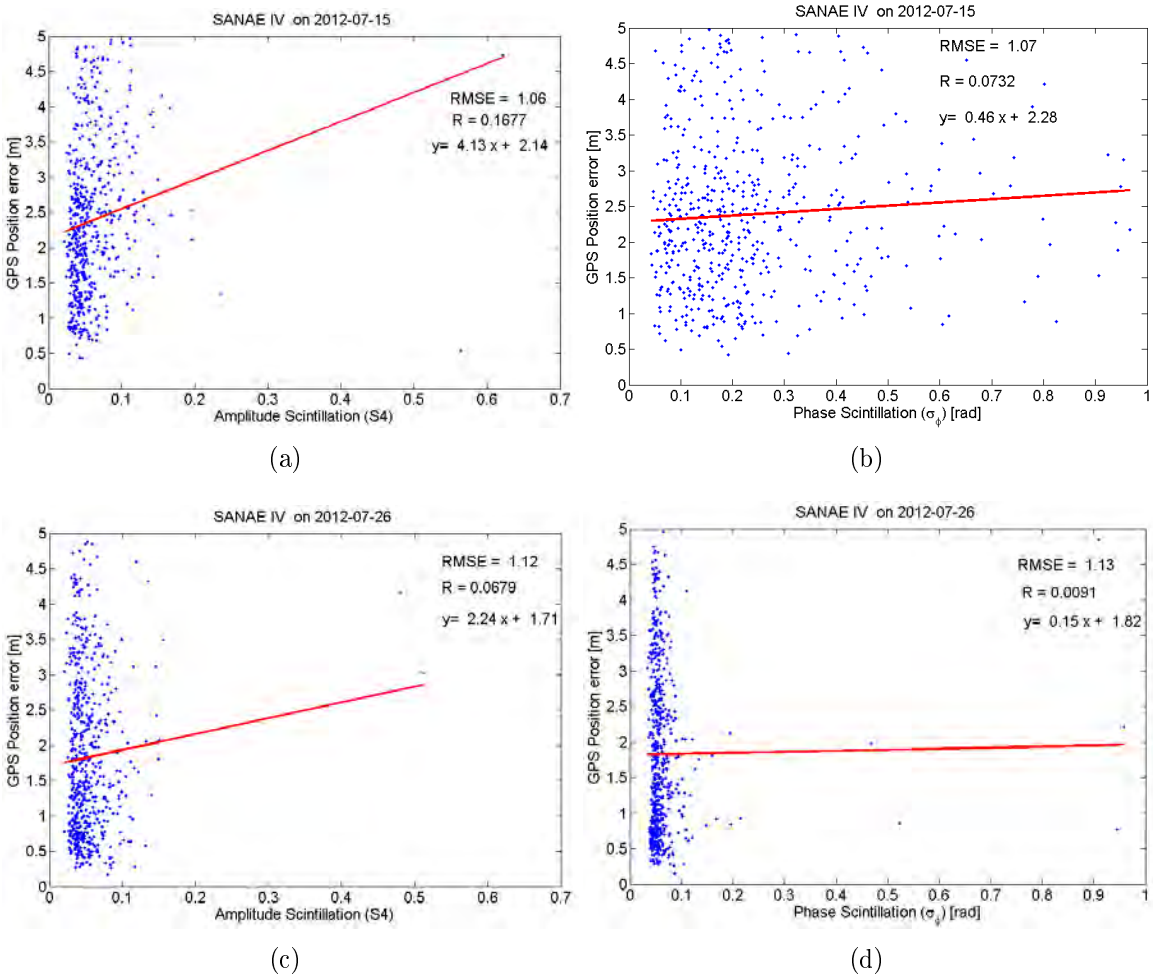

Figure 4.11: Scatter plot of GPS position estimation error vs (a) & (c) the amplitude scintillation (S_4) index, (b) & (d) the phase scintillation (σ_ϕ) index and the best linear fit both for geomagnetically disturbed and quiet days, 15 and 26 of July 2012, respectively. The correlation coefficient R is low for each case.

4.3 Gough GISTM receiver

In this section we will discuss some of the results we found from the scintillation data analysis done for Gough Island. For this analysis one year of scintillation data with 97% of the data available during May 2009 to April 2010 was used. Each 1° by 1° azimuth-elevation bin on the map contains scintillation index values of which the corresponding ray paths fall between the elevation and azimuth range of the specific bin. For each bin the S_4 data was averaged over one year.

Figure 4.12 shows azimuth-elevation maps for the S_4 index, σ_ϕ index, CCSTD-DEV and L1 CNo over one year. Figure 4.12(a) shows the percentage of occurrence of $S_4 > 0.2$ with a scale limit of 10%. In this case $S_4 > 0.2$ is considered as an indicator of strong scintillations. Therefore, areas with high occurrence percentage of $S_4 > 0.2$ throughout the year are identified as areas where stationary objects are regularly refracting and reflecting GPS signals. These signals reach the receiver with a different path length and within a short time delay from the direct signal which will introduce a random fluctuation on the amplitude and phase measurement.

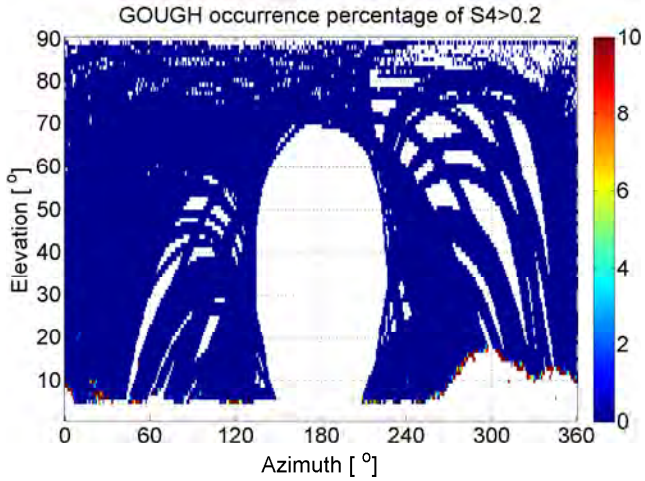

(a) Percentage occurrence of $S_4 > 0.2$ per azimuth-elevation bin over one year.

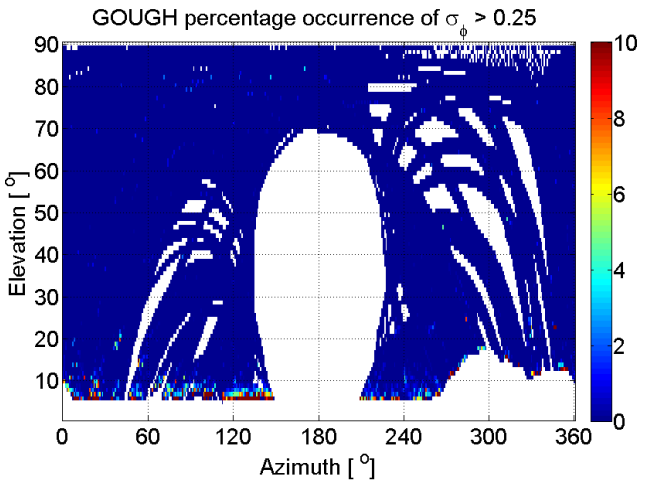

(b) Percentage occurrence of $\sigma_\phi > 0.25$ per azimuth-elevation bin over one year.

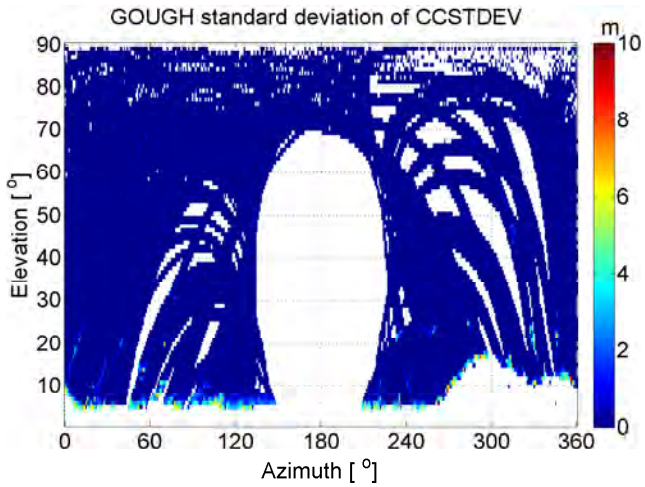

(c) The standard deviation of the code-carrier divergence standard deviation per azimuth-elevation bin over one year.

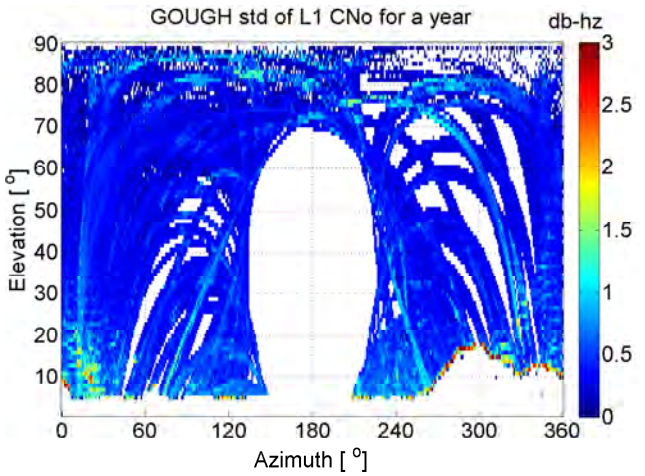

(d) Standard deviation of L1 CNo per azimuth-elevation bin over one year.

Figure 4.12: Percentage of occurrence of (a) S_4, (b) σ_ϕ, and the standard deviation of (c) CCSTDDEV, and (d) L1 CNo throughout the year (May 2009 to April 2010) plotted on an azimuth-elevation map. The blank bins on the azimuth-elevation maps shows that there are no ray paths traversing these bins.

In Figure 4.12(b) a high percentage of occurrence of $\sigma_\phi > 0.25$ is observed at lower elevation angles. This confirms that the horizon is the main source of multipath effects for this GISTM station. The Code-Carrier divergence index is a good indicator of multipath effects, since there will be no significant code-carrier divergence if the scintillation is due to the ionosphere. Therefore, we have plotted the standard deviation of CCSTDDEV (Standard Deviation of Code-Carrier divergence) on an azimuth-elevation map as shown in Figure 4.12(c) to identify the multipath area on an azimuth-elevation plot. High values of CCSTDDEV near the horizon show that signals are affected by multipath errors from the horizon, which also confirms what we have seen from the S_4 occurrence plot in Figure 4.12(a). The signal to noise ratio on L1 (see Figure 4.12(d)) also shows high signal degradation near the horizon, which indicates that the probability of interfering indirect signals increases as the ray paths come closer to the horizon.

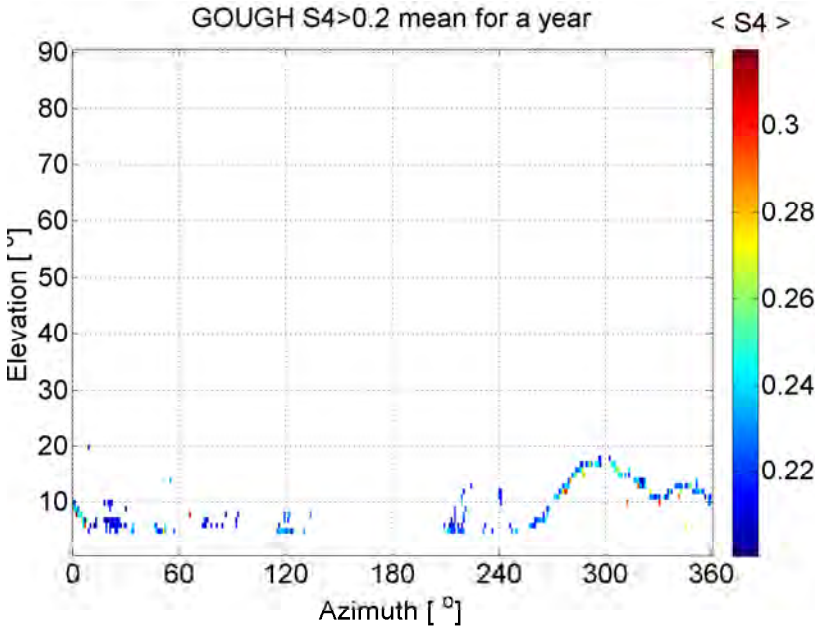

Figure 4.13: Mean of $S_4 > 0.2$ per azimuth-elevation bin for over year data.

From the results in Figures 4.12 and 4.13 we can also observe the variation of the horizon in every direction. The horizon rises up to 20° elevation angle in the Northwest direction and it drops to 5° elevation angle in the azimuth range 10° - 150°. The structures in the environment were identified by using the panoramic picture shown in Figure 4.14. In Figure 4.14, there is a mountain in the Northwest direction of the receiver that is preventing GPS signals from reaching the receiver and causing refraction and reflection of signals close to the horizon. Since it is observed that signals that are coming from lower elevation angles are distorted by the multipath effect of the horizon, modelling an elevation mask that can filter out signals that have high scintillation will be the next step. In order to do that we used the amplitude scintillation data for one year as shown in Figure 4.15(a). Elevation angles that correspond to $S_4 > 0.2$ are plotted vs. azimuth to represent the multipath region.

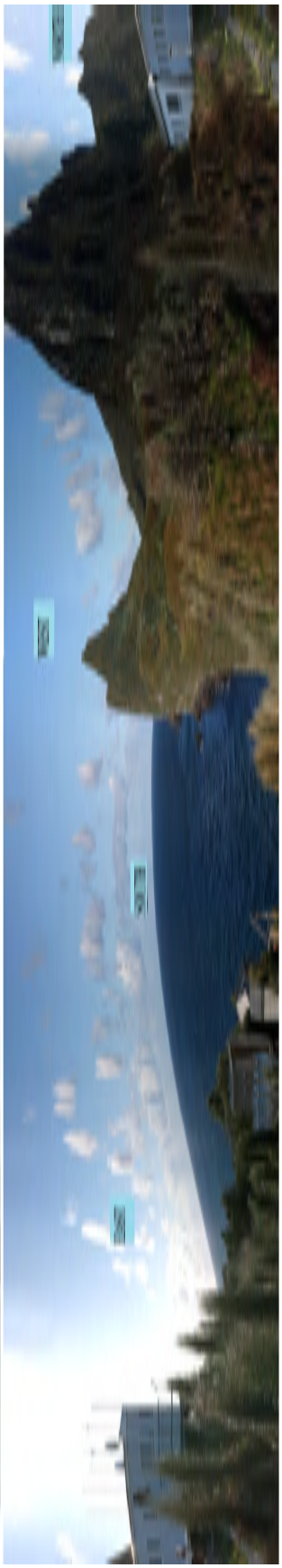

Figure 4.14: Panoramic view of the surrounding environment of the Gough island GISTM receiver antenna.

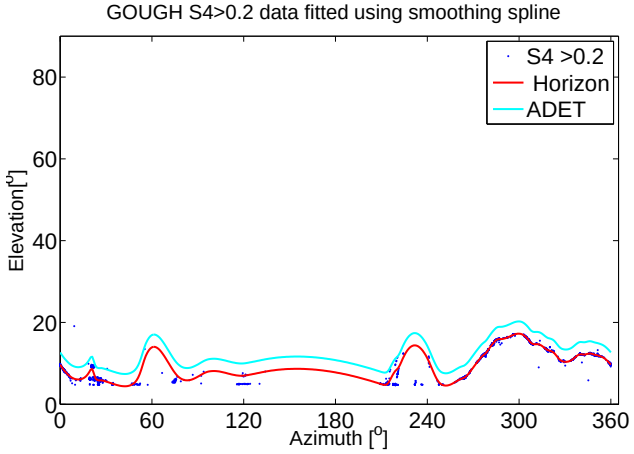

(a) The curve fitted to the horizon and the Azimuth Dependent Elevation Threshold (ADET) used to filter out multipath signals.

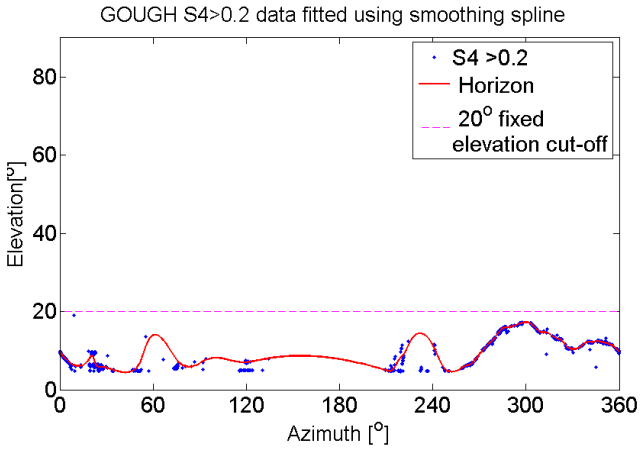

(b) A fixed elevation threshold of 20° used to filter out multipath signals.

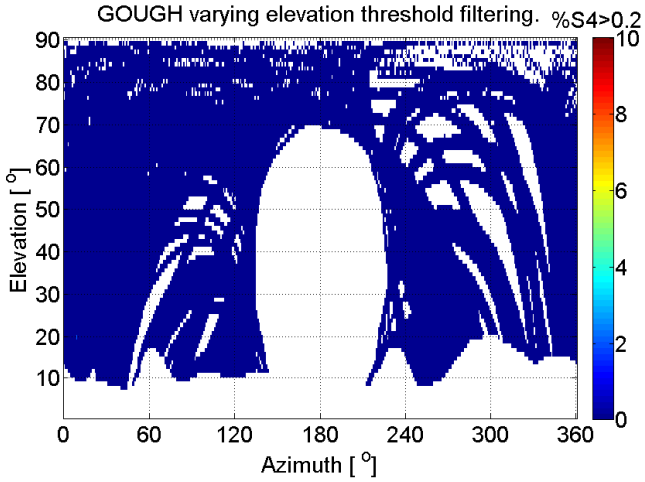

(c) Azimuth-elevation map of $S_4 > 0.2$ occurrence percentage filtered using ADET.

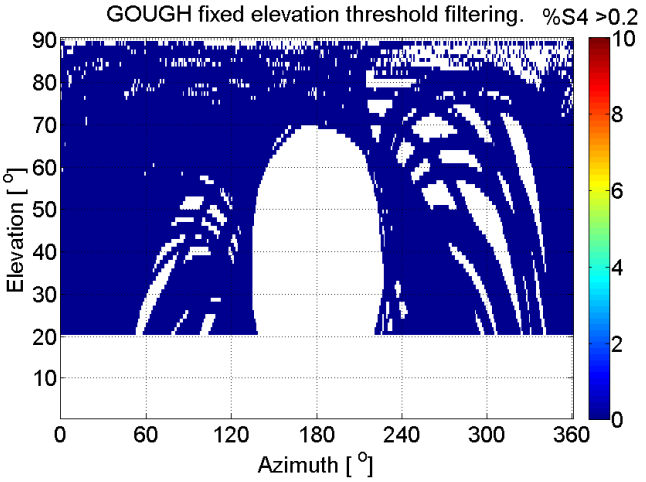

(d) Azimuth-elevation map of $S_4 > 0.2$ occurrence percentage filtered using a fixed elevation threshold value of 20°.

Figure 4.15: Comparison of two methods to filter out GPS signals that are affected by multipath sources.

Figure 4.15(a) shows the Azimuth Dependent Elevation Threshold (ADET) obtained by a spline fit to the high scintillation area of the azimuth-elevation plot and adding a fixed increment. The increment ($\Delta\epsilon = 3°$) is determined to give less than 0.1% occurrence of $S_4 > 0.2$ values as shown in Figure 4.16.

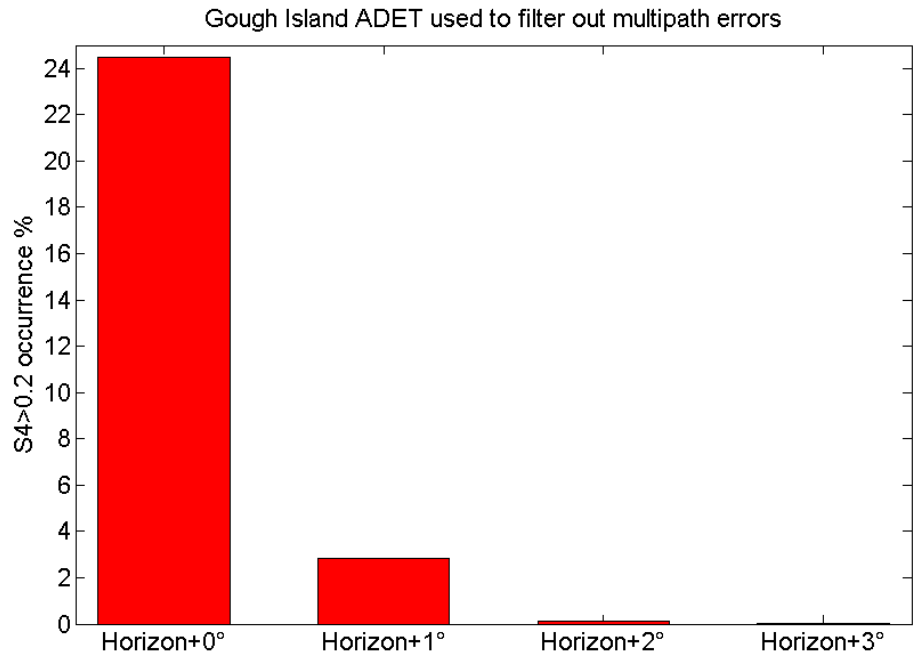

Figure 4.16: Histogram of $S_4 > 0.2$ occurrence percentage used to determine the $\Delta\epsilon$ value that should be added to the horizon to filter out multipath signals from the horizon.

The percentage of occurrence of $S_4 > 0.2$ obtained by using the ADET as shown in Figure 4.15(c), but this time we used ADET. High scintillation values that are the result of the multipath effect of the horizon are removed by the ADET. In Figure 4.15(d) a fixed-elevation threshold angle of 20° is used to remove the multipath sources. Comparing the ADET in Figure 4.15(c) with the fixed-elevation threshold in Figure 4.15(d), the ADET filters out the multipath signal effectively without losing useful data. Since the elevation of the horizon of the station varies with azimuth angle we lose useful data that is not distorted by multipath effects by using the fixed elevation threshold.

4.4 Hermanus GISTM receiver

This section presents the scintillation data analysis done for characterizing the multipath environment of the GISTM receiver at SANSA Space Science in Hermanus. The Hermanus GISTM receiver is located at 34.42° S and 19.22° E. One year of scintillation data taken from July 2009 to June 2010, with a 94% data availability, was used for this analysis.

Because Hermanus is a mid-latitude station a low amplitude scintillation, average S_4 values between 0.1 and 0.2, is observed over the one year scintillation data. Therefore, the repeated scintillation occurred were identified using a threshold of $S_4 > 0.1$. Figure 4.17(a) shows the percentage of occurrence of $S_4 > 0.1$ plotted on an azimuth-elevation map, with a 10% scale limit. Most of the amplitude scintillations with $S_4 > 0.1$ occur below 20° elevation in all directions, around the antenna. For azimuth angles between 150° and 210°, which correspond to approximately South, there is no satellite visibility (refer Figure 3.4(b)). The receiver only logged data above a built-in elevation threshold of 10°.

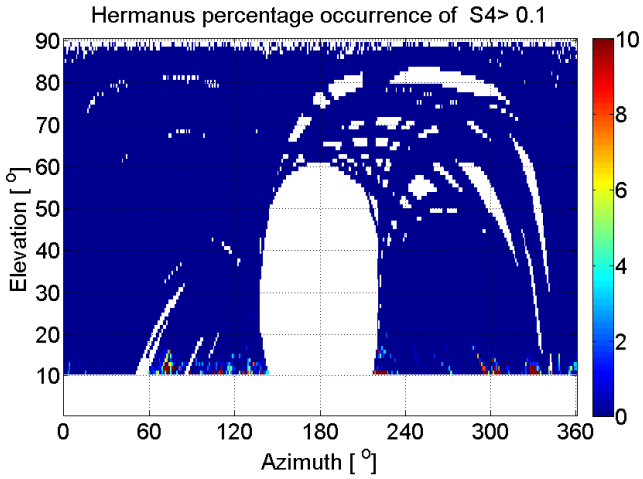

(a) Azimuth-elevation map of percentage occurrence of $S_4 > 0.1$ per each azimuth-elevation bin for one year.

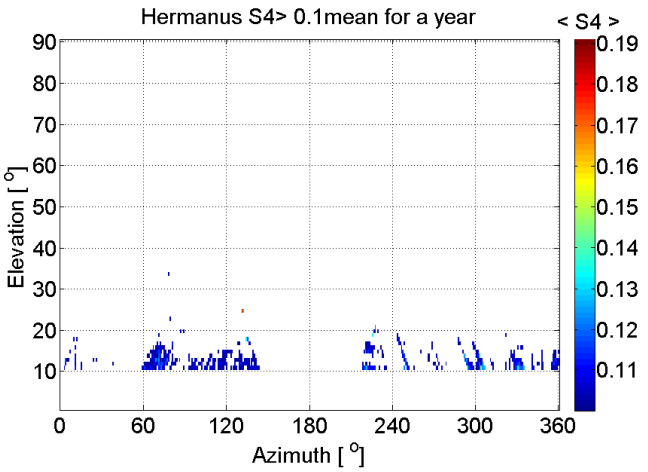

(b) Azimuth-elevation map of $S_4 > 0.1$ averaged per azimuth-elevation bin over one year data.

Figure 4.17: Azimuth-elevation maps of $S_4 > 0.1$ (a) occurrence percentage and (b) mean over one year

The S_4 mean shown in Figure 4.17(b) also confirms that $S_4 > 0.1$ are observed mostly below a 20° elevation angle, which shows that the multipath effect of the horizon extends up to 20° elevation angles. The panorama of the surrounding environment of the antenna in Figure 4.18 shows physical structures like the mountain located in the North and the buildings found near the antenna, which can be sources of multipath signals. The physical structures that are both near and far from the receiver are expected to be the sources of scintillations observed in Figure 4.17(a) and 4.17(b) because of multipath signals that can be introduced via reflection and

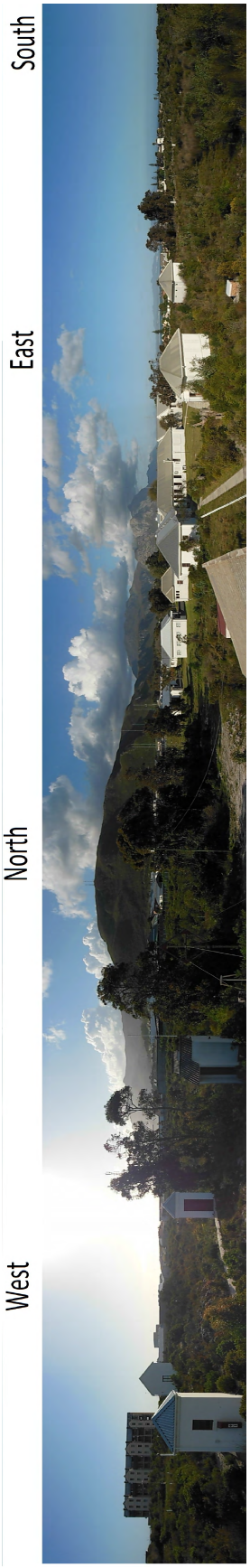

Figure 4.18: Panoramic view of the environment surrounding the Hermanus GISTM receiver antenna.

refraction by these structures.

After we identify the areas that are affected by multipath signals from the azimuth-elevation map, the next step is to develop an azimuth angle-dependent elevation threshold that can be used to filter out multipath signals effectively. The horizon for the GISTM antenna is obtained by fitting a curve to areas that have high scintillation as shown in Figure 4.20(a) (plotted in red). The required ADET used to mask out all high scintillation areas is derived from the horizon obtained from the curve fitting and adding a margin $\Delta\epsilon$ (see the curve plotted in cyan in Figure 4.20(a)). The $\Delta\epsilon$ value used to get an ADET that can filter multipath signals with less than 0.1% occurrence of $S_4 > 0.1$ is 2° (see Figure 4.19).

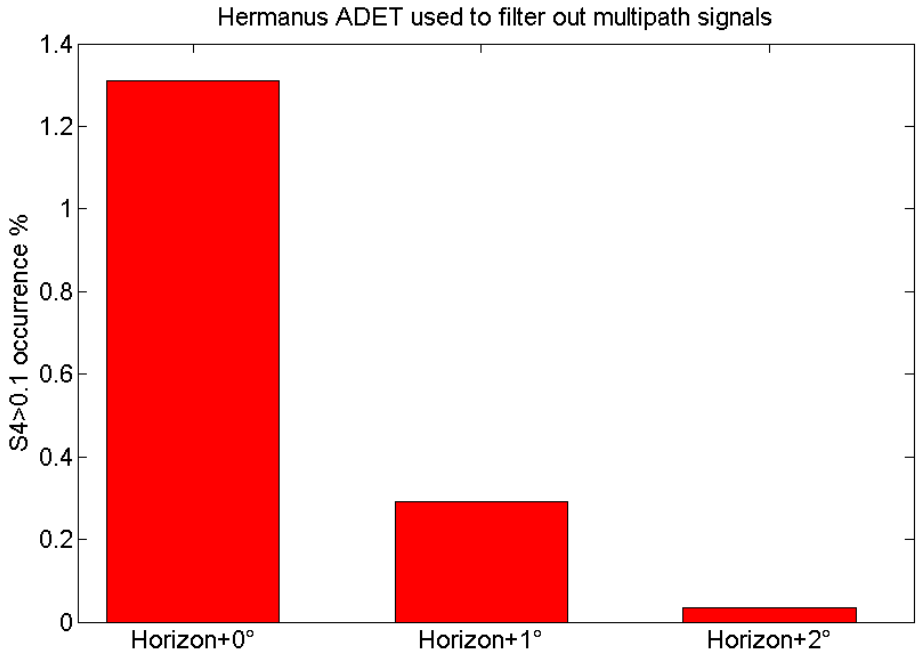

Figure 4.19: Histogram of percentage occurrence of $S_4 > 0.1$ used to determine the margin $\Delta\epsilon$ that must be added to the horizon to filter out $S_4 > 0.1$ values.

Figures 4.20(c) and 4.20(d) show the occurrence percentage of $S_4 > 0.1$ on the azimuth-elevation map, using ADET and a fixed elevation angle of 20° to filter out high scintillations that are caused by multipath effects. The ADET used to filter out the multipath signals was able to remove high scintillations that are due to the multipath effect as can be seen from the S_4 occurrence percentage map in Figure 4.20(c). The 20° fixed elevation threshold used to filter out multipath signals was not able to remove all occurrences of scintillation since there are high-scintillation areas that are above the 20° elevation cut off as shown in Figure 4.20(b). The percentage of data (above 10° elevation angle) that will be lost when we filter out the multipath signals using a 20° fixed elevation threshold is reduced by 5% when the ADET method is used to filter out multipath signals.

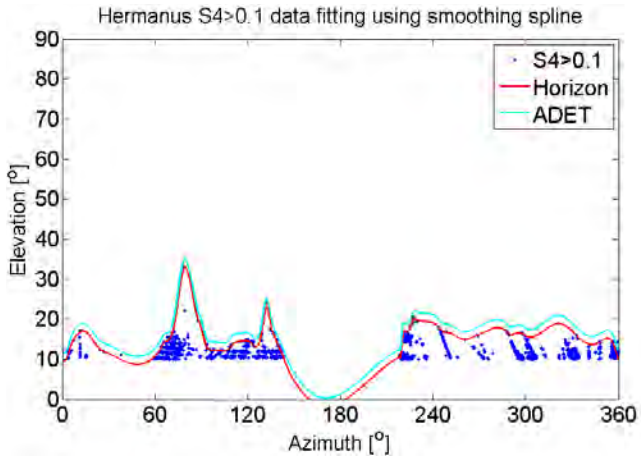

(a) The curve fitted to the horizon and the ADET used to filter out multipath signals.

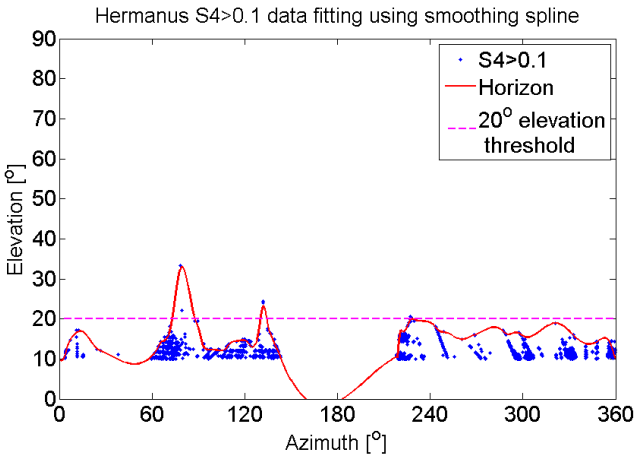

(b) A fixed elevation threshold of 20° used to filter out multipath signals.

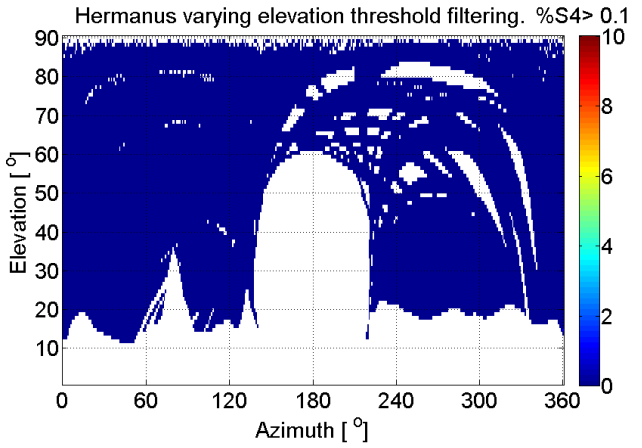

(c) Azimuth-elevation map of $S_4 > 0.2$ occurrence percentage filtered using ADET.

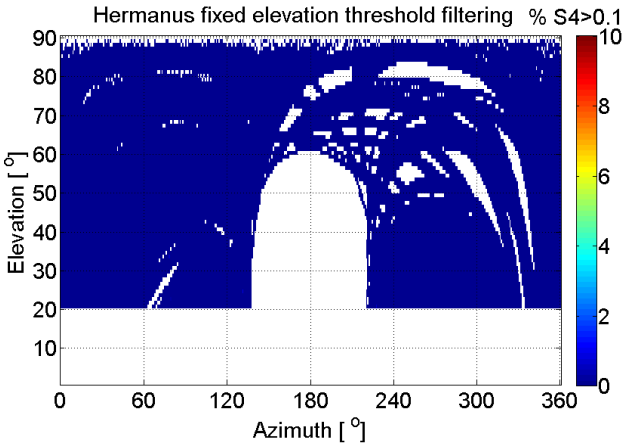

(d) Azimuth-elevation map of $S_4 > 0.2$ occurrence percentage filtered using a fixed elevation threshold value of 20°.

Figure 4.20: Comparing two multipath filtering methods one using (a) ADET and (b) 20° fixed elevation threshold and their implementation on S_4 occurrence plots (c) & (d) respectively.

4.5 Marion Island GISTM receiver

This section presents the analysis and discussion of the multipath environment characterization for the GISTM antenna on Marion Island. The Marion Island GISTM receiver is located at 46.87° S and 37.86° E (see Figure 3.3). In the analysis we used one year of scintillation data, from May 2009 to April 2010, with a 94% data availability.

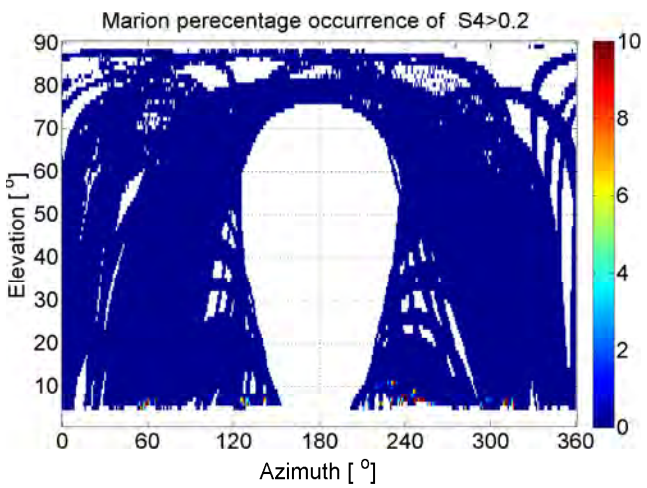

(a) Azimuth-elevation map of the percentage occurrence for $S_4 > 0.2$ per azimuth-elevation bin for one year of data.

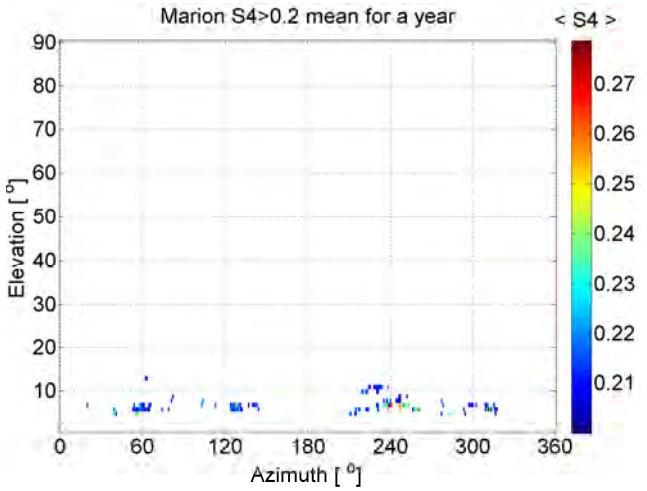

(b) An azimuth-elevation map of mean value of $S_4 > 0.2$ calculated for each azimuth-elevation bin for one year of data.

Figure 4.21: Azimuth-elevation maps of $S_4 > 0.2$ (a) occurrence percentage and (b) mean for one year of data

Figure 4.21(a) shows the percentage of occurrence of $S_4 > 0.2$ for the selected period. The built-in minimum elevation angle of satellite visibility is set to 5° by the receiver software. Most of the strong scintillations that are prominent throughout the year are observed at a less than 10° elevation angle on the azimuth-elevation map. The higher occurrence of amplitude scintillation $S_4 > 0.2$ observed at about 12° in the Southwest (around 230° azimuth angle) in azimuth-elevation space is caused by the multipath effect of the mountain located to the Southwest of the antenna, as can be seen in the picture of the environment surrounding the antenna in Figure 4.22. The average of $S_4 > 0.2$ plotted on the azimuth-elevation map in Figure 4.21(b) also shows high-amplitude scintillations, with values between 0.2 and 0.28 occurring at elevation angles of less than 15°.

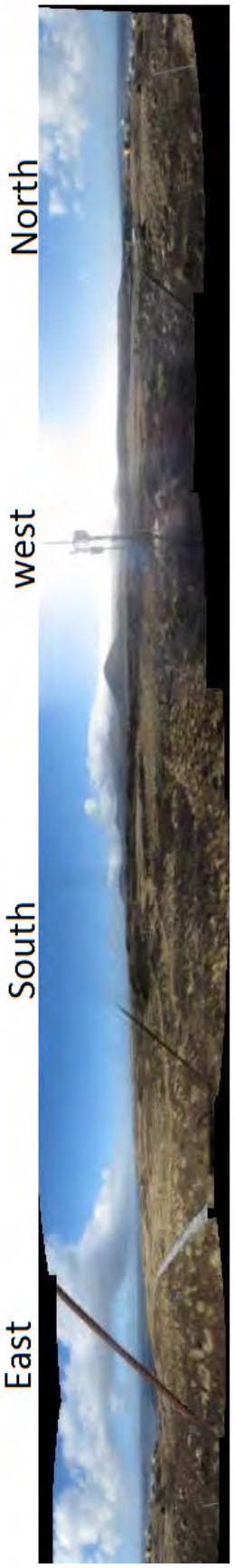

Figure 4.22: Panoramic view of the surrounding environment of the Marion Island GISTM receiver antenna.

Figure 4.24(a) shows the elevation threshold that varies with the azimuth angle, derived using curve fitting to the high scintillation areas and by adding an additional fixed value $\Delta\epsilon$. Figure 4.23 shows the occurrence percentage of $S_4 > 0.2$ when using the horizon plus $\Delta\epsilon$ values $0°, 1°$ and $2°$ to filter out multipath signals. For this station we use the horizon, derived from the curve fitting, plus $\Delta\epsilon = 2°$ (see Figure 4.24(a)) as the ADET, which gives a 0% occurrence percentage of $S_4 > 0.2$ as shown in Figure 4.23.

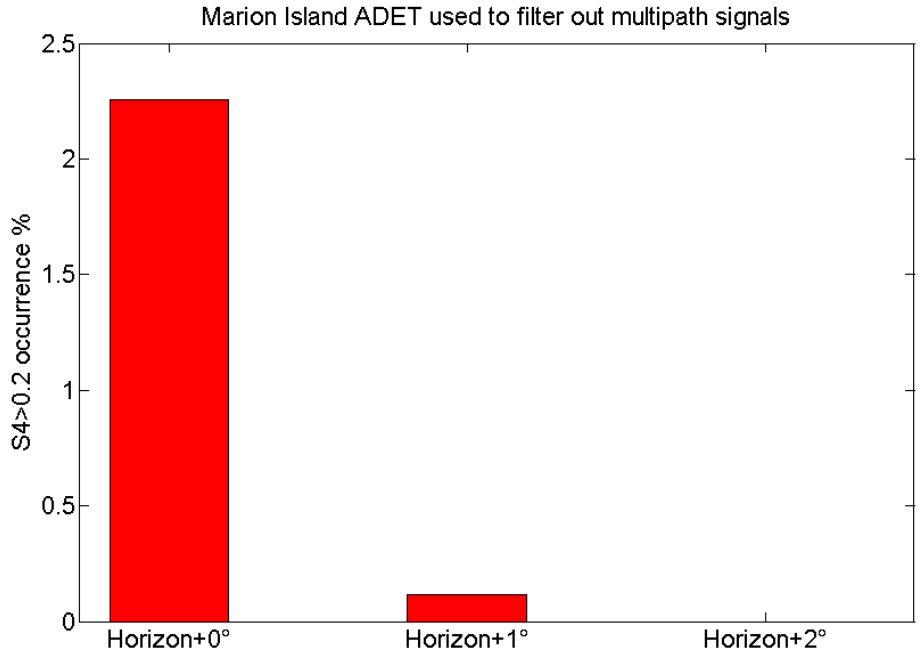

Figure 4.23: Histogram of $S_4 > 0.2$ occurrence percentage used to determine $\Delta\epsilon$ value that can be added to the horizon to filter out multipath signals.

To compare the method with the usual way of removing multipath errors we took a 20° fixed-elevation threshold shown in Figure 4.24(b). Figure 4.24(d) shows the S_4 occurrence plotted on an azimuth-elevation map only for signals from elevation angles greater than 20°. We can see that this method also removes multipath signals. Comparing the amount of data removed by using a fixed-elevation threshold with the ADET, the fixed-elevation threshold causes a significant data loss. The ADET method removes 7% of the data that is affected by multipath errors, while the 20° fixed-elevation threshold method removes an additional 28% of the data, that is non-multipath related, in order to filter-out the multipath errors.

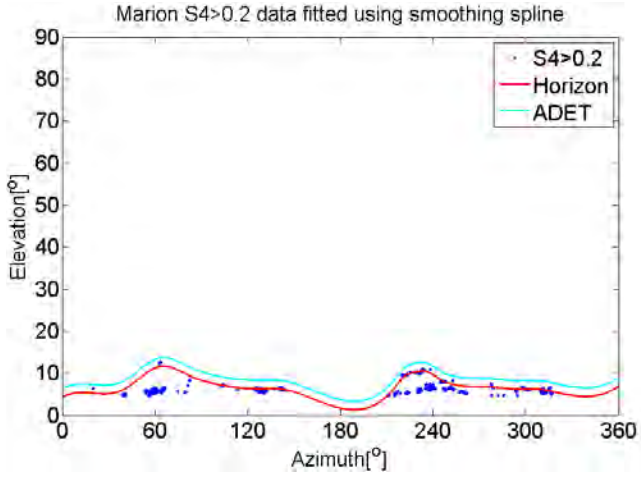

(a) The curve fitted to the horizon and the ADET used to filter out multipath signals.

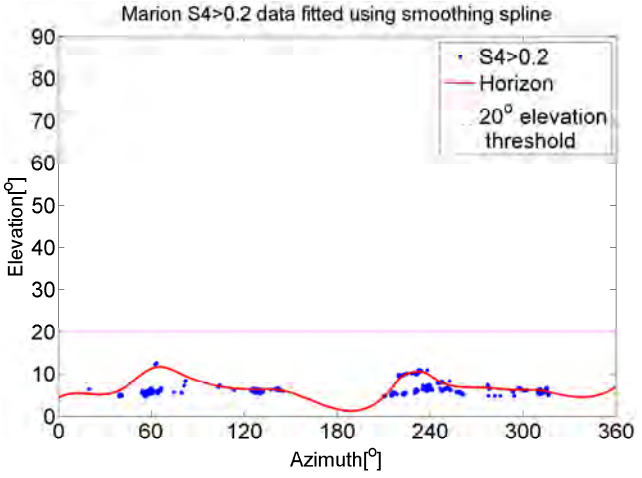

(b) A fixed elevation threshold of 20° used to filter out multipath signals.

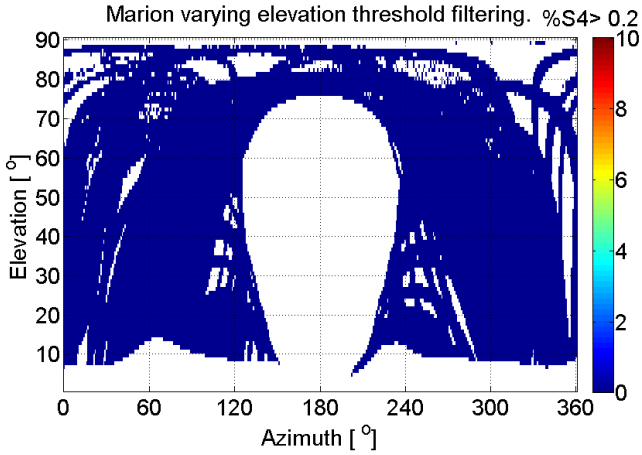

(c) $S_4 > 0.2$ occurrence percentage after filtered using ADET.

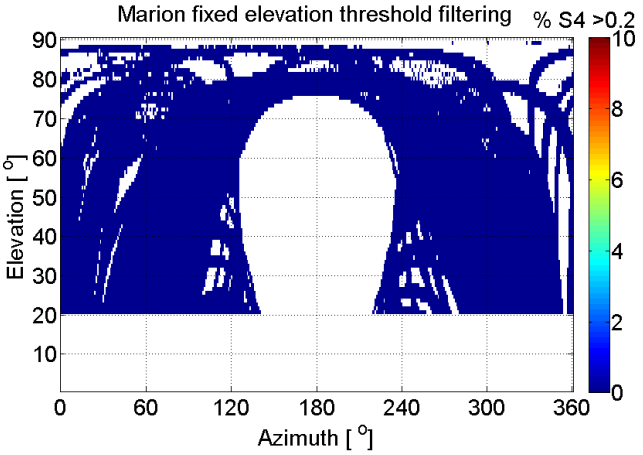

(d) $S_4 > 0.2$ occurrence percentage after filtered with a fixed elevation threshold value of 20°.

Figure 4.24: Comparing (a) ADET and (b) 20° fixed-elevation threshold used to filter out multipath signals implemented on an azimuth-elevation map of $S_4 > 0.2$ occurrence percentage (c) and (d), respectively.

4.6 SANAE IV GISTM receiver

The other GISTM station selected for multipath characterization is from a higher latitude, located at the South African National Antarctic Expedition station (SANAE IV) in Antarctica (geographical coordinates 71.67° S and 2.84° W). The scintillation monitor at SANAE IV was deployed during the International Polar Year (IPY) 2007-2009 to study the dynamics of the ionosphere at higher latitudes. The analysis was done using one year of scintillation data, from 1 January to 31 December 2009, of which 99% of the data was available.

The occurrence percentage and average value calculated for each azimuth-elevation bin for one year data of scintillation parameters S_4 and σ_ϕ are plotted in an azimuth-elevation map in Figure 4.25. The plots are used to identify areas that consistently have scintillations throughout the selected period. These areas are correlated with the physical structures that are found in the vicinity of the antenna (see Figure 4.27). These structures can result in multipath signals that can lead to the high scintillations on the signal amplitude and phase. For SANAE IV, $S_4 > 0.2$ and $\sigma_\phi > 0.6$ are designated as high scintillation values.

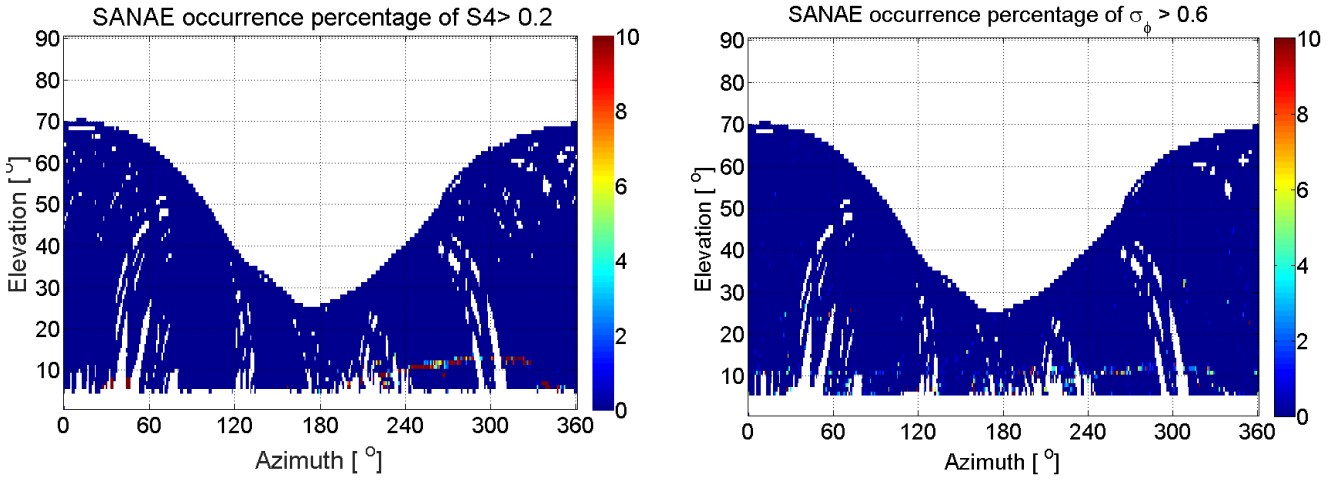

(a) Azimuth-elevation map of the percentage occurrence of $S_4 > 0.2$ per azimuth-elevation bin over one year.

(b) Azimuth-elevation map of the percentage occurrence of $\sigma_\phi > 0.6$ per azimuth-elevation bin over one year.

Figure 4.25: Azimuth-elevation map of percentage of occurrence of (a) S_4 and (b) σ_ϕ for the calendar year 2009.

Both amplitude and phase scintillation occurrence plots in Figures 4.25(a) and 4.25(b), respectively, show a high percentage of occurrence of $S_4 > 0.2$ and $\sigma_\phi > 0.6$ at elevation angles below 15°. Figure 4.26 shows that mean values of S_4 in the range 0.2 to 0.32 occur at elevation angles of less than 15°.

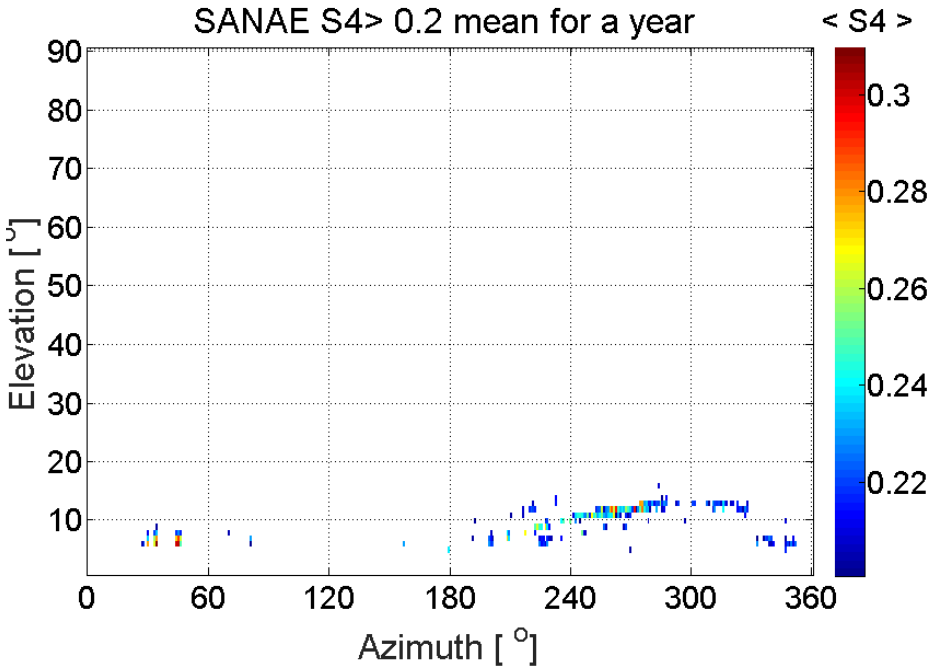

Figure 4.26: Azimuth-elevation map of average values of $S_4 > 0.2$ calculated per azimuth-elevation bin over one year of data

The building found at the North-East of the antenna and the rocky hill at the West of the antenna shown in Figure 4.27 are expected to be the main sources of the scintillations observed both on the phase and amplitude of the signals.

Figure 4.27: panoramic view of the surrounding environment of the SANAE IV GISTM receiver antenna.

In order to reduce the errors that multipath signals can introduce, a varying threshold (or an azimuth dependent elevation threshold) was modelled specifically for this station. The ADET shown in Figure 4.29(a) was developed by fitting a curve to the high-scintillation areas using a MATLAB curve fitting tool and adding a fixed value of $\Delta\epsilon = 3°$. The horizon plus the $\Delta\epsilon$ value is determined to give less than 0.1% percentage occurrence of $S_4 > 0.2$, when used as ADET to filter out high scintillation values (see Figure 4.28).

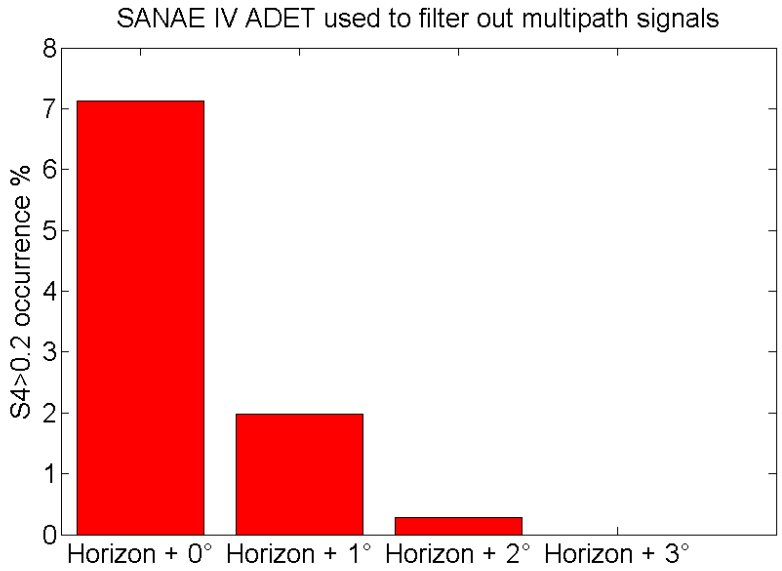

Figure 4.28: Histogram of $S_4 > 0.2$ occurrence percentage used to determine $\Delta\epsilon$ value that can be added to the horizon to filter out multipath signals.

The S_4 occurrence percentage was plotted in Figure 4.29(c) using the ADET to mask out the high scintillation. It is evident from Figure 4.29(c) that all of the high scintillations are effectively removed. To compare the use of ADET with a fixed-elevation threshold shown in Figure 4.29(b), we plotted the S_4 occurrences that are above the 20° elevation angle in the azimuth-elevation map (see Figure 4.29(d)). Out of the available data, using a fixed-elevation threshold will remove 33% of the data. By using an azimuth-dependent elevation threshold we only remove 11% of the data and we are still be able to effectively reduce the multipath errors. This amounts to an improvement of 22% on the available data for ionospheric characterization. This improvement can be seen in the scintillation climatology analysis (see Figure 4.30).

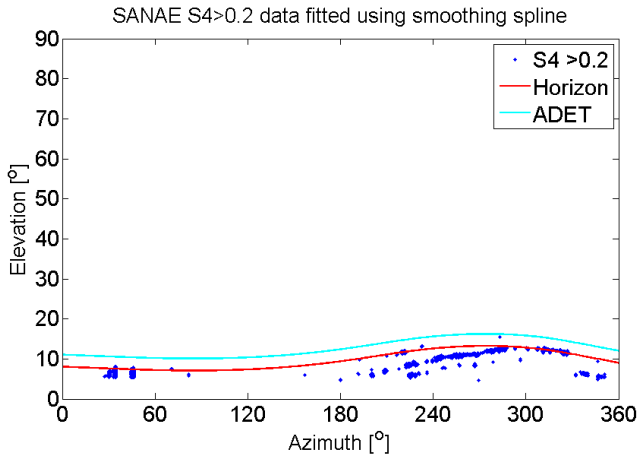

(a) The ADET plus 3° elevation threshold used to filter out multipath signals.

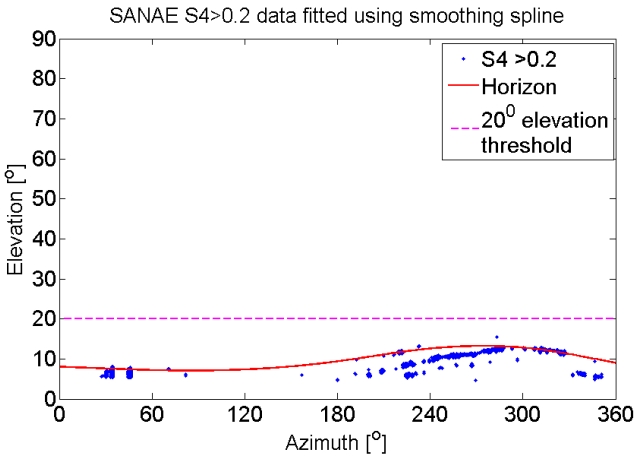

(b) A fixed elevation threshold of 20° used to filter out multipath signals.

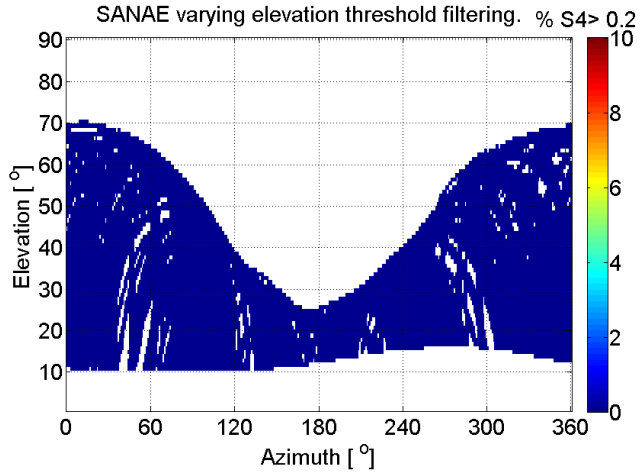

(c) $S_4 > 0.2$ occurrence percentage after filtered using azimuth dependent elevation thresholds.

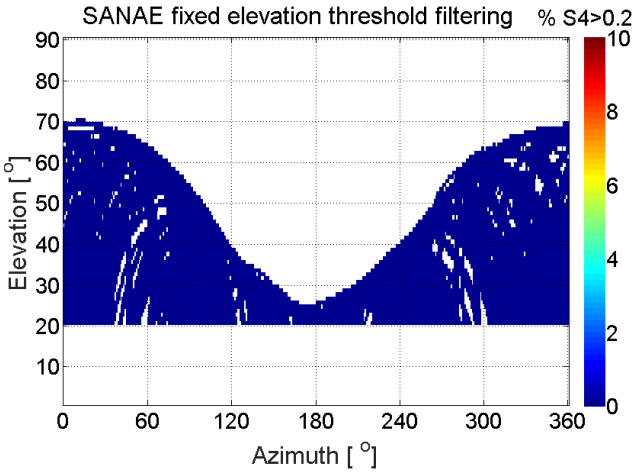

(d) $S_4 > 0.2$ occurrence percentage after filtered with a fixed elevation threshold value of 20°.

Figure 4.29: Comparing the ADET with a 20° fixed-elevation threshold method used to filter out multipath signals.

Figure 4.30 shows an occurrence percentage of $\sigma_\phi > 0.6$ with longitude and latitude for the calendar year 2009. Climatology plots are used to study the spatial and temporal variation of ionospheric scintillations. In Figure 4.30(a) a fixed elevation threshold of 20° was used. The ADET developed specifically for this station was used to filter out the multipath errors in the climatology analysis shown in Figure 4.30(b). Comparing the climatology plot in Figure 4.30(a) and 4.30(b), it can be seen that by using the fixed-elevation threshold we lost some useful data for the scintillation climatology analysis.

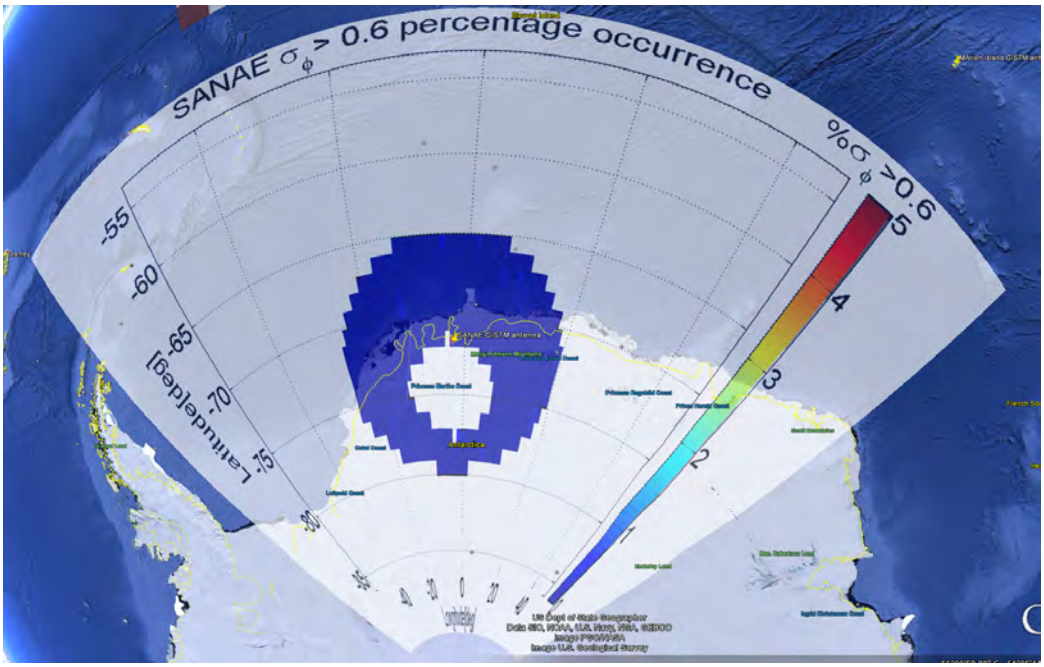

(a) The occurrence percentage of $\sigma_\phi > 0.6$ plotted with longitude and latitude during the year 2009 using a fixed 20° elevation cutoff to remove the multipath errors.

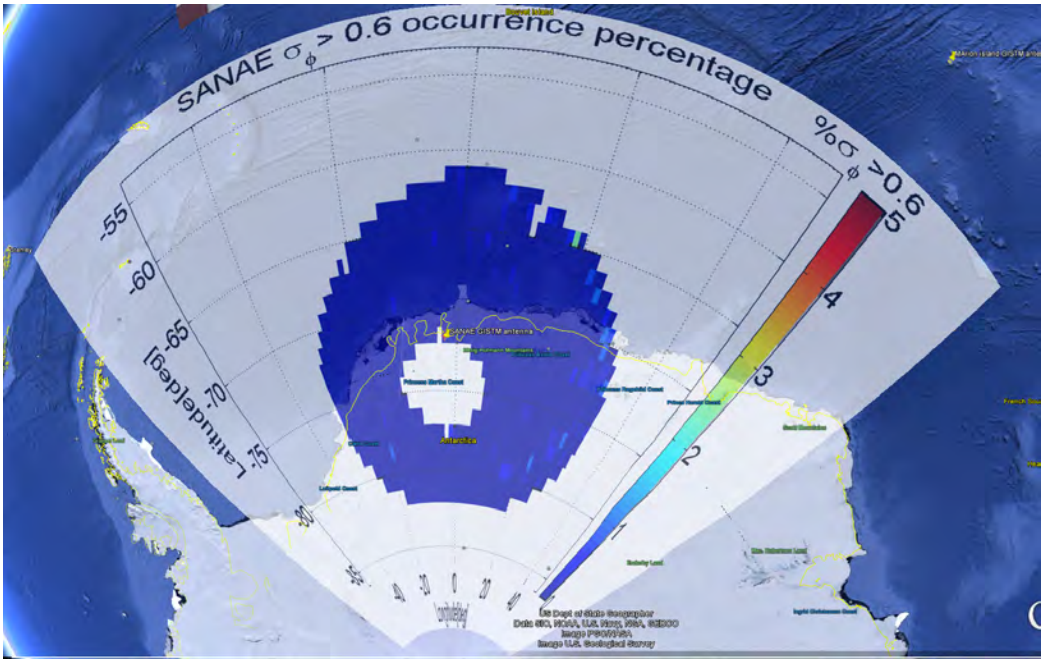

(b) The occurrence percentage of $\sigma_\phi > 0.6$ plotted with longitude and latitude during the year 2009 using an azimuth-dependant elevation threshold (ADET) to remove the multipath errors.

Figure 4.30: Comparison between a fixed-elevation threshold and ADET used to filter out multipath errors in scintillation climatology analysis.

Chapter 5

Conclusion

5.1 Summary of main findings

Multipath effects are one of the most significant sources of error in GNSS. Multipath signals introduce errors that degrade the accuracy of GNSS navigation and positioning systems. Ionospheric scintillation studies, which includes investigation of the formation and evolution of ionospheric irregularities, need quality data. Scintillations that are due to multipath signals reflected from the surrounding physical environment of the receiver antenna, have been demonstrated to degrade the usefulness of GNSS data.

In this project we have shown how to identify areas in azimuth-elevation space that are affected by multipath signals, using the GNSS station characterisation method from Romano *et al.* (2013). In the multipath environment characterization method we used azimuth-elevation maps of scintillation indices (S_4 index and σ_ϕ index), which represent the surrounding environment of the receiver antenna in azimuth-elevation space. The azimuth-elevation maps of CCSTDDEV and L1 CNo were also used for the identification of areas affected by multipath signals. Areas on the azimuth-elevation map that show repeated strong scintillation occurrence throughout the year are most likely to be errors dominated by multipath effects of stationary reflecting physical structures in the vicinity of the receiver antenna, such as mountains, trees or buildings.

A station-specific characterization was required because the geographical horizon

of the receiver antenna is different for each station. It is observed that the multipath effect occurs on GNSS ray paths with elevations up to 20° above the geographical horizon, due to reflecting physical structures, like trees. The effect was pronounced for the Hermanus GISTM station, which is surrounded by big trees, poles and buildings. Signals coming from satellites above the horizon can combine with signals reflected by the horizon. In this case we will observe scintillation on the azimuth-elevation map at elevation angles above the horizon. For the SANAE IV station, at low elevation angles around 5°, where the visibility of satellites are limited, the scintillation occurrence was low while there was high scintillation occurrence at elevation angles in the range 10° to 15°. These scintillations above the horizon might be due to reflections from the ice.

From the multipath environment characterization we are able to identify the geographical horizon of each GISTM receiver antenna. We added a margin above the horizon to develop an azimuth-dependent elevation threshold that can be used to minimize multipath errors. The margin above the horizon varies from station to station. The margin was derived from the condition that the occurrence of the S_4 values that are above a given threshold value used in the characterization, are less than 0.1%.

The ADET method improves the quality of the available data by effectively removing multipath errors. This method also gives more useful data by reducing the amount of the data that would be lost if a fixed-elevation threshold were used. For the Gough Island GISTM station the 20° fixed-elevation threshold removes 31% of the available data, while the ADET removes 12% of the available data. Therefore the ADET method increases the useful scintillation data by 19%.

For the Hermanus GISTM station we observed that the 20° fixed-threshold was not enough to filter out all of the signals that are affected by multipath effects and at the same time, out of the available data, 23% will be removed by using a fixed 20° elevation filtering method. The ADET developed for the Hermanus GISTM shows a better multipath signal filtering result than the fixed threshold. The ADET filtering method reduced the high scintillation occurrence due to multipath signals to less than 0.1% by only removing 18% of the available data.

For the Marion Island scintillation data, we showed that a 20° fixed-elevation threshold will remove 35% of the available data, while the ADET developed for the Marion Island GISTM station filters out only 7% of the available data. This shows that by using ADET we can save 28% of the data that was previously removed and use them for scintillation studies.

We showed that for the SANAE IV GISTM station, 33% of the available data were filtered out when using a fixed threshold angle of 20°. Using the ADET method only 11% of the available data are removed.

In this project we have characterized the multipath environment of four GISTM

stations that are located in different geographical locations. From the characterization we were able to develop station-specific azimuth-dependent elevation thresholds that can be used to filter out multipath signals introduced by the physical environment of the receiver antenna. We have shown that, by using the station-specific azimuth-dependent elevation thresholds, we can improve the data quality. Comparing this method to a fixed-elevation threshold of 20°, we can get 5% to 28% more useful data.

5.2 Recommendations for future research

The characterization of the multipath environment of GISTM receiver antennas can be applied to other GISTM stations to improve both quality and quantity of GNSS data. In ionospheric studies TEC derived from standard GNSS RINEX data are used to characterize the spatial and temporal distribution of the electron density in the ionosphere. Ionospheric studies need to be based on data that only represent the ionosphere and don't include signals that are distorted by multipath effect of stationary physical structures. Therefore, characterizing the multipath environment of the GNSS receiver antenna and developing an azimuth-dependent elevation threshold is very important to reduce the multipath error without losing useful data for post-processing of GNSS data in ionospheric studies. Scintillation proxies derived from RINEX data (Amabayo *et al.*, 2015; Prikryl *et al.*, 2013) can be used for deriving the ADET for GNSS stations where there are no co-located GISTM receivers.

References

Alfonsi, L., Spogli, L., De Franceschi, G., Romano, V., Aquino, M., Dodson, A., and Mitchell, C. N.: Bipolar climatology of GPS ionospheric scintillation at solar minimum, Radio Science, 46, doi:10.1029/2010RS004571, URL http://dx.doi.org/10.1029/2010RS004571, rS0D05, 2011.

Amabayo, E. B., Jurua, E., and Cilliers, P. J.: Validating the use of scintillation proxies to study ionospheric scintillation over the Ugandan region, Journal of Atmospheric and Solar-Terrestrial Physics, 128, 84 – 91, doi:http://dx.doi.org/10.1016/j.jastp.2015.03.006, URL http://www.sciencedirect.com/science/article/pii/S1364682615000541, 2015.

Aquino, M., Moore, T., Dodson, A., Waugh, S., Souter, J., and Rodrigues, F. S.: Implications of ionospheric scintillation for GNSS users in Northern Europe, Journal of Navigation, 58, 241–256, 2005.

Basu, S., Groves, K., Basu, S., and Sultan, P.: Specification and forecasting of scintillations in communication/navigation links: current status and future plans, Journal of Atmospheric and Solar-Terrestrial Physics, 64, 1745 – 1754, doi:http://dx.doi.org/10.1016/S1364-6826(02)00124-4, URL http://www.sciencedirect.com/science/article/pii/S1364682602001244, space Weather Effects on Technological Systems, 2002.

Beach, T. L.: Global positioning system studies of equatorial scintillations, Ph.D. thesis, Cornell University, 1998.

Beach, T. L.: Perils of the GPS phase scintillation index (σ_ϕ), Radio Science, 41, doi:10.1029/2005RS003356, URL http://dx.doi.org/10.1029/2005RS003356, rS5S31, 2006.

Briggs, B. and Parkin, I.: On the variation of radio star and satellite scintillations with zenith angle, Journal of Atmospheric and Terrestrial Physics, 25, 339 – 366, doi:http://dx.doi.org/10.1016/0021-9169(63)90150-8, URL http://www.sciencedirect.com/science/article/pii/0021916963901508, 1963.

Carrano, C. S. and Groves, K.: The GPS segment of the AFRL-SCINDA global network and the challenges of real-time TEC estimation in the equatorial ionosphere, in: Proceedings of the 2006 National Technical Meeting of The Institute of Navigation, pp. 1036–1047, 2006.

Carrano, C. S., Groves, K. M., and Griffin, J. M.: Empirical characterization and modeling of GPS positioning errors due to ionospheric scintillation, in: Proceedings of the Ionospheric Effects Symposium, Alexandria, VA, 2005.

Cmglee, G. S.: Comparison satellite navigation orbits.svg, http://commons.wikimedia.org/wiki/File:Comparisonsatellitenavigationorbits.svg, [Online; accessed 20-May-2015], 2011.

Datta-Barua, S., Doherty, P., Delay, S., Dehel, T., and Klobuchar, J.: Ionospheric scintillation effects on single and dual frequency GPS positioning, in: Proceedings of ION GPS/GNSS, pp. 336–346, 2003.

Davies, K.: Ionospheric Radio, 31, United Kingdom, London, Peter Peregrinus Ltd., 1990.

El-Rabbany, A.: Introduction to GPS: The Global Positioning System, Artech House, 2002.

Elósegui, P., Davis, J., Jaldehag, R., Johansson, J., Niell, A., and Shapiro, I.: Geodesy using the Global Positioning System: The effects of signal scattering on estimates of site position, Journal of Geophysical Research: Solid Earth (1978–2012), 100, 9921–9934, 1995.

Erickson, W., Perley, R., Flatters, C., and Kassim, N.: Ionospheric corrections for VLA observations using Local GPS data, Astronomy & Astrophysics, 366, 1071–1080, 2001.

Farrell, J. and Barth, M.: The Global Positioning System and Inertial Navigation, vol. 61, New York, McGraw-Hill, 1999.

Francis, W. E. and Karplus, R.: Hydromagnetic waves in the ionosphere, Journal of Geophysical Research, 65, 3593–3600, doi:10.1029/JZ065i011p03593, URL http://dx.doi.org/10.1029/JZ065i011p03593, 1960.

Fremouw, E., Andreasen, C., Klein, M., and Lansinger, J.: Preliminary investigation of longitudinal differences in TEC and scintillation at transition latitudes. Final report, 3 Jun 89-31 Jan 91, Tech. rep., Northwest Research Associates, Inc., Bellevue, WA (United States), 1991.

Georges, T.: Effects of ionospheric motions and irregularities on HF radio propagation, in: Low-Frequency Waves and Irregularities in the Ionosphere, pp. 137–151, Springer, 1969.

Gleason, S. and Gebre-Egziabher, D.: GNSS Applications and Methods, Artech House, 2009.

GPS.GOV: Official U.S. Government information about the Global Positioning System (GPS) and related topics, http://www.gps.gov/systems/gps/, [Accessed: 2015-10-02], 2015.

Groves, K., Basu, S., Weber, E., Smitham, M., Kuenzler, H., Valladares, C., Sheehan, R., MacKenzie, E., Secan, J., Ning, P., *et al.*: Equatorial scintillation and systems support, Radio Science, 32, 2047–2064, 1997.

Hofmann-Wellenhof, B., Lichtenegger, H., and Collins, J.: Global Positioning System. Theory and Practice., New York, Springer-Verlag Wien, 1992.

Hunsucker, R. D. and Hargreaves, J. K.: The High-Latitude Ionosphere and its Effects on Radio Propagation, New York, Cambridge University Press, 2003.

Jacobson, M. Z.: Fundamentals of Atmospheric Modeling, New York, Cambridge university press, 2005.

Kaplan, E. D. and Hegarty, C. J.: Understanding GPS: Principles and Applications, Artech house, 2006.

Kelley, M. C. and Heelis, R. A.: The Earth's Ionosphere : Plasma Physics and Electrodynamics, California, San Diego, ACADEMIC PRESS, INC., 1989.

Kintner, P., Ledvina, B., De Paula, E., and Kantor, I.: Size, shape, orientation, speed, and duration of GPS equatorial anomaly scintillations, Radio Science, 39, 2004.

Kintner, P. M., Ledvina, B. M., and de Paula, E. R.: GPS and ionospheric scintillations, Space Weather, 5, doi:10.1029/2006SW000260, URL http://dx.doi.org/10.1029/2006SW000260, s09003, 2007.

Kohl, H., Rüster, R., and Schlegel, K.: Modern Ionospheric Science. A Collection of Articles Published on the Occasion of the Anniversary:"50 Years of Ionospheric Research in Lindau", Katlenburg-Lindau, European Geophysical Society, 1996.

KYOTO: World Data Center for Geomagnetism, Kyoto Dst index service, http://wdc.kugi.kyoto-u.ac.jp/wdc/Sec3.html, [Online; accessed 2015-06-07], 2015.

Ledvina, B. M., Makela, J. J., and Kintner, P. M.: First observations of intense GPS L1 amplitude scintillations at midlatitude, Geophysical Research Letters, 29, 4–1–4–4, doi:10.1029/2002GL014770, URL http://dx.doi.org/10.1029/2002GL014770, 2002.

Loewe, C. and Prölss, G.: Classification and mean behavior of magnetic storms, Journal of Geophysical Research: Space Physics (1978–2012), 102, 14 209–14 213, 1997.

Mannucci, A., Iijima, B., Lindqwister, U., Pi, X., Sparks, L., and Wilson, B.: GPS and ionosphere, Review of Radio Science 1996–1999, pp. 625–665, 1999.

McDonald, K. D.: The modernization of GPS: plans, new capabilities and the future relationship to Galileo, Positioning, 1, 2002.

McNamara, L. F.: The ionosphere: Communications, Surveillance, and Direction Finding, Krieger Publishing Company, 1991.

Misra, P. and Enge, P.: Global Positioning System: Signals, Measurements and Performance Second Edition, Lincoln, MA: Ganga-Jamuna Press, 2006.

Moeketsi, D. M.: Solar cycle effect on GNSS derived ionospheric Total Electron Content observed over South Africa, Ph.D. thesis, Rhodes University, 2007.

Mohinder, S. G., Weill, R. L., and Andrews, P. A.: Global Positioning Systems, Inertial Navigation, and Integration, A John Wiley and Sons, Inc Publication, 2001.

Moldwin, M.: An introduction to Space Weather, New York, Cambridge University Press, 2008.

Ondoh, T. and Marubashi, K.: Science of Space Environment, Ohmsha, Ltd., 2001.

Opperman, B.: Reconstructing ionospheric TEC over South Africa using signals from a Regional GPS network, Ph.D. thesis, Rhodes University, 2007.

Prikryl, P., Ghoddousi-Fard, R., Kunduri, B., Thomas, E., Coster, A., Jayachandran, P., Spanswick, E., and Danskin, D.: GPS phase scintillation and proxy index at high latitudes during a moderate geomagnetic storm, Annales Geophysicae, 31, 805 – 816, doi::10.5194/angeo-31-805-2013, 2013.

Rawer, K.: Wave Propagation in the Ionosphere, vol. 5 of *Developments in Electromagnetic Theory and Applications*, Kluwer Academic Publishers, Dordrecht, Boston, London, URL http://cds.cern.ch/record/1629258, 1993.

Rife, J., Khanafseh, S., Pullen, S., De Lorenzo, D., Kim, U.-S., Koenig, M., Chiou, T.-Y., Kempny, B., and Pervan, B.: Navigation, interference suppression, and fault monitoring in the sea-based joint precision approach and landing system, Proceedings of the IEEE, 96, 1958–1975, doi:10.1109/JPROC.2008.2006107, 2008.

Romano, V., Spogli, L., Aquino, M., Dodson, A., Hancock, C., and Forte, B.: GNSS station characterisation for ionospheric scintillation applications, Advances in Space Research, 52, 1237–1246, 2013.

Shanmugam, S., Jones, J., MacAulay, A., and Van Dierendonck, A.: Evolution to modernized GNSS ionoshperic scintillation and TEC monitoring, in: Position Location and Navigation Symposium (PLANS), 2012 IEEE/ION, pp. 265–273, IEEE, 2012.

SpaceWeatherlive.com: SpaceWeatherLive.com: Real-time auroral activity and solar activity, http://www.spaceweatherlive.com/en, [Online; accessed 2015-06-07], 2015.

Spogli, L., Alfonsi, L., De Franceschi, G., Romano, V., Aquino, M. H. O., and Dodson, A.: Climatology of GPS ionospheric scintillations over high and mid-latitude European regions, Annales Geophysicae, 27, 3429–3437, doi:10.5194/angeo-27-3429-2009, URL http://www.ann-geophys.net/27/3429/2009/, 2009.

Spogli, L., Alfonsi, L., De Franceschi, G., Romano, V., Aquino, M., and Dodson, A.: Climatology of GNPs ionospheric scintillation at high and mid latitudes under different solar activity conditions, IL NUOVO CIMENTO, doi:10.1393/ncb/i2010-10857-7, 2010.

Spogli, L., Romano, V., De Franceschi, G., Alfonsi, L., Plakidis, E., Cesaroni, C., Aquino, M., Dodson, A., Monico, J. F. G., and Vani, B.: A Filtering Method Developed to Improve GNSS Receiver Data Quality in the CALIBRA Project, INTECH open science open mind, 2014.

Valley, G. G. S.: GSV4004B GPS Ionospheric Scintillation & TEC Monitor (GISTM) User's Manual, 1131 Seena Avenue, Los Altos, CA 94024, USA, 2005.

Van Dierendonck, A., Klobuchar, J., and Hua, Q.: Ionospheric scintillation monitoring using commercial single frequency C/A code receivers, in: proceedings of ION GPS, vol. 93, pp. 1333–1342, 1993.

Wanninger, L.: Ionospheric monitoring using IGS data, in: Proceedings of the 1993 IGS Workshop, pp. 25–26, 1993.

Wernik, A., Secan, J., and Fremouw, E.: Ionospheric irregularities and scintillation, Advances in Space Research, 31, 971 – 981, doi:http://dx.doi.org/10.1016/S0273-1177(02)00795-0, URL http://www.sciencedirect.com/science/article/pii/S0273117702007950, 2003.

Zell, H.: Earth's Atmospheric Layers, http://www.nasa.gov/mission_pages/sunearth/science/atmosphere-layers2.html, [Online; accessed 2015-05-30], 2013.